High-Speed Photodiodes for Applications in Photonic-Based Millimeter Wave Systems

---

A

Dissertation

Presented to
the faculty of the School of Engineering and Applied Science
University of Virginia

---

in partial fulfillment
of the requirements for the degree

Doctor of Philosophy

by

Jesse S. Morgan

August 2022

APPROVAL SHEET

This
Dissertation
is submitted in partial fulfillment of the requirements
for the degree of
Doctor of Philosophy

Author: Jesse S. Morgan

This Dissertation has been read and approved by the examining committee:

Advisor: Andreas Beling

Committee Chair: Joe C. Campbell

Committee Member: Olivier Pfister

Committee Member: Steven M. Bowers

Committee Member: Robert Weikle

Accepted for the School of Engineering and Applied Science:

Jennifer L. West, School of Engineering and Applied Science

August 2022

To my family, my supportive and loving wife Rachel, and our lil' boy Jake.

Contents

List of Figures

List of Tables

Acknowledgments

Thanks to my advisor, Dr. Andreas Beling. At the writing of this thesis, I have known Andreas now for almost 7 years, since first taking an undergraduate course with him in 2015. Since that time, he has been unwavering in his professionalism and dedication to promoting knowledge and learning in his students. His door has always been open, even his Zoom virtual door since the pandemic, and he has always made me feel like there are no dumb questions. He goes above and beyond in his duties as a mentor, professor, and a leader, and has supported every goal I have set out to accomplish. He is truly an expert in what he does and I will be forever grateful for the growth he helped me achieve during my time under his advisement. If I am fortunate enough to continue to work with people of Andreas's caliber, my life after PhD will be very fulfilling.

I would also like to thank Professor Joe C. Campbell, both for chairing my advisory committee and for his helpful discussions throughout the last six years. He understands and values hard work, leads by example, and always has his door open for the students. In addition to how much he has accomplished in the field, his humble nature and friendly manner has made his example that much more to live up to. I also want to thank Professor Harry Powell, who helped me hone my engineering skills during my undergrad, giving me many opportunities to be involved in the department and always being supportive and ready to help me grasp the finer points of "cooking with gas." I also want to thank Dr. Meredith Hutchinson, who I first met through my first two research projects, and whose mentorship and friendship as I move into the professional world has helped keep me grounded and set me up for success. I also want to thank Professor Patricia Weisbrod, who encouraged me at the community college in 2012 to try out calculus, which opened my eyes to the world of engineering and quantifying the world through mathematics, and set me on the path to becoming an engineer.

A big thanks goes out to my advisory committee. I have had the privilege to work closely with Professor Steve Bowers on projects, and learned a lot through our discussions and his critical thinking and knowledge. A big thanks to Professor Olivier Pfister, who continues to put up with us engineers and ask us the hard physics questions to get the wheels turning. I have also had the privilege to work with and get classroom instruction from Professor Robert Weikle, whose mastery of teaching I can only equate to watching art in action.

My research group has also been a big part of this journey, from which I've made many colleagues and friends. In particular Bassem Tossoun and Jizhao Zang, not only became lifelong colleagues, but became foundational supports on my journey and lifelong friends. I can't give a big enough thank you to Keye Sun, who's quest to always learn more and willingness to always go to the math to help answer the difficult research questions continues to impact my approach to problem solving. Thanks to Junyi Gao, Ta-Ching Tzu, Xiangwen Guo, Qinglong Li, Fatemeh Tabatabaei, Tasneem Fatema, Xiaojun Xie, Min Ren, Maddy Woodson, Yang Shen, Ye Wang, Zhanyu Yang, Qianhuan Yu, Andrew Jones, Yuan Yuan, Jiyuan Zheng, Yiwei Peng, Fengxin Yu, and Dekang Chen for their helpful discussions and friendship during the stressful times that inevitably arise during long days and nights in the lab.

The front office in the ECE department has also been a huge help, not only administratively, but also as a place to go and talk about life and things outside of the daily engineering grind. Thanks to Beth Eastwood-Beatty, Crystal Aldridge, Susan Malone, Yadi Weaver, and Dan Fetko. You all do a huge job and I hope you realize how appreciative we are. Thank you.

Finally, my family has been everything I need to persevere and come out on the other side of this journey stronger, intellectually and morally. I was fortunate to meet my now wife in my first year of the journey and share in her PhD journey at the same time. Her empathy and support during the most rigorous times enabled me to be able to step back and enjoy the journey along the way, and our Lab Jake has been the greeting I needed many nights coming home late from the lab. Watching my siblings grow with their families and still make time for our family trips and meals and triathlons kept me excited for life after PhD. My parents' support has also been a rock on this journey, and the love and support of my in-laws has given me the strength of two sets of parents. I can't thank you all enough for your support and love and for sharing this journey with me. I love you all so much.

Abstract of the Dissertation

High-Speed Photodiodes for Applications in Photonic-Based Millimeter Wave Systems

by

Jesse S. Morgan

Doctor of Philosophy in Electrical and Computer Engineering

University of Virginia, June 2022

Andreas Beling, Advisor

Technologies based on millimeter wave (mmWave) (30-300 GHz) systems continue to emerge in the areas of wireless communications, radar, imaging, and spectroscopy. While exact requirements vary between applications, a fundamental requirement exists for all photonic-based platforms: mmWave sources capable of high-frequency, high-power operation and, ideally, wide tunability. To achieve mmWave operation in photonic-based approaches, photodiodes (PDs) with broad bandwidth (DC to 100's of GHz) and high-power capability play a critical role in converting optical signals into electrical signals.

This thesis demonstrates a push forward of the state-of-the-art in high-speed and high-power III-V based photodiodes for application in photonic-based mmWave systems. To this end, novel approaches to the epitaxial (semiconductor) design, microwave circuit design and integration, and methods of device fabrication are shown. Through the mmWave frequency range, flat roll-off at low -1 V bias, and high power for single device photodiodes is demonstrated. 3-dB bandwidths above 110 GHz under bias, and 92 GHz at zero bias are also achieved. Better than 70% yield of a photodiode array fabricated with a new surface normal PD fabrication procedure is also shown.

Chapter 1

Introduction

This thesis examines and pushes forward the state-of-the-art in high-speed and high-power III-V based photodiodes for application in photonic-based millimeter-wave (mmWave) systems. To this end, novel approaches to the epitaxial (semiconductor) design, microwave circuit design and integration, and methods of device fabrication are presented, theoretically and experimentally. Research conducted building on the work of my predecessors is also presented as a means of describing the current state-of-the-art and motivation for the approaches taken.

1.1 Photodiodes and Photonic-Based mmWave Systems

As applications using photonic generation of radio frequency (RF) signals move to higher speeds, high-speed photodiodes continue to be critical components in a wide range of these systems [1]. Analog photonics applications including radio-over-fiber and antenna remoting, require that photodiodes (PDs) have high power handling capability and high linearity in order to maintain high RF gain and large spurious-free dynamic range [2]. Our research group at the University of Virginia has worked toward that end in the development of PD technology.

Within this push toward higher speed applications, technologies based on millimeter wave (mmWave) (30-300 GHz) systems continue to emerge in the areas of wireless communications, radar, imaging and spectroscopy [3][4][5]. While exact requirements vary between applications, a fundamental requirement exists for all photonic-based applications: mmWave sources capable of high-frequency, high-power operation and, ideally, wide tunability. A number of methods to produce these frequencies through optical means exist, such as optical heterodyning, electro-optic (EO) modulation, and as shown in Figure 1.1, photodetection of microresonator soliton frequency

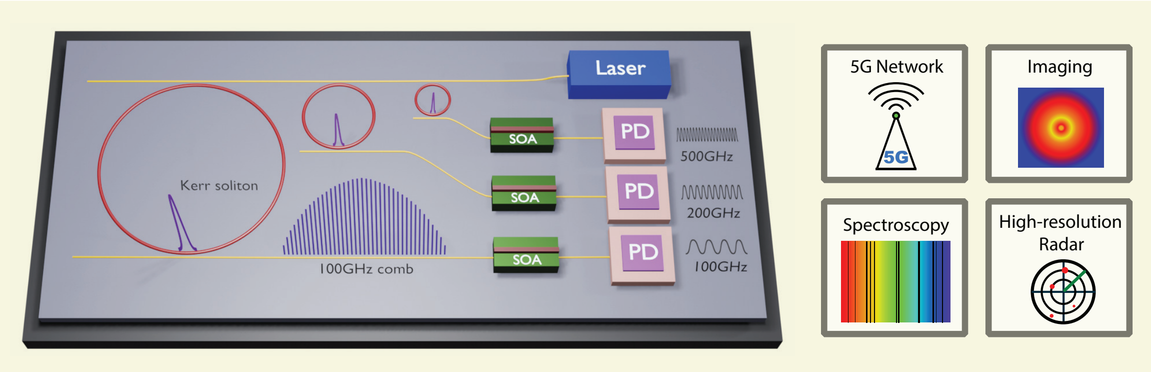

Figure 1.1: Conceptual view of fully integrated mmWave platform using high-speed high-power photodiodes (PD) with microresonator soliton excitation.[6]

combs [6]. Furthermore, with the help of optical amplifiers such as the semi-conductor optical amplifier (SOA) illustrated in Figure 1.1, these signals can easily reach powers in the hundreds of milliwatts. To achieve mmWave operation in photonic-based approaches, as mentioned previously, PDs with broad bandwidth (DC to hundred's of GHz) and high-power capability play a critical role in converting these optical signals into electrical signals. However, as the frequency response roll-off with photodiodes goes, the ability to efficiently convert the high-power optical signals to high power electrical signals degrades. Thus, the faster the speed (higher the bandwidth) of a photodetector and lesser the roll-off, the higher the power output at mmWave frequencies. This proves beneficial as high-power operating levels can provide high RF gain, low noise figure, and high spur-free dynamic range performance [7]. While a number of different material platforms for photodiodes exist, this thesis primarily examines photodiodes based on the group III-V modified uni-traveling carrier (MUTC) design with a brief review of Germanium based PDs.

1.2 Photodiode Fundamentals

Figure 1.2a shows a high-level diagram of the function of a photodiode (PD). At its most fundamental level, the PD receives an optical signal carrying an RF signal, the PD absorbs the photons with energy $(h\nu)$ generating electron-hole pairs which are accelerated through the PD depletion region by an electric field that is enhanced by the applied bias voltage, V_{bias}, whereby generating a RF modulated photocurrent I_{PD} and delivering the power in the converted signal to a load, R_{load}. There are many methods for generating the optical signal that is delivered to the PD. One such method of generation, optical heterodyning, is demonstrated in Figure 1.2b, where two

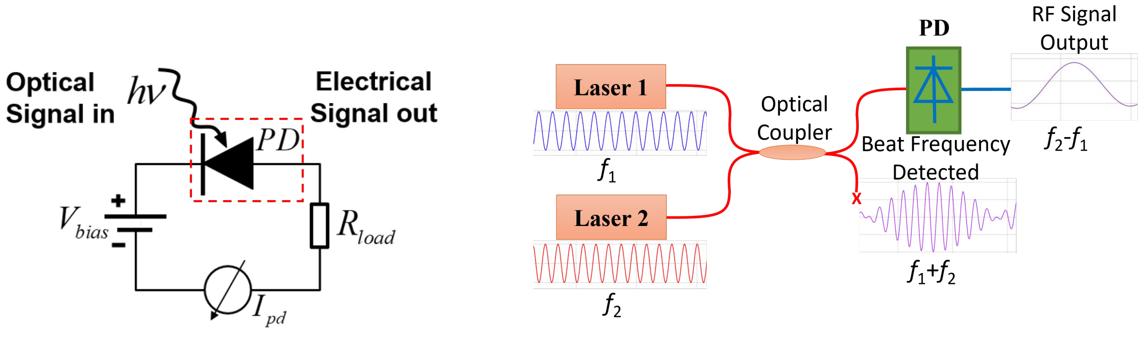

(a) (b)

Figure 1.2: High level concept of a photodiode (a) and photodiode signal extraction under optical heterodyne signal generation (b).

operationally equal lasers are coupled together and then offset to generate a difference frequency (beat note), RF envelope on optical carrier. Other methods of signal generation include electro-optic (EO) modulation, in which the RF signal is directly modulated onto one optical carrier through a modulator, and optical frequency comb generation in which equally spaced lines in a frequency comb beat with each other to generate a pulse train which is delivered to the PD at the repetition rate of the lines. Waveguide, or edge-coupled photodiodes, utilize an optical waveguide to couple the optical signal horizontally along the length of the absorbing region in the PD, and surface normal photodiodes couple the light vertically through the PD absorbing region. The RF signal output from the PD can be transmitted via free-space such as in an antenna application, or directly through electrical transmission lines such as in an analog photonic link application. Thus, by linking the optical domain to the electrical domain in order to harness the inherent benefits of optical generation and transmission, photodiodes play a crucial role.

1.2.1 PD Bandwidth (Speed)

When assessing the “high-speed” performance in photodiodes, the primary figure of merit is the 3-dB bandwidth of the PD. Under reverse bias, the PD acts as a low pass filter, and so the bandwidth of the device is considered as the point where the RF output power decreases by 3-dB from the low frequency (“DC”) value. The resistor-capacitor (RC) response time and carrier transit times are the primary factors that determine the 3-dB roll-off point in photodiodes.

To analyze the RC limited bandwidth, it makes sense to start by looking at the circuit

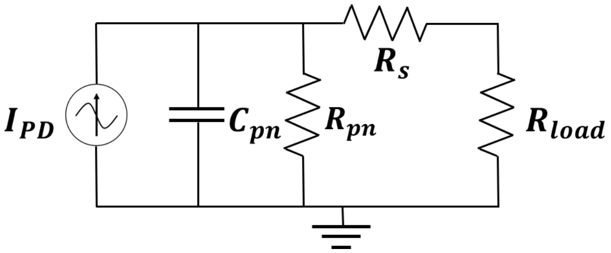

Figure 1.3: Typical equivalent circuit model for a photodiode.

model for a photodiode. As shown in the model in Figure 1.3, we typically represent the PD as a current source with an internal series resistance, R_s, p-n junction capacitance, C_{pn}, in parallel with the p-n junction resistance, R_{pn}, with the external load that the PD sees in series as a resistance, R_{load}. Because R_{pn} is generally found to be on the order of M-Ω's, we treat it as an open circuit and the current delivered to the load becomes:

$$I(\omega) = I(0)\left[\frac{\frac{1}{j\omega C_{pn}}}{\frac{1}{j\omega C_{pn}} + (R_s + R_{load})}\right] = \frac{I(0)}{1 + j\omega C_{pn}\left(R_s + R_{load}\right)}, \tag{1.1}$$

where $I(\omega)$ is the photocurrent at angular frequency ω, and $I(0)$ is the DC photocurrent. We then use a simple parallel plate representation for C_{pn}:

$$C_{pn} = \frac{\varepsilon_0 \varepsilon_r A}{d}, \tag{1.2}$$

where ε_r is the relative permittivity of the depletion region material, ε_0 is the vacuum permittivity, A is the active area in the photodiode, and d is the thickness of the depletion region. We can express the RC response time limited 3 dB-bandwidth as:

$$f_{RC} = \frac{1}{2\pi C_{pn}\left(R_s + R_{load}\right)}. \tag{1.3}$$

Thus, if the series resistance is small relative to the load resistor, then the primary knob to turn in the design of the PD to improve RC limited bandwidth, is the junction capacitance. However, reducing C_{pn} by reducing A means reducing the physical size of the PD, leading to larger contact resistance. Thus, device design must also consider the trade-off in small capacitance and larger contact resistance. I show in Section 6.2 my approach to reducing the total junction capacitance by reducing parasitic capacitance in hopes to somewhat offset this trade-off.

After photon absorption, electron-hole pairs are generated and then must travel through the depletion layer to the p- and n-type contact layers. The time for this travel is the carrier transit time. For the case of a p-i-n photodiode, if we assume uniform illumination of the PD, and that the electrons and holes travel through the thickness of the absorber/depletion layer d at a constant saturation velocity V_e and V_h, then we can express the normalized current as [8]:

$$\frac{I(\omega)}{I(0)} = \left[\frac{1}{\omega^2\tau_e^2}\{1 - exp(j\omega\tau_e)\} - \frac{1}{j\omega\tau_e}\right]\left[\frac{1}{\omega^2\tau_h^2}\{1 - exp(j\omega\tau_h)\} - \frac{1}{j\omega\tau_h}\right], \tag{1.4}$$

where τ_e and τ_h are the transit times of the electrons and holes, respectively. If we consider then that the transit time limited bandwidth is achieved when $\left|\frac{I(\omega)}{I(0)}\right| = \frac{1}{\sqrt{2}}$, then we can approximate the transit time limited bandwidth to be [8]:

$$f_t \approx \frac{3.5\bar{V}}{2\pi d}, \tag{1.5}$$

where:

$$\bar{V} = \left(\sqrt[4]{\frac{1}{2}\left(\frac{1}{V_e^4} + \frac{1}{V_h^4}\right)}\right)^{-1} \tag{1.6}$$

is the average of the electron and hole drift velocity in the depletion region. In Equation 1.5, it can be seen that by reducing d in the photodiode epitaxial stack, we can improve the transit time limited bandwidth, though as will be shown in Equation 6.3, at a trade-off in efficiency for surface normal PDs. Finally, if we consider that f_{RC} and f_t have a Gaussian response, then we can approximate the total speed response in the photodiode as [8]:

$$f_{3dB} = \left(\sqrt{\frac{1}{f_t^2} + \frac{1}{f_{RC}^2}}\right)^{-1}. \tag{1.7}$$

1.2.2 PD Power

The next figure of merit associated with photodiodes in RF applications, is the maximum power they can deliver at a given RF modulation frequency. To quantify this power, we consider the amount of AC power delivered to R_{load}. For a continuous wave signal frequency, f, we express the RF power with:

$$P_{RF} = \left|I_{(t,f)}\right|^2 Z, \tag{1.8}$$

with Z as the impedance of R_{load}, $\left|I_{(t,f)}\right|$ as the root mean square (RMS) value of the AC current $\frac{I_p}{\sqrt{2}}$ where I_p is the peak value of the current. From Equation 1.8, assuming 100% modulation depth and using $Z = R_{load}$, the DC photocurrent equates to I_p, and we can re-write the ideal power delivered to the load (ignoring bandwidth limiting effects) as:

$$P_{RF} = \frac{1}{2}I_{DC}^2 R_{load}. \tag{1.9}$$

Formal treatment of power output capability is assessed as the point where the RF output power from the PD saturates, as the input optical power level continues to increase. When measuring the RF power output, as will be shown in multiple chapters to come, the power increases quadratically (or linear with slope of 2 on a log-log scale) with optical input power increase, until at a certain point, the magnitude of the photocurrent causes the PD to suffer saturation, preventing strict quadratic growth. To quantify the point where this saturation happens, we consider the ideal Equation 1.9. Then, comparing the measured power to the calculated power, the 1 dB compression point denotes the average photocurrent, at which the RF output power deviates 1 dB from the quadratic current-power relation. The photocurrent at this 1 dB compression we define as the saturation current.

When we consider the knobs to turn for improvement in power performance, one consideration is the thermal handling capabilities of the devices. To mitigate thermal effects, one approach we have successfully applied is flip-chip bonding photodiodes to thermally conductive substrates, to facilitate heat transfer out of the PD junction [9]. We have also looked into the device design itself. For a typical p-i-n photodiode operating at 1550-nm wavelength, using a narrow bandgap InGaAs as the absorber and depletion region, as optical input increases high electric field and high current leading to Joule heating in the device, generates a higher dark current in the junction, and ultimately adds to more total current, which leads to heating in the device. This heating process can activate defect states in the PD, and ultimately can lead to thermal breakdown, killing the device. It will be shown in Section 1.3 how we separate the absorption and depletion region to reduce this thermal runaway process.

Another factor we consider in improving power performance is mitigation of the space-charge screening effect. This occurs in the depletion region when the charge from carriers generated from photon absorption off-set the space charge and thus reduce the electric field that is meant to accelerate the carriers through the device and to the electrical contacts. With higher input optical power comes higher density of generated carriers, which leads to carrier accumulation at the edges of the depletion region, whereby generating an internal field opposing the field from the bias voltage. We therefore need to pay attention to the carrier concentrations in the PD's materials and the bias voltage needed to control these carriers under operation. The effects of space-charge screening can be found in the solutions to the carrier continuity equations and Poisson's equation [10]:

$$\frac{dE}{dx} = \frac{\rho_{(x)}}{\varepsilon_0 \varepsilon_r}, \tag{1.10}$$

which can be re-written as:

$$\frac{dE}{dx} = \frac{q}{\varepsilon_0 \varepsilon_r} \left(p - n + N_D - N_A\right), \tag{1.11}$$

$$E = \frac{q}{\varepsilon_0 \varepsilon_r} \int_x^{x+\Delta x} \left(p(x) - n(x) + N_D(x) - N_A(x)\right) dx, \tag{1.12}$$

where E is the electric field over the length of the depletion region x, $\rho_{(x)}$ is the charge density in the depletion region, N_A and N_D are the static acceptor and donor concentrations, respectively, and n and p are the electron and hole concentrations, respectively. If the intrinsic region is truly undoped, the slope of the electric field is zero meaning a constant electric field across the region. The field strength then, across the intrinsic region is highly dependent on the photogenerated carriers. So as the free carrier concentrations increase with higher optical power, the field from the charge of these carriers becomes stronger, which can oppose the electric field from the fixed charges that is responsible for accelerating the carriers to the electrical contacts, whereby leading to an accumulation of charge, ultimately leading to the space-charge screening effect. The PDs we design attempt to pre-distort the electric field through charge-compensation, i.e. counteract the charge of photogenerated carriers, as will be highlighted in Section 1.3.

1.3 Charge Compensated Modified Uni-Traveling Carrier Photodiodes

Among the reported high-speed photodiode structures [12][13] and illustrated in Figure 1.4, the charge-compensated modified uni-traveling carrier photodiode (CC-MUTC PD) operates under the principle of mostly single carrier transit, and compared to traditional p-i-n photodiodes, isolating electrons for this transit process eliminates the dependency on the slower traveling holes leading to higher-speed operation. Over the past years, our group has developed InGaAs/InGaAsP/InP MUTC PDs that achieved high bandwidth above 100 GHz, high responsivity, and low dark current [11]. Similar to uni-traveling carrier (UTC) photodiodes [14], MUTC photodiodes include a narrow-bandgap un-depleted absorber and a depleted wide-bandgap drift layer, and by using a graded doping in the undepleted absorber, an electric field is generated which accelerates electrons through. To increase responsivity, however, MUTC also uses a lightly n-type doped absorber between the undepleted absorber and the drift layer. This depleted absorber maintains a high electric field at the heterojunction interface to improve electron transport. In the p-type absorber, to accomplish the mostly single carrier transit, photogenerated excess holes decay within their short

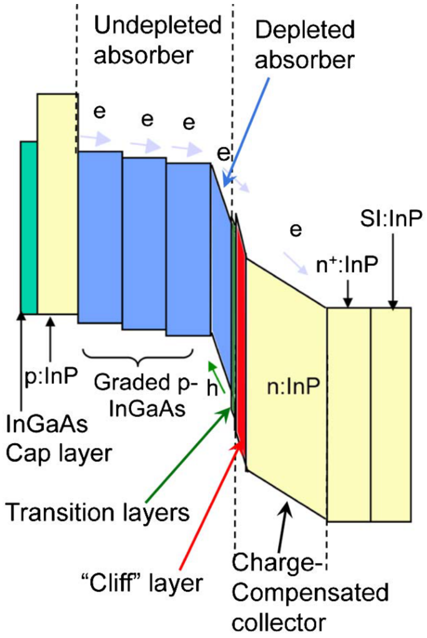

Figure 1.4: Band diagram and operating principle behind CC-MUTC PDs.[11]

dielectric relaxation time, and electrons move via both diffusion and drift before being injected into the depletion region. To further prevent electric field collapse at the heterointerface of the absorber and drift layer, a moderately doped cliff layer is inserted [15][16]. Once in the drift layer, electron space-charge effects are pre-distorted or charge compensated by light n-type doping in the drift layer, which helps to avoid saturation and increase RF output power under high photocurrent [9]. When designed for high bandwidth, these photodiodes, known colloquially in the Optoelectronic Device Group at UVA as FUTC (fast uni-travelling-carrier), will be referred to as such moving forward.

Chapter 2

High-Power Flip-Chip Bonded FUTC Photodiodes


FREEDOM PHOTONICS

Figure 2.1: Fully packaged FUTC PD with pigtail fiber and coaxial connector.[17]

A target application of the charge-compensated MUTC photodiodes (FUTC PDs) designed and fabricated at UVA was eventual implementation as fully packaged devices for use in high-power, wide-bandwidth applications such as RF photonic links, sensing, and photonic generation of RF signals. Building on the epitaxial design of the FUTC PDs, this goal was achieved through the microwave design and modeling of both a new transmission line and the chassis, housing the PD and submount. After technology transfer of the epitaxial structure and fabrication procedure, the final product, produced and manufactured by our collaborator, Freedom Photonics, LLC, is shown in Figure 2.1, with a pigtail fiber optical input to the PD and coaxial connector for RF output from the PD. The following sections will describe the PD design behind both this packaged device application of the FUTC PD, as well as an emitter application integrating the PDs with wide-band antennas through flip-chip bonding.

2.1 Device Design and Application

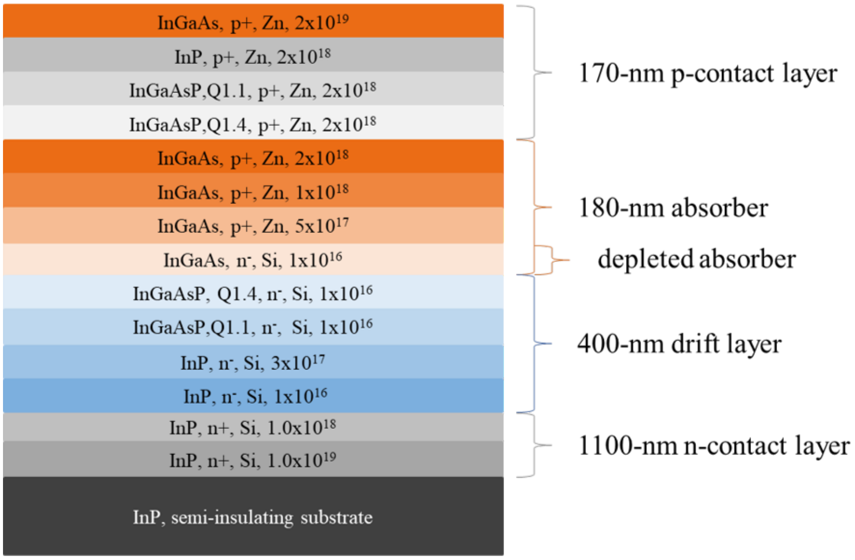

Figure 2.2: FUTC PD epitaxial-layer design.[18]

Backside illuminated FUTC PDs with diameters from 4 to 11-µm were fabricated from a 2-inch InGaAsP/InP wafer. The epitaxial structure for the PDs grown on native InP substrate is shown Figure 2.2 and the band diagram and operating principle is shown in Figure 1.4. Above the substrate, a heavily doped n-type InP acts as the n-contact layer followed by the charged-compensated InP drift layer and the InP cliff layer. Quaternary layers of InGaAsP are then grown to smooth conduction band discontinuity leading into the depleted and undepleted (with step-graded doping) InGaAs absorber layers. The quaternary layers above the absorber help to block electron transport into the anode, and the heavily p-doped InGaAs top layer acts as the p-contact layer. The PDs were fabricated using a double mesa process. The p-mesa was made by dry etching to the InP n-contact layer as illustrated in Step 3 of Figure 2.3. The large n-mesa was formed next by dry etching into the InP semi-insulating substrate (Step 5, Figure 2.3). Passivation of the PD surface was done via plasma-enhanced chemical vapor deposition (PECVD) of SiO_2. Ti/Pt/Au deposited on the p-contact layer acts as the p-metal stack, and AuGe/Ni/Au grown on the n-contact layer acts as the n-metal stack. An air-bridge, Figure 2.9b, was fabricated to connect the p-metal to flip-chip-bonding pads on the InP substrate. Both the metal layers and air-bridge were then plated to a Au

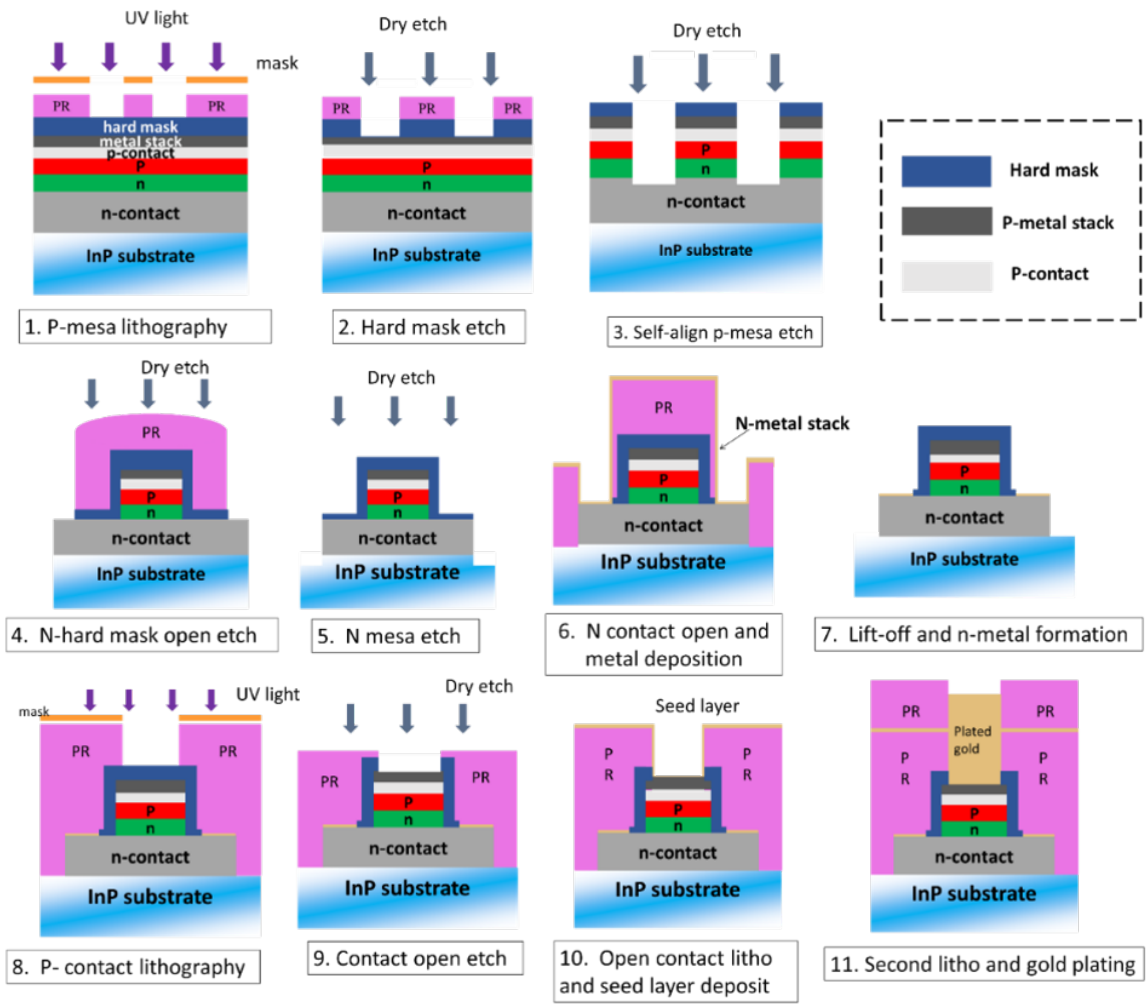

Figure 2.3: FUTC PD epitaxial-layer design.

thickness of 1.5-µm. The PDs were connected to gold-plated bonding pads via the air-bridge and to improve DC power dissipation were then flip-chip-bonded to a 380-µm thick AlN submount [9]. Figure 2.4 is a microscope image showing the front of a completed photodiode die with the bonding pads and air-bridge zoomed in on a single 07-µm device (left), and back of the photodiode die flip-chip bonded to the AlN submount (right).

The FUTC PDs examined in this thesis have demonstrated dark currents as low as 200 pA at -2 V, a 3-dB bandwidth of up to 145 GHz (4-µm diameter PD), a responsivity of 0.2 A/W at 1550 nm, and a -2.6 dBm maximum output power at 160 GHz at -3 V bias [19]. They have also been investigated as viable receivers for soliton applications ranging from 50 to 500 GHz [20][21].

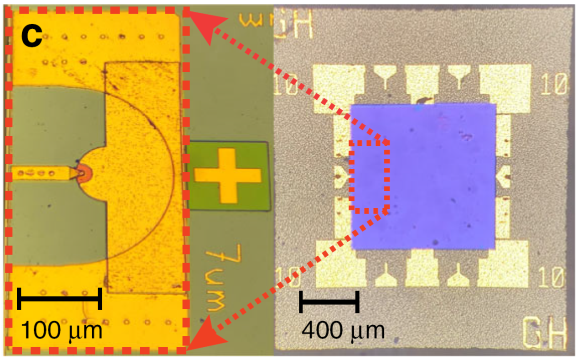

Figure 2.4: Microscope image of front of PD die zoomed on single 7-µm device (left), and back of PD die flip-chip bonded to AlN submount (right).[6]

2.2 Device Characterization

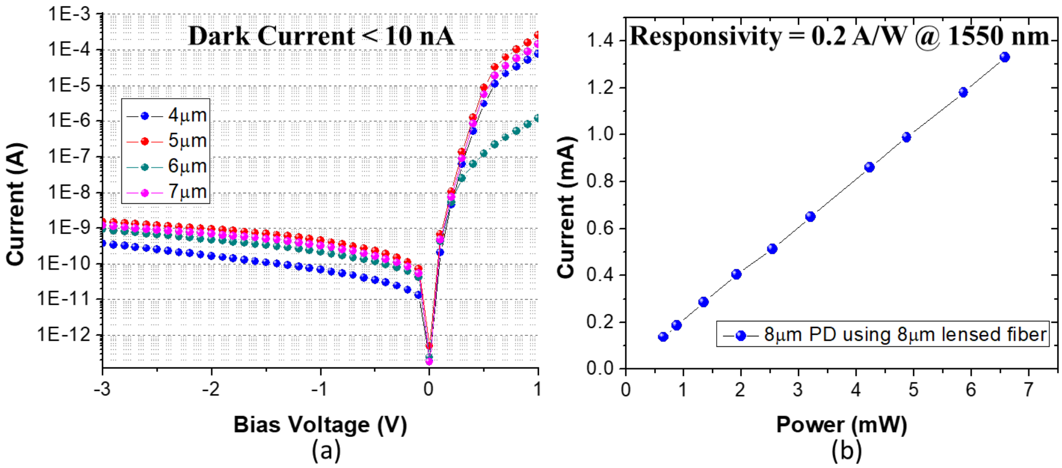

Figure 2.5: Dark current (a) and responsivity (b) measurements of FUTC.

Dark currents measured at -2 V bias ranged from 200 pA (4-µm) to 3 nA (10-µm) and responsivity of the devices was 0.2 A/W at 1550-nm shown in Figure 2.5 for various device sizes. Scattering parameter S11 for the devices was measured using a PNA Vector Network Analyzer up to 67 GHz at 3 V reverse bias. A model similar to that proposed in [22] was developed in Agilent's Advanced Design System (ADS) for parameter fitting, shown in the top of Figure 2.6a with the simplified model of the PD at high RF frequency in the bottom. The PD is modeled as an ideal

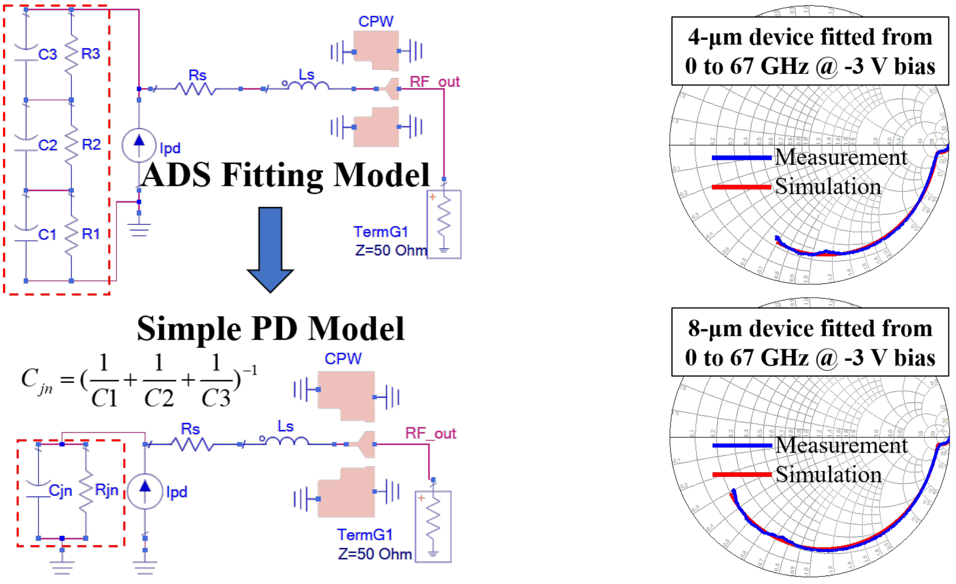

(a) (b)

Figure 2.6: ADS fitting circuit model based on [22] (top) and translation to simplified PD model (bottom) (a) and S11 fitting result of model (blue) compared to measurement result (red) (b).

current source with the transfer function:

$$I_{PD}(\omega) = I_0 \frac{1 - exp(j\omega t_r)}{j\omega t_r}, \tag{2.1}$$

where I_0 represents the average photocurrent value (mA), ω is the signal frequency and t_r is the transit time of electrons through the drift layer. This equation is of the form from Equation 1.4, but neglects the hole transit assuming only electron transit through the depletion region in UTC PDs. The current source is in parallel with a serial connection of three parallel RC circuits, C1 and R1, C2 and R2, and C3 and R3. The ideal current source then connects to the series resistance, R_s, and the series inductance, L_s, associated with the semiconductor resistance and the device's air-bridge structure. The S11 fitting results for 4-µm and 8-µm PDs are shown in Figure 2.6b. At high operating frequency, the signal sees the capacitors in series with R1 being the dominant (100's of kΩ's) junction resistance and we collapse the serial capacitance down to a single junction capacitance. Figure 2.7 compares the extracted and calculated capacitance of the devices using the parallel plate capacitance equation (Equation 1.2). Stray capacitance is extrapolated from the intercept of a linear fit of the S11 fitted values. The fitted and measured results show good agreement for all PD sizes. The measurement and fitting results are shown in Figure 2.8. The series resistance,

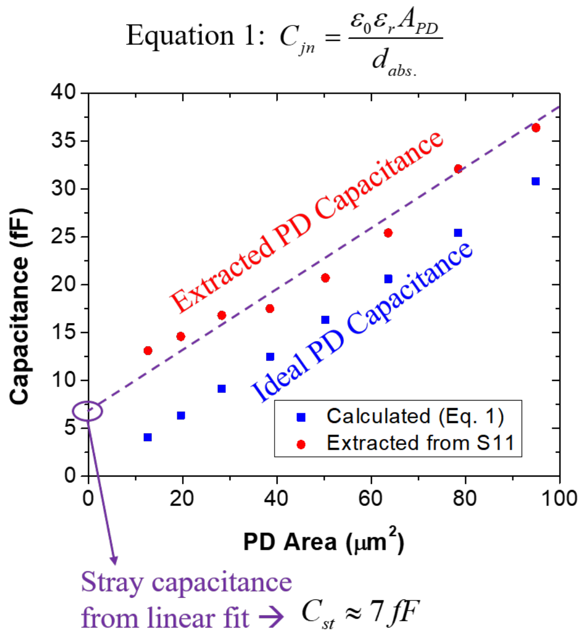

Figure 2.7: Chip-on-carrier ADS fitting results showing extracted and stray capacitance.

R_s, did not scale with device area meaning contact resistance is small, and series resistance is dominated by bulk resistance. For the extracted series inductance, L_s, the value scales inversely with device area, due to the width of the air-bridge structure, which is wider for larger diameter devices leading to a smaller inductance. To verify the extracted inductance values due to the air-bridge, I examined the design dimensions of the air bridge for various sized PDs as shown in Figure 2.9a for a 06-μm, 10-μm, and 14-μm diameter PD. To solve for the inductance in the air-bridge, we begin by looking at the skin depth at the operating frequency of interest, 110 GHz:

$$\delta = \left(\sqrt{\pi \mu \sigma f}\right)^{-1}, \tag{2.2}$$

$$\delta \approx 0.26nm$$

where, μ is the relative permeability of Au, σ is the resistivity of Au, and f is the operating frequency. Because the skin depth is much smaller than the thickness of the air-bridge (0.6-μm), we can neglect the frequency dependence and treat the inductance as Faraday (geometric) inductance, defined as:

$$L(nH) = 0.2l(mm)\left[ln\left(\frac{2l}{w+t}\right) + 0.5 + \frac{w+t}{3l}\right], \tag{2.3}$$

where, l is the length, w is the width, and t is the thickness of the geometric shape. If the thickness is much less than the width, the thickness can be neglected. Using the values from Figure 2.9a for

Size (µm)	C_1 (fF)	C_2 (fF)	C_3 (fF)	R_1 (Ω)	R_2 (Ω)	R_3 (Ω)	C_{pn} (fF)	R_s (Ω)	L_s (pH)	I_{dark} (nA)	Max Bandwidth (GHz)	Max RF Output Power @ 160 GHz (dBm)
4	350	30	25	300k	700	300	13.1	6	74	0.2	120	> -8.5*
5	385	33	32	300k	680	285	15.6	6	68	0.3	110	> -8.6*
6	420	40	32	300k	670	285	17	6	62	0.3	100	> -10*
7	450	37	36	300k	635	270	17.5	6	56	2	90	> -4.9*
8	510	45	43	300k	725	265	21	6	51	0.3	80	-3.5
9	540	56	51	300k	725	295	25.4	6	46	0.4	70	-2.6
10	660	68	66	300k	735	295	31.9	6	39	3	65	-3.5
11	770	77	75	300k	795	295	36.2	6	35	0.9	60	-3.5

Figure 2.8: Parameter extraction from S11 fitting and power performance of PDs. *PDs failed before reaching compression. [19]

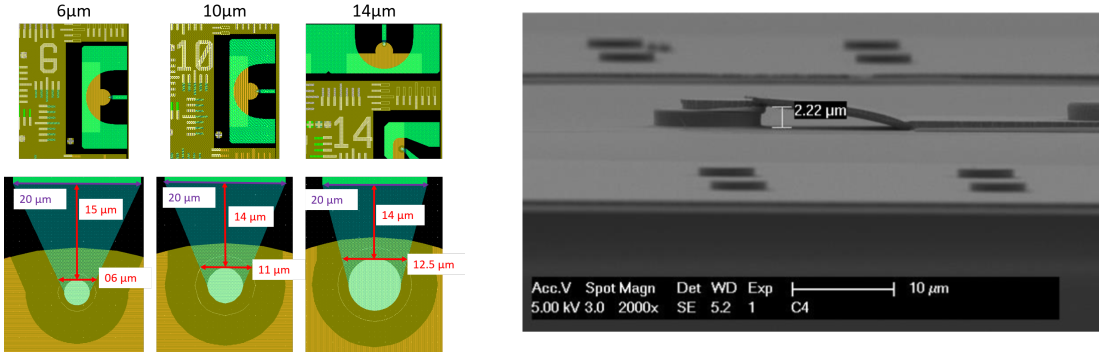

(a)

(b)

Figure 2.9: Mask layout and design dimensions of FUTC air-bridge structure for various sized PDs (a) and SEM of fabricated air-bridge structure (b).

the width and length of the air-bridge structures for different devices, it can be shown that the 6-µm PD should have an inductance ≈ 30% larger than the 10-µm PD, and ≈ 34% larger than the 14-µm PD. The 10-µm PD should have an inductance ≈ 6% larger than the 14-µm PD. If we use the fitting values from Figure 2.8 to compare the 6-µm PD to a 10-µm PD, we find that the 6-µm fitting is ≈ 37% larger than the 10-µm PD, which agrees well with the result of the equation considering fitting error and fabrication tolerance. The stray capacitance extracted from S11 fitting can be attributed to the overlap between the RF signal pads and air-bridge with the n-contact layer which can be seen for the air-bridge in the scanning electron microscope (SEM) image in Figure 2.9b.

The RF response was measured using an optical heterodyne setup illustrated in Fig-

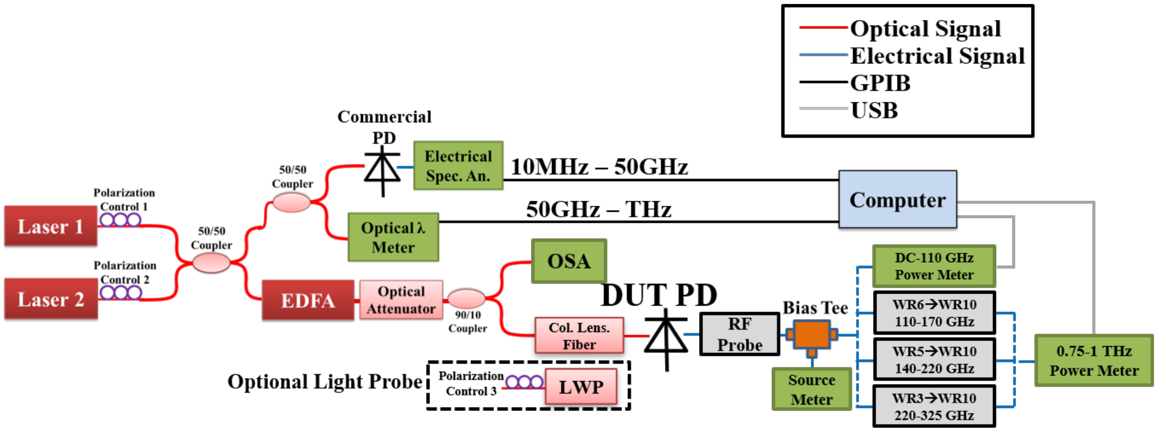

Figure 2.10: Optical heterodyne block diagram.

ure 2.10. Two 1550-nm lasers were set to the same power level, then their polarization was aligned through polarization controllers 1 and 2, and then their light was combined through a 3-dB optical coupler. The RF beat signal was then generated and controlled by tuning the lasing wavelength of one of the lasers. From the first 3-dB optical coupler, half of the RF beat note on optical carrier was sent towards the device under test (DUT), and the other half to another 3-dB coupler, where half of that signal traveled to an electrical spectrum analyzer and the other half to an optical wavelength meter for monitoring. A spectrum analyzer using a commercial photodiode, tracked the beat frequency up to 50 GHz and a multi-wavelength meter was used to track the beat note above 50 GHz. Measurements up to RF frequencies of 170 GHz were performed in two steps. From DC to 110 GHz, a GGB ground-signal-ground (GSG) high frequency probe (Model 110H) fed into an Anritsu high-frequency external bias-tee, and a Rohde-Schwarz power meter used for recording power levels. Probe loss from the vendor's data sheet was included in the measurements. A calibration file was generated for the external bias-tee and coaxial connections using a 7-step SOLT and offset shorts calibration kit (short (4), open, load, through) on a 110 GHz PNA. From 90 GHz to 170 GHz, a power meter working up to 1 THz from Virginia Diodes Incorporated (VDI) (PM5) was fed from a GGB GSG tapered WR-6 waveguide probe (Model 170) which had an integrated bias-tee and pitch size of 90-μm. Probe loss was again taken from the vendor data sheet and included in the measurement results. The RF saturation measurements used a similar setup. RF saturation was characterized by measuring the RF output power as a function of average photocurrent at a fixed RF frequency of 160 GHz. Shown in Figure 2.11, a 4-μm PD reaches a maximum 3-dB bandwidth of 145 GHz with an unsaturated RF output power of -7.5 dBm at 160 GHz. In Figure 2.12a a 7-μm

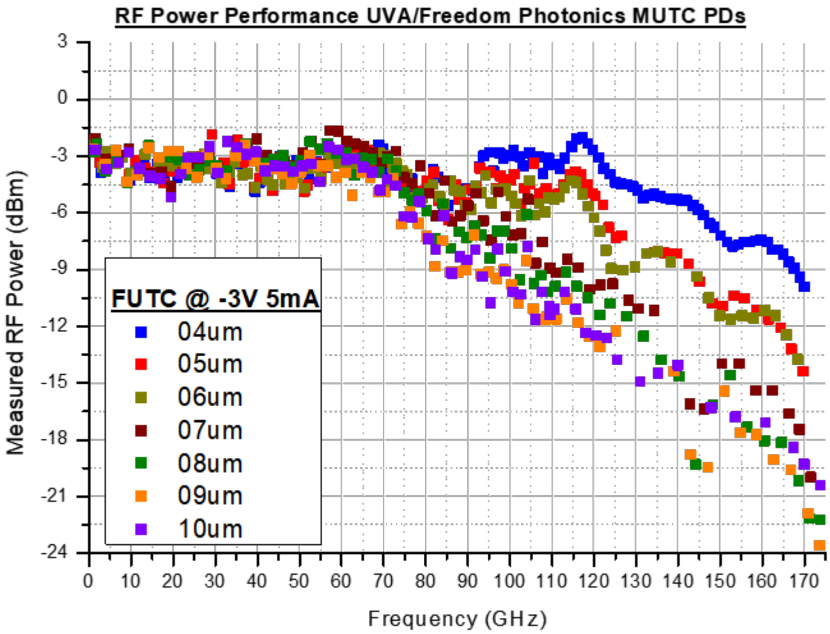

Figure 2.11: Bandwidth measurement of 4 to 10-µm PDs at 5-mA photocurrent and -3 V bias.

PD with 100 GHz bandwidth attains a maximum RF output power of -5 dBm at 160 GHz and -5 V, saturation current of 15 mA, and in Figure 2.12b a 9-µm PD with 70 GHz bandwidth attains a maximum RF output power of -2.6 dBm at 160 GHz and -5 V, and a saturation current of 40 mA.

2.3 FUTC PD Applications

2.3.1 Fully Packaged Devices

The goals of the fully-packaged PD project were to achieve full DC to V-band and DC to W-band coverage, in fully packaged receiver modules like that shown in Figure 2.1. The RF transmission line designed to accomplish this goal was done in two steps. Firstly, the coplanar waveguide (CPW), shown in Figure 2.13 (bottom right), was optimized to achieve an inductive peaking effect around 110 GHz, with the idea being to achieve coverage through the V-band (75 GHz) while maximizing the power output before roll-off in the upper end of the W-band (110 GHz). The bonding pads of the PD were flip-chip bonded to a Au ground-signal-ground (GSG) CPW transmission line, which achieved the inductive peaking effect using a 70 x 20-µm signal stub

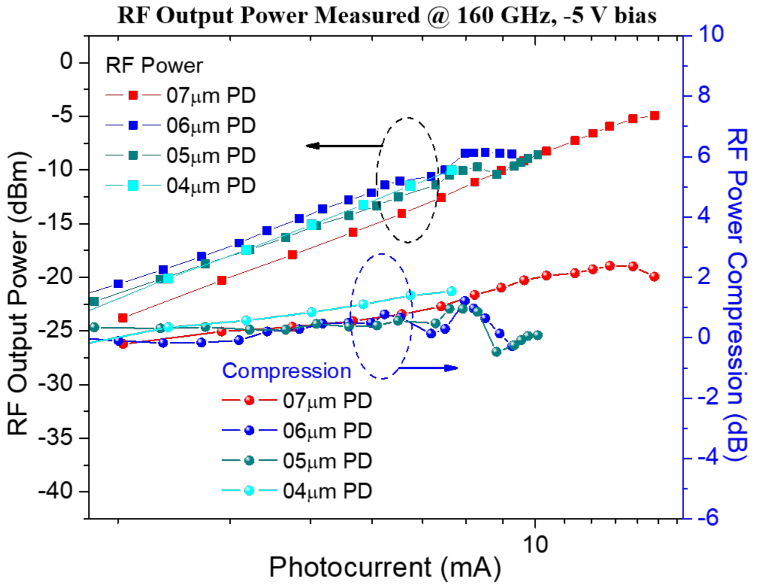

(a)

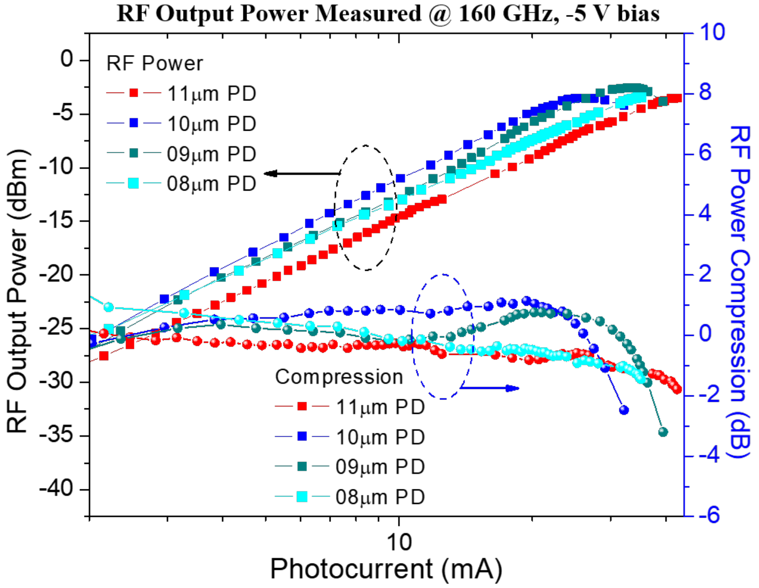

(b)

Figure 2.12: RF output power (left axis) and power compression (right axis) for 04-µm to 07-µm PDs (a) and 08-µm to 11-µm PDs (b).[19]

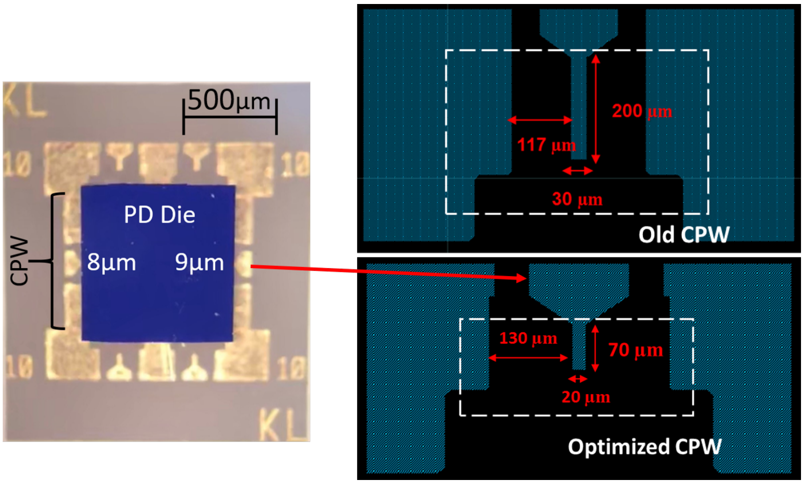

Figure 2.13: Microscope image of flip-chip bonded PD die on Au CPW on AlN submount (left) and initial optimization of 110 GHz peaking CPW.[19]

with a 130-µm signal-to-ground gap. A tapered section connected the stub to a 50 Ω, 50 x 154-µm pad with a 54-µm signal-to-ground gap and 250-µm pitch. The effect of the peaking can be well seen in the bandwidth measurements shown in Figure 2.11, particularly for the 04-µm, 05-µm, and 06-µm PDs. A microscope image of a fabricated PD die flip-chip bonded to the inductive peaking submount is shown in the left of Figure 2.13.

The second step in designing the CPW for the packaged application required that the CPW be compatible with connection to a coaxial connector. Therefore, I designed the CPW to maintain 50 Ω characteristic impedance at the output, while extending in length and width to accommodate the glass bead of a coaxial connector. To maintain the characteristic 50 Ω impedance on the output of the CPW, using the theory of small reflections, the CPW utilized a full-length taper in the signal and ground pads to accommodate a glass bead and maintain gap distance ratio with the ground planes. To achieve this the 50 Ω, 50 x154-µm pad with a 54-µm signal-to-ground gap shown in Figure 2.13 was extended to 1273-µm length with a 250-µm width and a 100-µm signal-to-ground gap. The pitch size of 250-µm was maintained for compatibility with the glass bead connection. This final design, drawn and simulated in ADS, is shown with the initial short CPW design and relative size to a PD die (purple) in Figure 2.14. Using a simple PD model in ADS as shown in Figure 2.15, I inserted the electromagnetic Method of Moments (MoM) simulation of the CPW and simulated the frequency response in order to validate the design and determine if the expected/required bandwidth could be achieved.

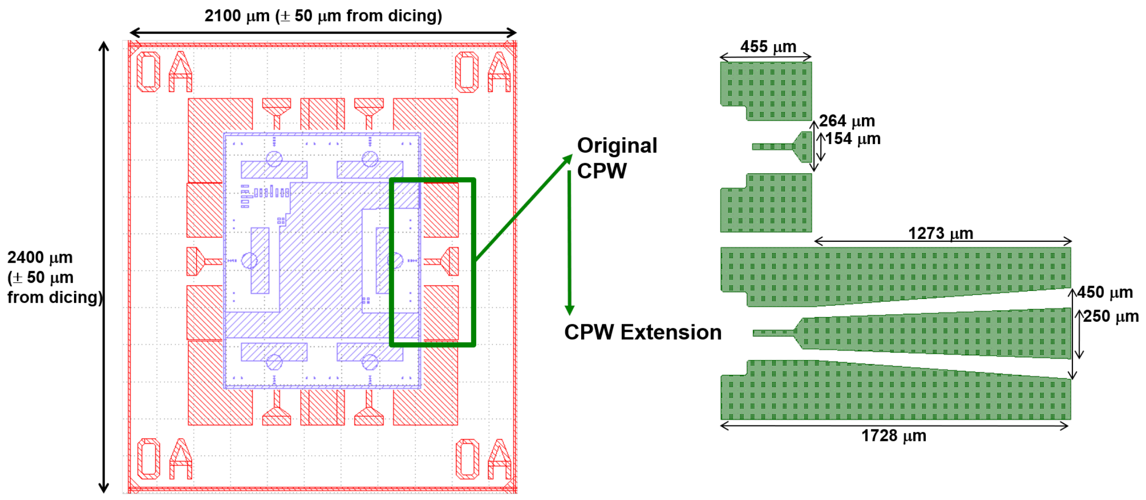

Figure 2.14: PD die layout (left) and final evolution (right) of FUTC CPW optimization for packaged application.

After fabrication of the submount, 2-port S-parameter measurements were done from DC-110 GHz using 110 GHz extenders with a Keysight PNA network analyzer. An on wafer probe-pad calibration standard was used to calibrate the two GGB Model-110 probes on port 1 and 2 of the extenders. The model of the PD using simulated CPW s2p data was then replicated and adapted by replacing the simulated s2p data with the measured s2p CPW data for comparison. Figure 2.15 shows the results of the simulated vs. measured s2p data for the optimized CPW. At a model photocurrent of 2-mA, good agreement can be seen with a 5-µm PD achieving 110 GHz 3-dB bandwidth. The CPW was next characterized by measuring the 2-port S-parameter response with the carrier mounted in the chassis, using an RF probe on the PD side, and coaxial connector on the output side. The top microscope image in Figure 2.16b shows a top view of the glass bead epoxied to the signal pad of the CPW. Once the CPW was fully characterized, the next step involved flip-chip bonding the PDs to the optimized submount, and characterizing their chip-on-carrier (CoC) performance. A fabricated CoC is shown in the middle microscope image in Figure 2.16b. Using optical heterodyning, the CoC was measured from DC-110 GHz over a range of photocurrents. The measured bandwidth is shown in Figure 2.16a for a 10-µm device measured at -3 V bias and 10 mA. The CoC model was updated to reflect that in Figure 2.6a and simulated from DC to 110 GHz, and is compared with the measurement result in Figure 2.16a. After measuring and characterizing all diameters of PDs in CoC form, the next step was to measure cut-package devices with the CoC mounted to the chassis and epoxied to the coaxial connector, as shown in the bottom image of Figure 2.16b. Again,

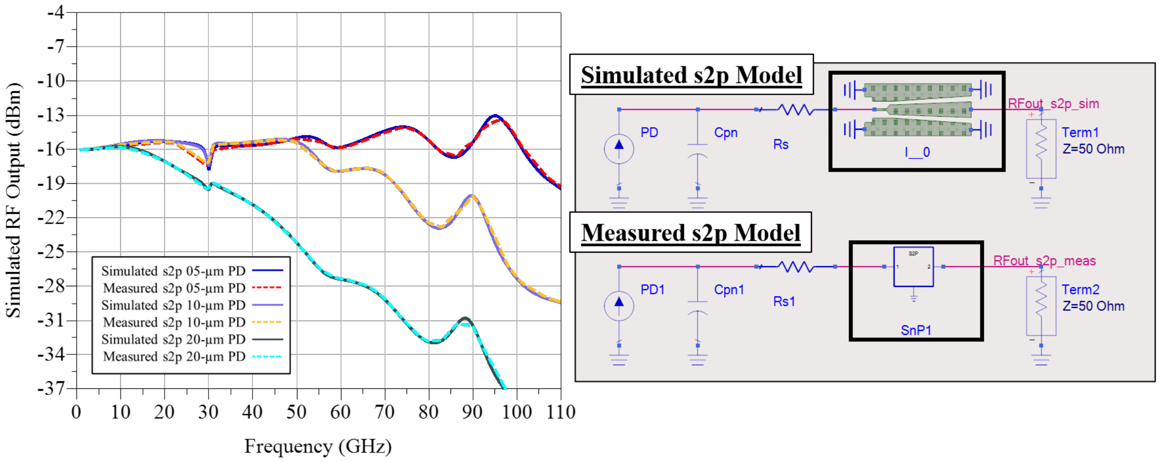

Figure 2.15: Simulated frequency response using simple PD model and comparing file-based CPW s2p data and simulated CPW s2p data.

DC-110 GHz measurements were performed in order to characterize performance.

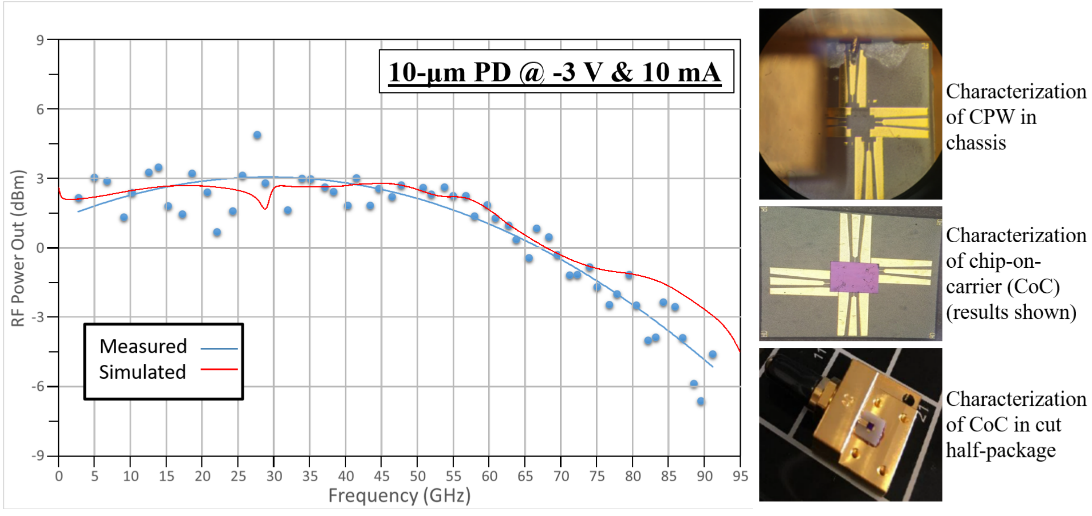

(a) (b)

Figure 2.16: Measured vs. simulated bandwidth for 10-µm PD on optimized CPW measured at -3 V and 10 mA (a) and evolution of CPW and device characterization (b).

The final step entailed fully-packaging the CoC in the chassis housing that had been designed by Freedom Photonics. After measuring the devices from DC-110 GHz fully-packaged, we saw performance degradation and bandwidth results as much as 50% less than expected. My thoughts as to why this degradation happened were the possibility of cavity resonances occurring between the Au transmission lines and the chassis housing, and potential issues with the epoxy used for the coaxial connection and thus the coax waveguide mode. In order to debug and fix the problem, the Method of Moments (MoM) simulation environment used by ADS, which uses an infinite reference plane, was no longer helpful. Therefore, I had to build and simulate the CoC in chassis using finite element modeling (FEM) in ANSYS High Frequency Simulation Software (HFSS). This approach to simulation and modeling allows not only the simulation of the CoC, but the interaction of the electric fields in the CPW mode with the surrounding environment, in this case, the chassis housing.

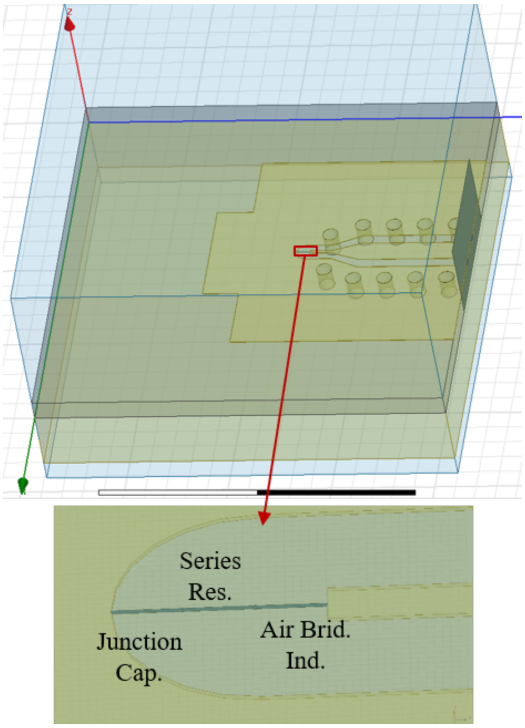

Figure 2.17: CoC on metal block model built in HFSS with incorporated PD model.

The first step of this process involved building and simulating the CoC in HFSS, with the goal of matching the overlap achieved between simulated ADS results and measured device results. After building the CPW on AlN submount, I used a lumped port excitation on the PD side and a waveport on the RF output side to measure S-parameters, and compared the results with the measured results and simulated ADS results. Next, I placed the submount on top of a Au plated block, and simulated S-parameters. The next step was to integrate the PD circuit model into the design. Shown in Figure 2.17, the CoC on Au plated block is pictured, with a zoomed in image showing the lumped port parameters, connected by perfect electrical conductors (PEC), representing the junction capacitance, C_{jn}, series resistance, R_s, and series inductance, L_s, of the PD model as shown in the simplified PD model in Figure 2.6a. It should be noted that a junction resistance, R_{jn}, was also included in parallel from the PEC connection of C_{jn}, and R_s to the ground plane, but showed negligible impact due to the magnitude of the junction resistance, and thus was neglected in the final model. After verifying the circuit model by comparing the bandwidth results to measurement and ADS simulation, I decided to next incorporate and investigate the chassis housing before looking at the glass bead and coax waveguide mode.

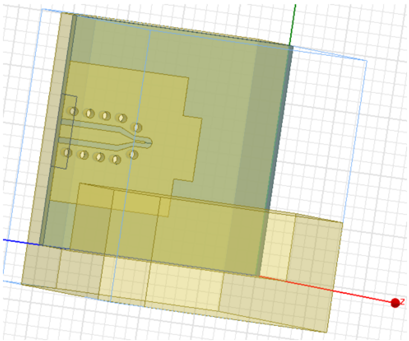

Figure 2.18: HFSS CoC model incorporated with more of mechanical chassis housing.

The HFSS model including more of the chassis housing is shown in Figure 2.18. It should be noted that my initial CPW design was altered in the initial packaged modules, which is why the discrepancy is evident in the picture of the CPW. Through analysis of the simulated model, the CPW utilizing vias and straight section of CPW to connect the PD to the output, when sitting in proximity to the Au plated overhanging block shown in Figure 2.18, interacts with the chassis to generate specific resonant frequencies that ultimately reduce the RF performance of the device. It was found that this performance limitation was due to a patch mode occurring in the large ground plane. This was verified by looking at S11 of the model and comparing resonances in the simulated model to the simple case of a rectangular patch resonance [23], defined as:

$$f_{mn} = \frac{c}{2\sqrt{\varepsilon_r}}\left[\left(\frac{m}{w_g}\right)^2 + \left(\frac{n}{l_g}\right)^2\right]^{0.5}, \tag{2.4}$$

where, c is the velocity of light, ε_r is the relative dielectric constant, w_g is the width and l_g is the length of the ground patch, and m and n are integers of the mode indexes. The resonances seen in S11 corresponding to the unanticipated frequency response roll-off in the bandwidth measurements, could be calculated from this equation. It was finally determined that my CPW design was optimal, and while proprietary biasing circuitry and some alterations to my design were done for the final proprietary product, the design and analysis I did paved the way to making a successful product and meeting the goals of the program.

2.3.2 Electromagnetic Emitters

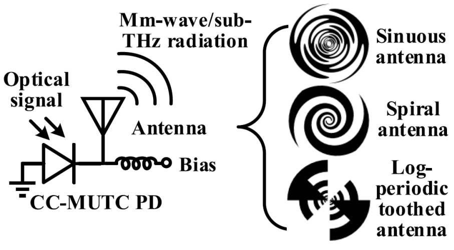

Figure 2.19: Photonically-driven emitter block diagram. [18]

In another target application, in collaboration with Professor Steve Bowers' group and Freedom Photonics, I worked closely with Xiaochuan Shen to characterize, through bandwidth and radiated power measurements and development of ADS circuit modeling, FUTC PDs flip-chip bonded by Freedom Photonics to frequency-independent (FI) antennas designed by Xiaochuan for use as high-power broadband integrated photonically driven emitters with high radiated powers operating from V-band to G-band (50–220 GHz). The benefit of the inherently wide bandwidth in this frequency range offers a promising solution to the ever-growing demand for high data rates required by the next-generation wireless communications [24, 25, 26] and wide bandwidth/frequency-tuning range is important for applications in spectroscopy [27], sub-THz imaging [28, 29], mm-wave radar [30, 31], and biology [32]. In biology, various biomolecules can be effectively recognized and characterized according to their distinctive spectral “fingerprints” lying between the microwave and infrared regions of the electromagnetic spectrum [32]. In mmWave imaging, single-frequency/narrowband imaging systems suffer from low imaging quality due to speckles created from complex interference from varying reflection points of the object under test. The speckles on the image can be largely eliminated by sweeping the operating frequency in a wide frequency range in order to achieve a 3-D holographic image with various depths, even for complex targets [29]. In another example application, frequency-modulated continuous-wave (FMCW) radars can distinguish closely spaced targets through high range resolution achieved with enormous absolute bandwidth [31]. MmWave and sub-THz wireless signals can be generated electronically [33, 34] or optoelectronically [35, 36]. Compared with integrated electronic systems, optoelectronic systems using photonically driven emitters may offer a promising and affordable approach to constructing high-power continuous-wave (CW) mmWave and sub-THz wireless links.

Figure 2.19 shows the general block diagram of the photonically driven emitter consisting of the photodiode (PD) and the antenna. The RF carrier (beat note) on the optical signal is generated by mixing two lasers (optical heterodyning) and is then illuminated on the PD. The PD extracts the beat note by absorbing and converting the input optical signal into photocurrents that drive the antenna to emit electromagnetic radiation at the beat frequency. The radiated power of the emitter is primarily determined by the available power of the PD, the gain of the antenna, and the impedance matching between the PD and the antenna. The PD plays an important role in the photonically driven emitters. PDs optimized for 1550-nm absorption can be fabricated on SiGe [37, 38] or III/V materials [39, 40]. The advantage of the SiGe PD is its compatibility with the existing large-scale silicon semiconductor fabrication industry, leading to higher integration levels and reductions in cost. However, the SiGe PDs suffer from low saturation power, which leads to low output power [37, 38]. The PDs based on III/V materials provide higher output power, lower dark current, and convenience in bandgap engineering. Thus, FUTC PDs were used in this application in order to achieve high-power and high-speed performance.

High radiated power was achieved in combination of the high-power PD and the high-gain antenna. The impedance of the fabricated PDs was characterized by a circuit model (Figure 2.6a) up to G-band. FI antennas, including the sinuous antenna, the spiral antenna, and the log-periodic toothed antenna shown in Figure 2.19, were selected for integration in the emitters due to their planar structures, high directivity, and broadband operation. The impedances of the FI antennas were investigated and simulated to include the effect of the substrate and the PD. Then, impedance matching between the PD and antenna was investigated.

Understanding the impedance of the PD is critical in achieving high radiated power out of the emitter. The model in Figure 2.6a was used to predict the impedance of the PD up through 220 GHz (G-band). The resulting measured and simulated impedances of the PDs with various sizes are plotted in Figure 2.20. Both the PD plus CPW model (red) and the PD model model alone (cyan) were simulated. Bandwidth measurements taken out to 225 GHz were also compared with the PD plus CPW model simulated bandwidth and can be seen in Figure 2.21(a)-(c). Bandwidth was measured for the 05-μm PD at 5-mA, the 10-μm PD at 10, 15, and 20-mA, and in the 14-μm PD at 10, 20, and 25-mA, all at -3 V bias. It should be noted that during the time of measurement, no more 05-μm PDs flip-chip bonded to CPW were available for higher power bandwidth measurements. The bandwidth was simulated for the 10-μm and 14-μm PDs at 10-mA, and at 5-mA for the 05-μm PD. Once the PD fitting model was verified with the measurements, the antenna impedance was simulated in ANSYS HFSS and incorporated with the PD to make a complete model of the emitter device.

The equivalent circuit models used for the simulation of effective isotropic radiative power

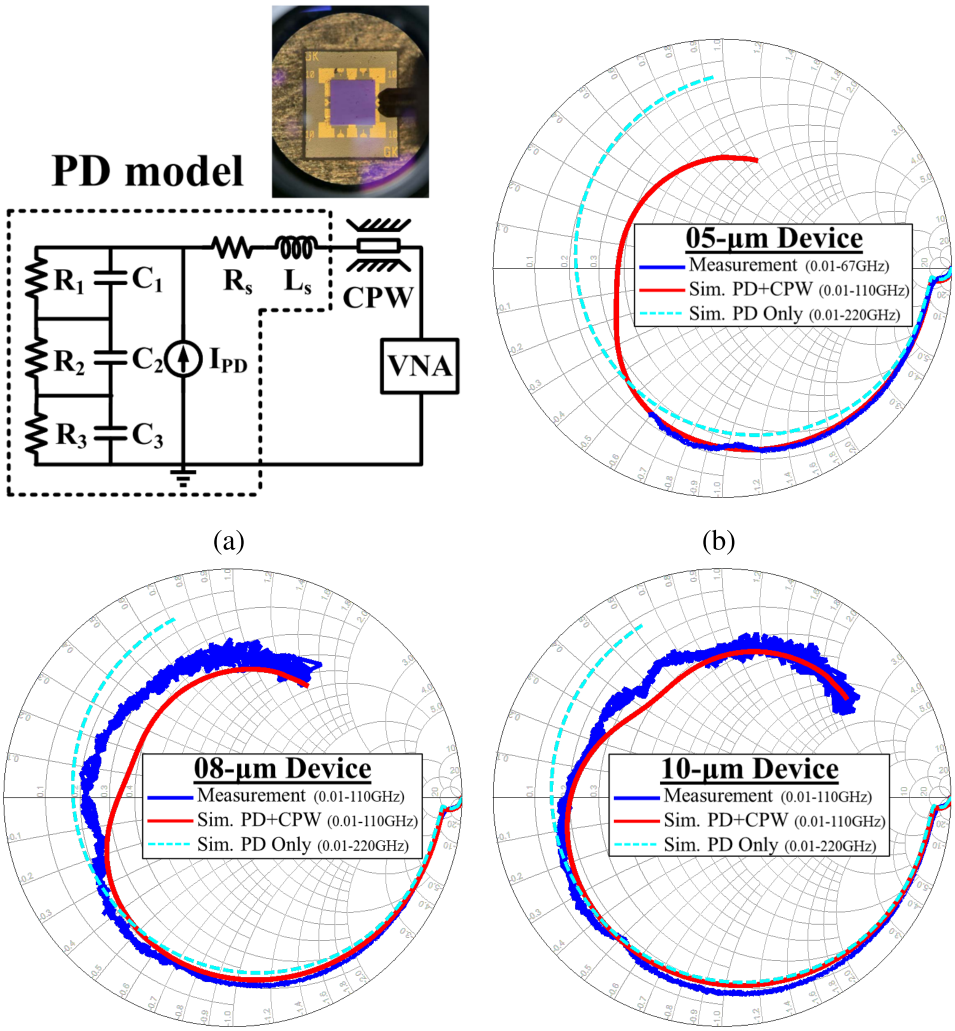

(a) (b)

(c) (d)

Figure 2.20: Circuit model of PD and VNA and microscope image of probed device (a) and fitting results vs. measured S11 data for 5-µm (b), 8-µm (c), and 10-µm (d) diameter PDs. [18]

(EIRP) are drawn in Figure 2.22. In Model 1, the PD model is directly connected to the antenna with the CPW section de-embedded. In Model 2, an extra capacitance C_p, is added to Model 1 to represent the parasitic effect introduced by the flip-chip bonding overlap of the air-bridge and metal on the submount. The simulated EIRP of all five emitters in the -Z-direction is plotted in Figure 2.23 for comparison with the measured results. For the first three emitters with 5-µm PDs, 5-mA photocurrent is used for simulation (I_0 = 5 mA in Equation 2.1 for I_{PD}), whereas 10-mA photocurrent (I_0 = 10 mA) is used for the last two emitters with the 8-µm PD and the 10-µm PD. The

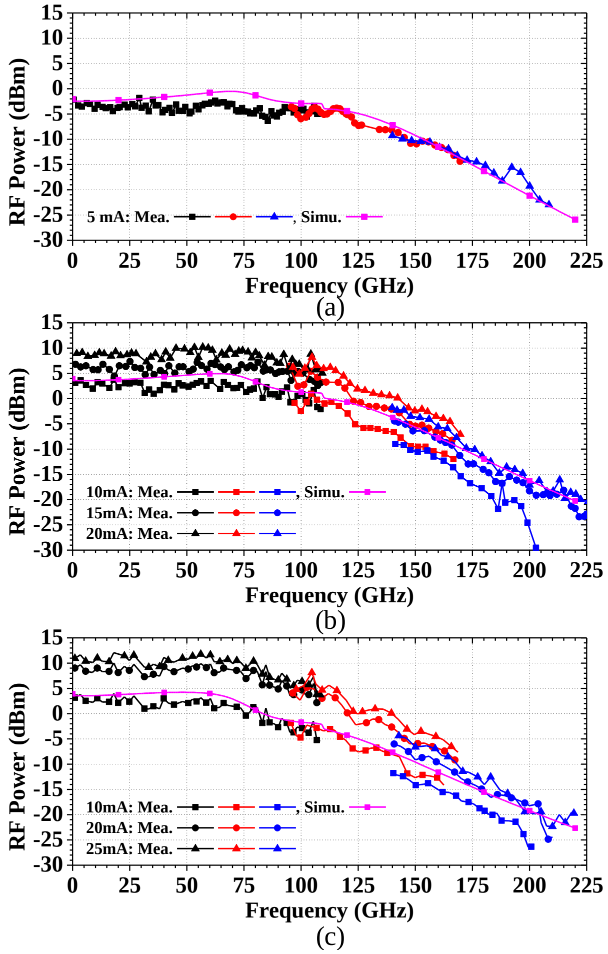

Figure 2.21: Simulated and measured RF output power of a 5-μm (b), 8-μm (c), and 10-μm (d) diameter PDs. [18]

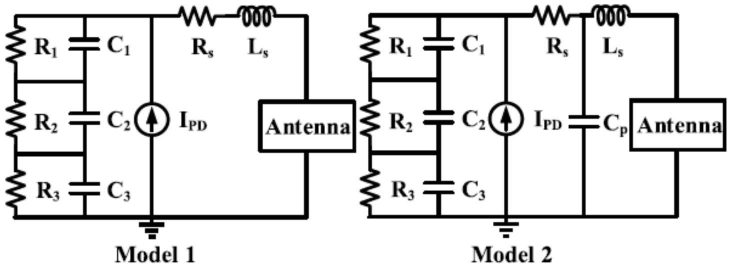

Figure 2.22: Equivalent circuit models used for the simulation of EIRP. [18]

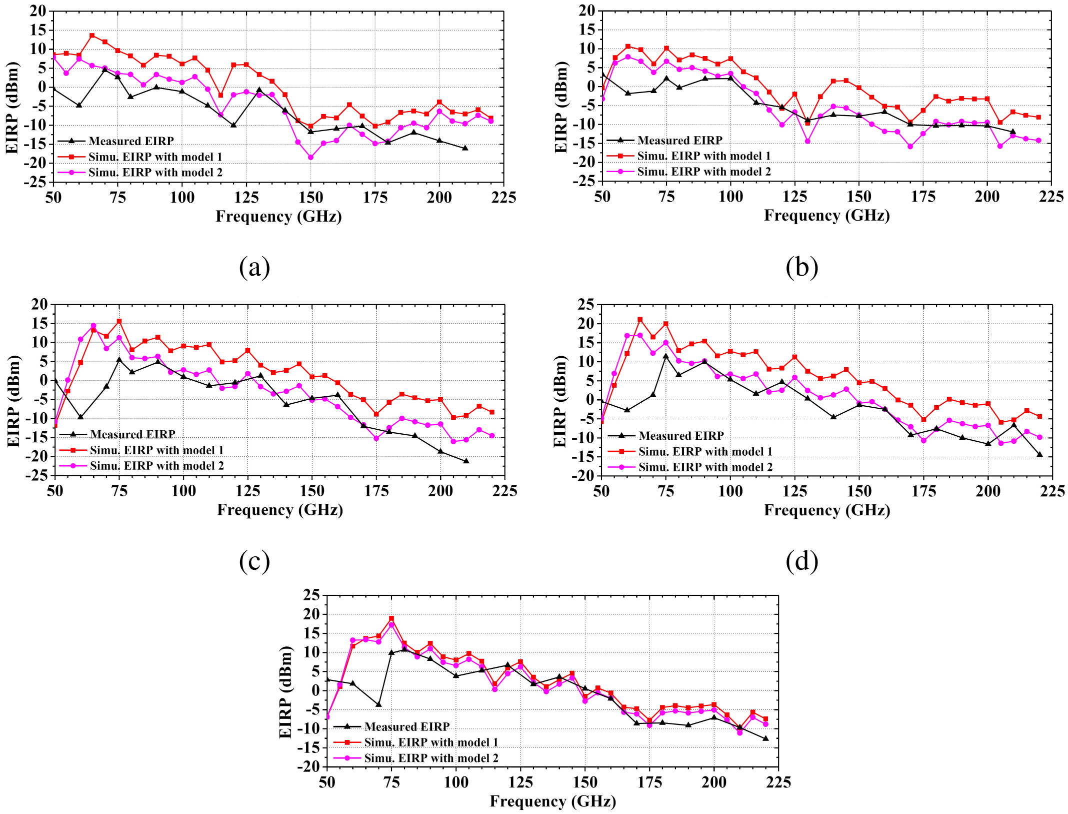

(a)

(b)

(c)

(d)

(e)

Figure 2.23: The simulated and measured EIRP of the emitter with (a) the log-periodic antenna with 5-µm PD, (b) the spiral antenna with 5-µm PD, and (c) the sinuous antenna with 5-µm PD, (d) the sinuous antenna with 8-µm PD, and (e) the sinuous antenna with 10-µm PD. [18]

simulated EIRP with Model 1 (red lines) agrees well with the measured EIRP for the emitter with the sinuous antenna and the 10-µm PD from 75 to 220 GHz in (e), but the simulated EIRP is on average between 5 and 8-dB higher than the measured EIRP for the other four emitters. This discrepancy may be attributed to the parasitics. When the PD is flip-chip bonded onto the antenna, the footprint of the PD may be partially misaligned with the GSG pad at the center of the antenna, introducing parasitic capacitance. Thus, a parasitic capacitance C_p is added in Model 2. Since the PDs in all five emitters are bonded individually, slightly different values of C_p are used for different emitters (5–18 fF). The simulated EIRP using Model 2 (magenta lines) agrees well with the measured results for all five emitters from 70 to 220 GHz. It demonstrates that even a small parasitic capacitance ($<$ 18 fF) may still have a significant effect on the matching at this frequency range. The discrepancy below 70 GHz may be due to the two bond wires providing bias for the PDs. Since these wires are bonded on the outer edge of the antennas, they mainly affect the impedance of the antenna in the lower frequency ranges. The emitter with the sinuous antenna achieved a record-high effective isotropic radiated power (EIRP) of 20-dBm while achieving a wideband response across 115 GHz of bandwidth (from 50 to 165 GHz) with the EIRP > 0 dBm. Meanwhile, the emitter with the spiral antenna demonstrated the flattest response with a 3-dB bandwidth of 34 GHz.

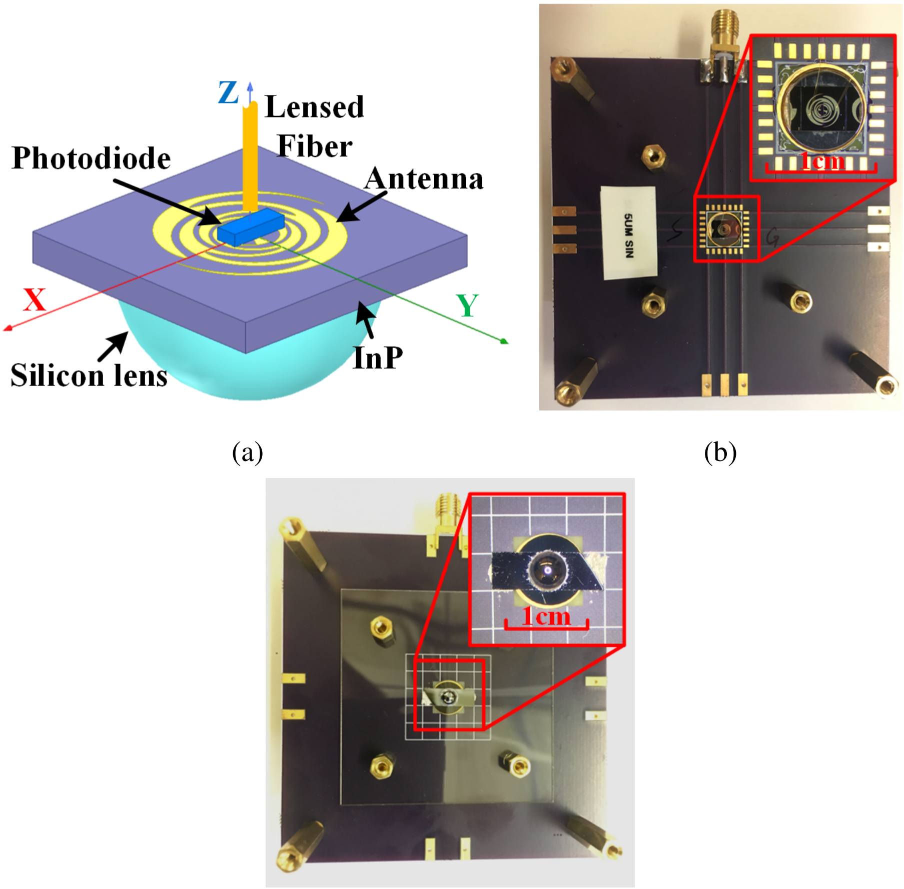

(a) (b)

(c)

Figure 2.24: (a) Structure of the integrated photonically-driven emitter, (b) top view and (c) bottom view of the emitter mounted on the PCB.[18]

The final structure of the integrated photonically driven emitter is shown in Figure 2.24a, which consists of the FUTC PD, an FI antenna fabricated on InP substrate, and a high-resistivity silicon (HRSi) lens attached to the bottom of the substrate. The two-arm FI antenna is composed of a layer of gold with a thickness of 2-μm and is fabricated on a 500-μm thick semi-insulating

InP substrate. At the center of the antenna, a ground-signal-ground (GSG) pad is fabricated as the footprint for the PD. The InP substrate is mounted on a printed circuit board (PCB) as shown in Figure 2.24b. Two wirebonds are connected from the outer edge of each arm of the antenna to the PCB in order to provide the DC bias for the PD. Because the outer edge of the antenna determines the low-frequency limit of the bandwidth, the antenna is fabricated slightly larger than required in order to avoid affecting the radiation pattern in the lower end of the frequency band. Within the operating frequency range, the inductive wirebonds present a high impedance, effectively isolating the dc bias from the high frequency signals.

The PD is directly flip-chip bonded onto the antenna, which helps minimize the parasitics between them when compared to assemblies based on discrete components. At frequencies up towards the G-band, discrete component assembly would be difficult. However, there are still tolerances in mechanical accuracy when flip-chip bonding and with PD feature sizes as small as 5-µm, we expect to see some parasitics introduced, making wideband impedance matching difficult. As shown in Figure 2.23 parasitic capacitance smaller than 18 fF (model 2, C_p) introduced by the flip-chip bonding significantly changed the impedance matching between the antenna and the PD, lowering the EIRP by 5–8 dB. However, the parasitic capacitance is unpredictable before integration because the flip-chip bonding process is a mechanical process with tolerances in accuracy. Additional simulations show that a variation of 3-fF capacitance will significantly change the impedance matching at this high-frequency range.

In summary, high-power V-band to G-band (50 GHz to 220 GHz) photonically-driven electromagnetic emitters, composed of frequency-independent (FI) antennas and charge-compensated modified uni-traveling carrier photodiodes (FUTC PDs), are demonstrated. The designed and fabricated PDs achieve a responsivity of 0.2 A/W and are able to provide up to 12 dBm output power. The impedances of the PD and the FI antennas (the sinuous antenna, the spiral antenna, and the log-periodic antenna) are characterized, showing that different antennas could be selected to provide either highest radiated power or widest bandwidth depending on applications. The measurement results indicate that the integrated emitter with the sinuous antenna and the 8-µm PD achieves a record-high broadside effective isotropic radiated power (EIRP) of 20 dBm with an optical-to-THz power conversion efficiency of 15.7% while maintaining EIRP greater than 0 dBm up through 115 GHz of bandwidth (50 - 165 GHz). The emitter with the spiral antenna and the 5-µm PD provides a wide 3-dB bandwidth of 34 GHz with a maximum EIRP of 8.8 dBm. These high-power wideband emitters can be used for wireless communications, mm-wave and sub-THz imaging, and radar systems.

Chapter 3

High-Speed Integrated Waveguide FUTC Photodiodes

In another PD-centric project, I had the opportunity to help my colleague and friend Bassem Tossoun with the CPW microwave design and modeling, fabrication, and measurement and characterization of high-speed integrated waveguide FUTC PDs for low-power applications. While high-speed and high-power are necessary performance metrics for the applications previously mentioned, there are also low-power applications that benefit from high-speed photodiodes. High-speed, low-capacitance photodiodes are key components in low-power optical receivers for data communication and processing. According to Miller [41], reducing the photodiode capacitance can help enable a ‘receiverless’ system, meaning there is no need for a transimpedance amplifier (TIA) following the photodiode. Because the photodiode capacitance is sufficiently small, the self-induced electric field caused by photogenerated carriers will create a strong enough voltage swing to drive the input of a CMOS gate with the incorporation of a high load resistor [42]. This not only simplifies the system, but has the potential to reduce the energy consumption per bit of an optical receiver by over 100x.

To this end, we demonstrated a modified uni-traveling carrier (FUTC) waveguide photodiode with an ultralow capacitance of 1.8 fF, 0.26 A/W external responsivity, and a bandwidth up to 85 GHz at -1 V and 50 GHz at zero bias. In normal incidence photodiodes, reduced depletion width and device area, can reduce the carrier transit-time and RC time constant, respectively, which ultimately makes a faster device; however, this comes at the cost of efficiency (responsivity) due to absorption and carrier transit occurring in a parallel direction. To achieve simultaneous high-speed high-efficiency performance, as would be necessary in a CMOS gate application, waveguide-coupled photodiodes offer carrier collection perpendicular to light absorption, allowing the absorber to remain thin but extend in length leading to higher efficiency, as compared to normal incidence PDs. In addition to this speed and efficiency benefit in waveguide PDs, in order to reduce capacitance by reducing device size, a newly designed planarization and passivation process was developed and devices as small as 2 x 2-µm in size were successfully fabricated with reduced device parasitic capacitances for potential high bandwidth, 'amplifier-less' optical receivers.

3.1 Device Design and Fabrication

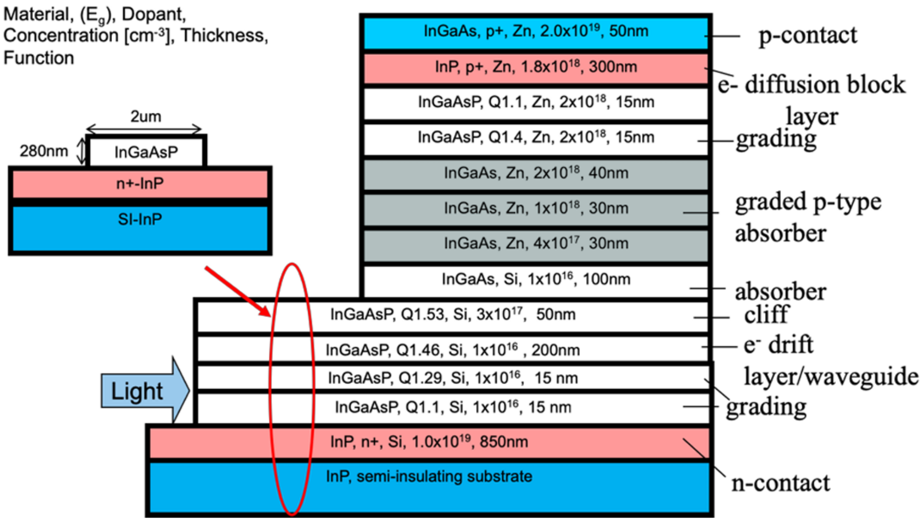

Figure 3.1: Epitaxial layer stack of WG-FUTC.[43]

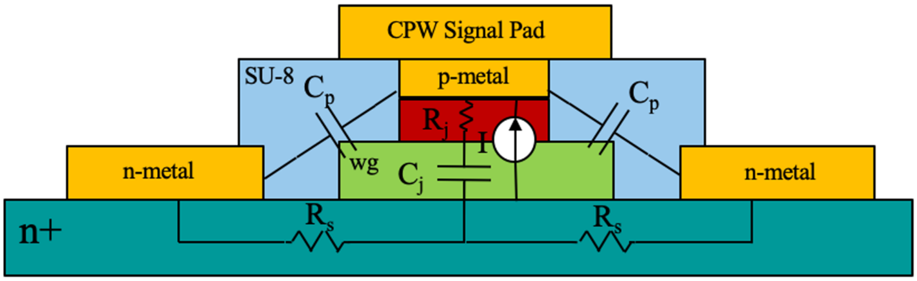

Figure 3.2: Cross-section with circuit elements of the WG-FUTC PD and planarized SU-8.[43]

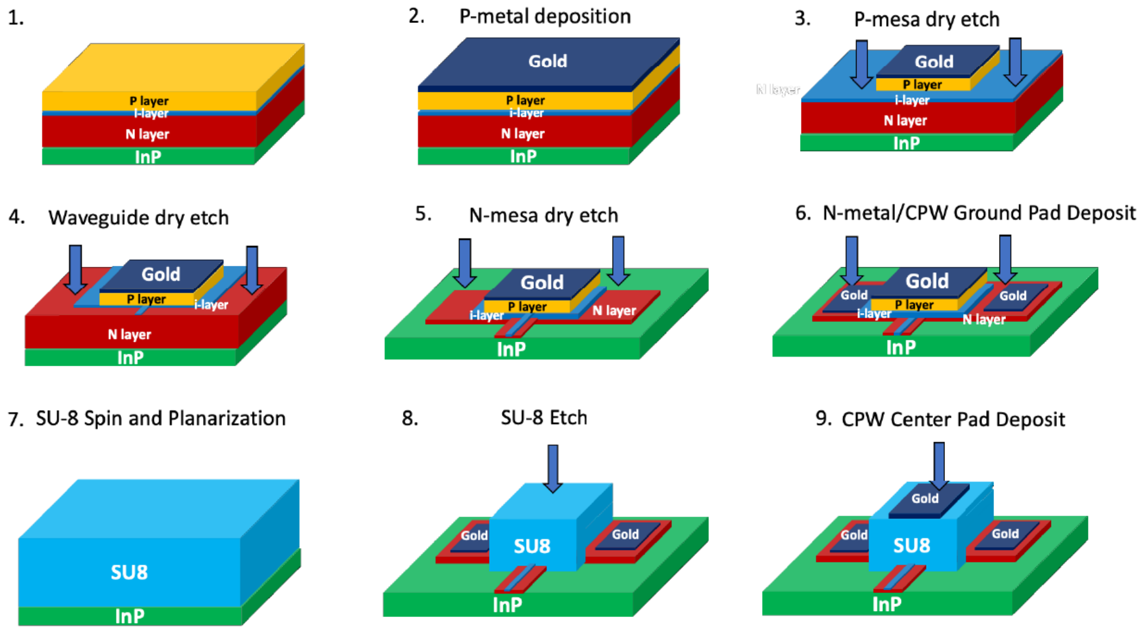

Figure 3.3: Fabrication flow for WG-FUTC using SU-8 planarization process.[43]

Figure 3.1 shows the epitaxial layer stack of the photodiode, which was grown with metal-organic chemical vapor deposition (MOCVD). Figure 3.2 shows the circuit elements introduced from the SU8 planarization process. Following along with Figure 3.3, the first step for device fabrication was to deposit Ti/Pt/Au/Ti, the p-contact metal, on top of the sample using electron beam evaporation. Then, silicon dioxide (SiO_2) was deposited as a hard mask for the p-mesa etch. After the p-mesa was etched, then the waveguide and the n-mesa were dry etched. Next, Ti/AuGe/Ni/Au was deposited on top of the n-mesa to serve as the n-contact metal, as well as, the coplanar waveguide (CPW) ground pads. SU-8 was then used to passivate the sidewalls of the device and reduce leakage current, as well as, serve as an insulation pad and interconnect supporting structure for the RF signal pad. After SU-8 was deposited and planarized on the surface of the chip, it was dry etched with O_2 and SF_6 until the p-metal was exposed. Then, 30 nm of Ti and 400 nm of Au were deposited for the CPW signal pad. This novel planarization process eliminates the need for an air bridge and its precise and difficult alignment to the p-mesa. Lastly, the chips were cleaved using a cleaving tool. An SEM photo of a fabricated WG-FUTC PD is shown in Figure 3.4.

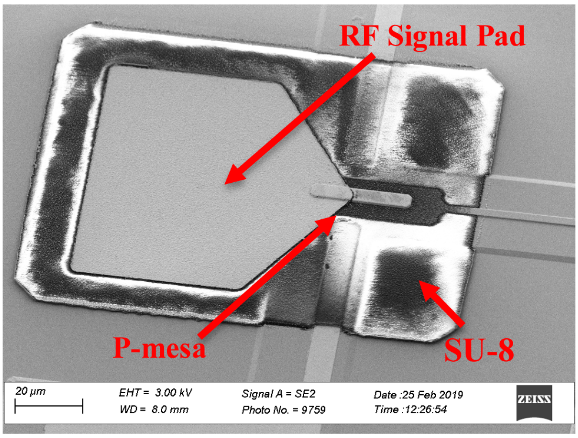

Figure 3.4: SEM photo of fully fabricated 5-µm x 30-µm WG-FUTC PD.[43]

3.2 Device Characterization

I-V curves were taken of the devices and are shown in Figure 3.5a. The dark current is as low as 5 nA at -1 V for a 2-µm x 2-µm photodiode. Capacitance-voltage (C-V) measurements were also taken using an LCR meter showing that the junction capacitance scales linearly with area as shown in Figure 3.5b. A junction capacitance as small as 1.8 fF was measured for a 3-µm x 3-µm device at -1 V, and the parasitic capacitance coming from outside the device, C_p, was measured to be about 1 fF. Due to the new planarization process and optimized CPW designs, the capacitances of these devices were more than 10x lower than the smallest devices fabricated in previous similar designs [44]. The external responsivity at 1550 nm was measured using a 2-µm spot size lensed fiber to be about 0.26 A/W for a 5-µm x 7-µm PD. The RF frequency response was also measured at 1550 nm and is shown in Figure 3.5c. We recorded a 3-dB bandwidth as high as 85 GHz at -1 V, and a 3-dB bandwidth of 50 GHz at 0 V for a 5-µm x 7-µm photodiode.

It is worth noting that the photodiode is able to produce high speed RF output power at zero-bias. This is beneficial because of zero leakage current, saving idle power consumption in an optical receiver. It is also advantageous because it simplifies heat sinking, reduces biasing circuit cost, and improves reliability [45]. Furthermore, even with a large load resistor, the measured capacitance allows for a high 3-dB bandwidth to still be maintained. Also, since the capacitance is ultra-low, the photogenerated charges in the photodiode produce a large enough voltage swing across the high resistance load resistor to supply a CMOS logic gate, eliminating the need of a TIA.

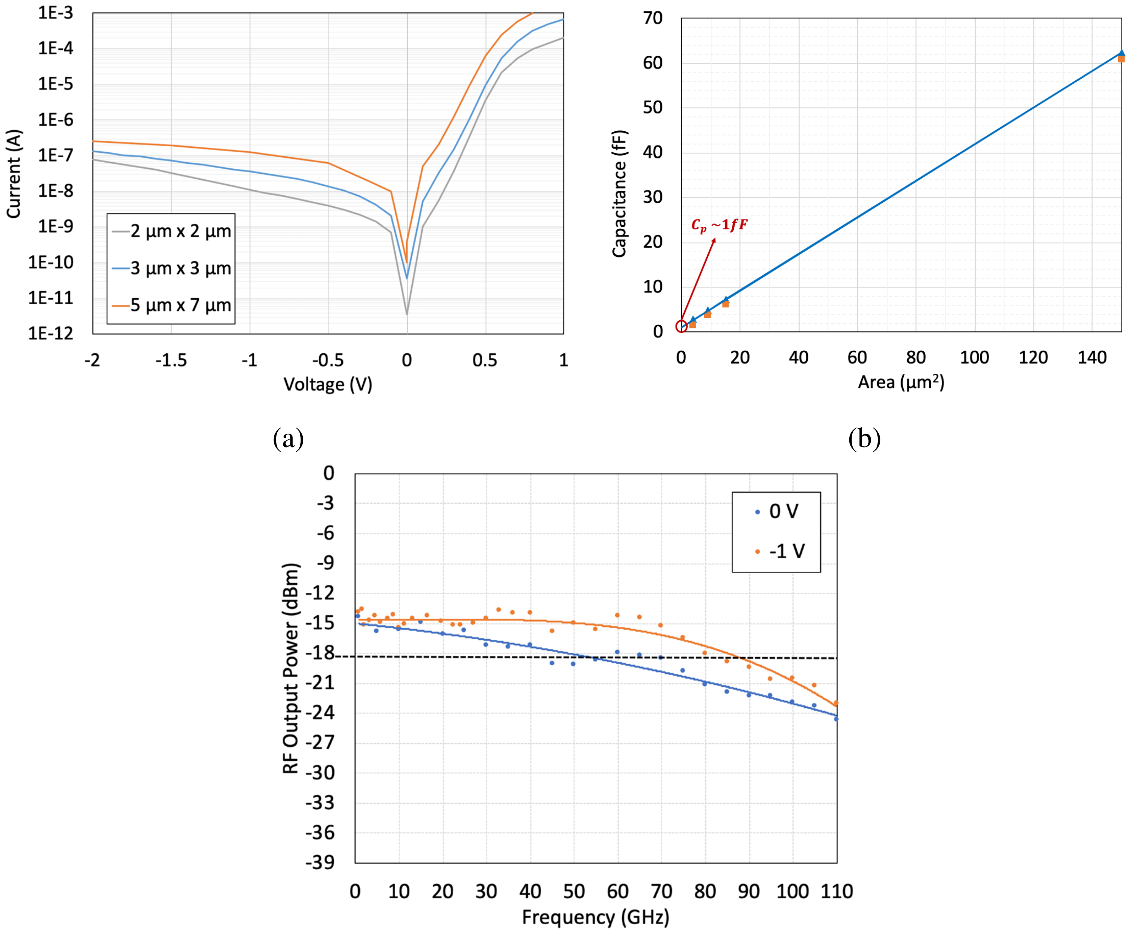

(a) (b)

(c)

Figure 3.5: (a) I-V curves of WG-FUTC PDs with different sized active areas, (b) measured (blue dots) and calculated (orange dots) capacitance vs. PD active area size, with linear fit representing linear fit of the measured data and (c) measured frequency response of a 5-µm x 7-µm PD with curves showing averaged data.[43]

Chapter 4

FUTC PDs for Soliton Excitation

In collaboration with Professor Xu Yi's research group, I worked with Beichen Wang, to create a measurement setup, measure, and characterize the RF performance of microresonator solitons as an excitation source for FUTC PDs. The recent development of dissipated Kerr solitons in microresonators [46, 47, 48, 49, 50, 51] provides an integrated solution to address the challenges of photonic-generated mmWaves in both power and coherence. These solitary wave packets achieve mode-locking by leveraging Kerr nonlinearity to compensate cavity loss and to balance chromatic dispersion [46, 52]. Microresonator solitons have been applied to metrology [53], optical communications [54] and spectroscopy[55, 56] in the form of microresonator-based frequency combs (microcombs)[57]. Due to the miniaturized dimension, the repetition rate of microresonator solitons ranges from a few GHz to THz [58, 59]. Direct detection of the solitons with a fast photodiode produces mmWave at the repetition frequency of the solitons. When compared with the conventional two laser heterodyne detection method, the soliton mode-locking provides up to 6-dB gain in mmWave output due to the constructive interference among beatnotes created by different pairs of neighboring comb lines [60]. This additional gain is of great importance at high frequencies, since it can relax the bandwidth requirements in the photodiode. In terms of signal coherence, recent studies have shown that the phase noise of the soliton repetition frequency at 10's of GHz can be orders of magnitude smaller than that of its pump laser [61, 47, 62, 63]. When microresonator solitons are married with integrated lasers [64, 65], amplifiers [66], and high-speed photodiodes [67] through heterogeneous or hybrid integration, a fully integrated mmWave platform can be created with high power, high coherence performance and the potential for large scale deployment through mass production (Figure 1.1). Working towards this platform, this project used surface normal FUTC PDs and integrated microresonators to demonstrate the coherent, high-power, high-speed performance attainable from soliton excitation. A 5.8-dB improvement over sinusoidal mmWave power for a given photocurrent, a maximum output power of 6.7-dBm, and mmWave 3-dB linewidth of 7-kHz were achieved at 100-GHz operating frequency. An illustration of the power enhancement attainable through optical frequency comb generation over heterodyne generation is show in Figure 4.1.

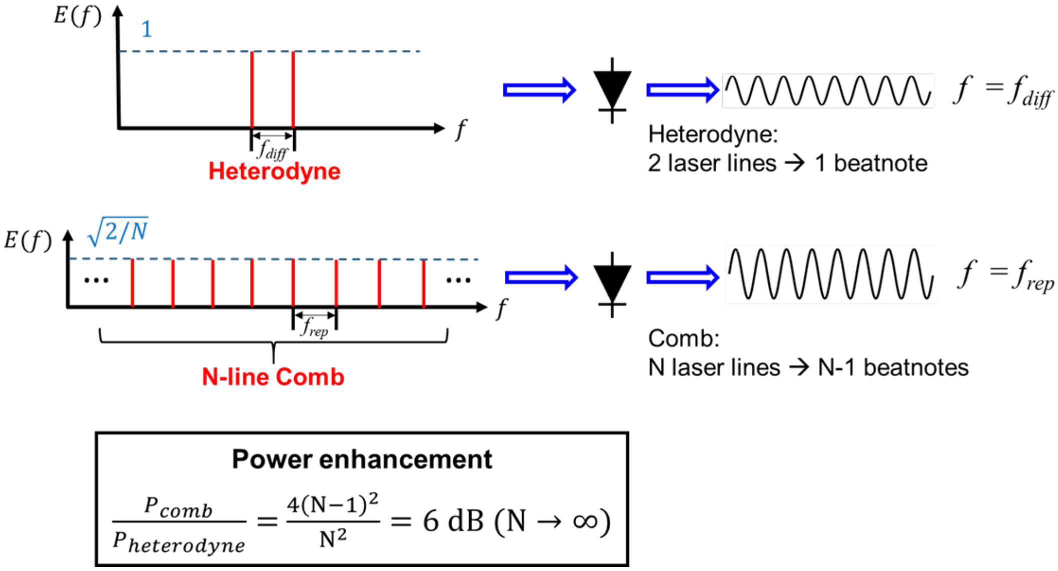

Figure 4.1: Illustrated principle behind power enhancement within linear range of PD operation showing normalized optical power vs. optical signal lines for heterodyne excitation (top) and optical frequency comb excitation (bottom).

In conventional heterodyne detection, mmWaves are generated when two laser lines mix with each other on a photodiode and create one beat note. However, when using an optical frequency comb, each comb line will beat with its two adjacent neighbour lines to create beatnotes at the comb repetition frequency. For a comb that consists of N comb lines, $(N-1)$ beat notes will be created at the comb repetition frequency. Therefore, for the same average optical power, the comb can produce up to twice the number of beatnotes per laser line than heterodyne detection, and thus generate twice the AC photocurrent. Factoring in this boost in power to Equation 1.9, the output power from the photodiode at the comb repetition frequency can be described as [10, 60]:

$$P_{PD} = \frac{I_{DC}^2 R_L}{2}\left[\frac{2(N-1)}{N}\right]^2 \times \Gamma, \tag{4.1}$$

where I_{DC} is the average photocurrent, R_L ($50\ \Omega$) is the load resistor, and $N \geqslant 2$ is the number of comb lines. Γ is the measured relative mmWave power roll-off for the photodiode, and is ~ 5.5

dB for the 7-µm and $\sim$ 6 dB for the 8-µm diameter PDs used in this work at 100 GHz. Clearly, the power at the limit of $N \rightarrow \infty$ is 4 times (6 dB) higher than the power of heterodyne detection, where $N = 2$.

In practice, however, conventional frequency combs are not the best candidates to achieve the 6 dB gain for mmWave generation due to their low repetition frequencies. Previously, two attempts with electro-optics modulation frequency combs were reported, where line-by-line amplitude and phase shaping was used to remove the unnecessary comb lines and increase the repetition rate from 20 GHz to 100 and 160 GHz [60, 68]. This post spectral filtering nonetheless increases the complexity and cost of the system. Conversely, microresonator solitons have comb repetition rates ranging from a few GHz to 1 THz, and can be directly applied to mmWave generation. MmWave generation with soliton microcombs in tapered-coupled microtoroid resonator [69], from dual-comb structure [70], and from a pair of comb lines [71] have been shown, but there was no investigation into the output power from the PD.

4.1 Experimental Setup

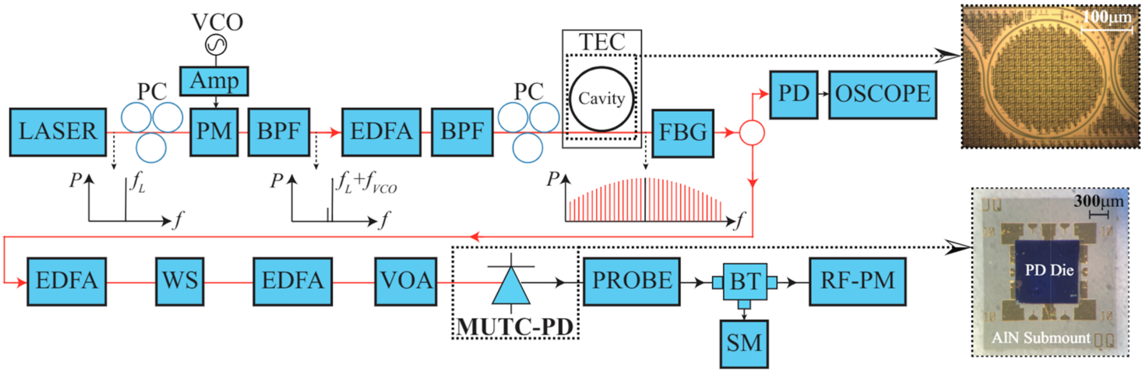

Figure 4.2: Experimental setup for microresonator soliton and photodiode experiment.[72, 6]

The experimental setup is shown in Figure 4.2. A continuous wave (CW) laser (f_L) feeds through a polarization controller (PC) and into a phase modulator (PM). The microresonator's pump laser is then derived from the CW laser's first phase modulated sideband ($f_L + f_{VCO}$) and tuned rapidly by a voltage-controlled oscillator (VCO) until the pump laser enters the red-detuned regime of the resonator. The soliton frequency comb is generated with a $Sech^2$ envelope optical spectrum. A thermoelectric cooler (TEC) sitting beneath the resonator mitigates environmental fluctuations to maintain the laser-cavity detuning within the soliton existence range. A fiber Bragg grating (FBG) filters out the pump laser and 10% of the comb power is fed into a commercial photodiode (PD) and monitored on an oscilloscope (OSCOPE) while 90% of the comb power is amplified in an erbium-doped fiber amplifier (EDFA) and transmitted through a 70-m long optical fiber. Because the soliton was generated in our collaborator's lab in another room in our building, we had to run a 70-m long optical fiber to our lab for the experiment. A programmable optical waveshaper (WS) is used to overcome group velocity dispersion effects in the fiber and EDFA and to suppress the amplified spontaneous emission (ASE) noise of the EDFA. A variable optical attenuator (VOA) controls the optical power incident on the FUTC, which is back-illuminated through a fiber collimator. A high frequency rectangular waveguide (WR) GSG RF probe extracts the electrical signal from the PD. A source-meter (SM) monitors the photocurrent and biases the PD through an integrated bias-tee (BT) on the probe, and a RF power meter (RF-PM) records the power.

4.2 Results and Characterization

The dissipated Kerr solitons used in this work are generated in an integrated, bus-waveguide coupled Si_3N_4 micro-ring resonator with free spectral range (FSR) of $\sim$100 GHz. The experimental setup is shown in Figure 4.2. The single soliton state with a 35.4 fs pulse width is generated and its squared hyperbolic secant spectral envelope is characterized by an optical spectrum analyzer (Figure 4.3a. The spectrum has sech^2 spectral envelope (fitting shown in dashed red line). The pump laser is suppressed by a fiber Bragg grating filter. The comb is then amplified by an erbium-doped fiber amplifier (EDFA) and sent to the photodiode, and an optical programmable waveshaper (WS) is used to compensate the group velocity dispersion and to suppress spontaneous emission (ASE) noise from the EDFA. The inset of Figure 4.3a shows the optical spectrum after the amplification and dispersion compensation. A microscope picture of the microresonator is shown in Figure 4.3b.

To characterize the 6 dB power increase from the microresonator solitons, the PD output powers are measured for both microresonator soliton detection and heterodyne detection on four of our PDs with 7, 8, 10, and 11-µm diameters. The heterodyne measurements are performed using two continuous-wave lasers with the same optical power and polarization. A variable optical attenuator is used to control the optical power illuminating on the PD. In the linear region of PD operation, the 100 GHz mmWave powers at different photocurrents are shown in Figure 4.3c for the 7-µm device. The DC photocurrent is a direct measurement of the optical power illuminating on the PD. In the experiment, the coupling distance from fiber to PD is increased for a uniform illumination,

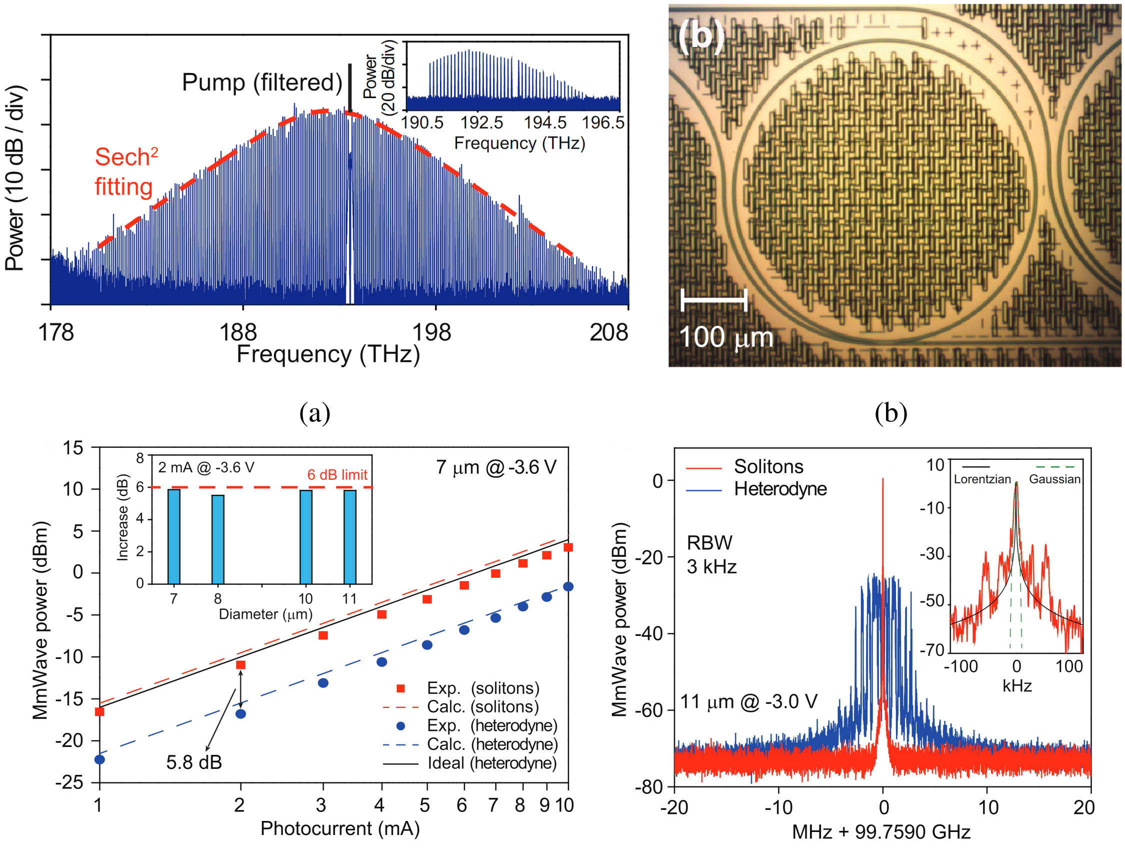

(a) (b)

(c) (d)

Figure 4.3: (a) Optical spectrum of single soliton state from the microresonator. The spectrum has sech^2 spectral envelope (fitting shown in dashed red line). (b) Microscope image of integrated Si_3N_4 microresonator with 100 GHz free spectral range (FSR). (c) 100 GHz mmWave output power measured for microresonator solitons (red) and optical heterodyne detection of two cw-lasers (blue) (d) Down-converted electrical spectrum of 100 GHz signal generated with free-running microresonator solitons (red) vs. the signal generated from heterodyne method shown in blue trace.[6]

resulting in 1 mA photocurrent for 11 mW optical input power. The mmWave power generated from the microresonator solitons is measured to be 5.8 dB higher than that of heterodyne detection. This power increase is approaching the 6 dB theoretical limit, and is verified on all four PDs with different diameters (shown in the inset of Figure 4.3c). As a result of the 6 dB power increase, the mmWave power generated using microresonator solitons is within 1 dB of the theoretical power limit of heterodyne detection (solid black line in Figure 4.3c), where the detector is assumed to be ideal and has no power roll-off at mmWave frequency. It shall be noted that no optical spectrum flattening is applied in our measurement. For 5.8 dB power improvement, a 3 dB bandwidth of 7 comb lines is required for the Sech^2 or Gaussian spectral envelope, and the shape of the spectral envelope has little effect on mmWave power when the number of comb lines is large [6].

The electrical spectrum of the 100 GHz mmWave signal is measured and shown in Figure 4.3d. Limited by the available bandwidth of our electrical spectrum analyzer, we down convert the 100 GHz mmWave by sending it to an RF mixer to mix it with the fifth harmonic of a 20.2 GHz local oscillator. The mixer generates a difference frequency at $\Delta f = 5f_{LO} - f_r$. Δf is measured to be 1.2410 GHz, and we can derive the mmWave frequency as $f_r = 99.7590$ GHz. A low-noise, narrow signal is clearly observed at 3 kHz resolution bandwidth (RBW) in Figure 4.3d (red trace). The signal is fitted with a Lorentzian, and the 3-dB bandwidth is 0.2 kHz (zoomed-in panel in Figure 4.3d). Note that the soliton repetition rate is subject to fluctuations (laser frequency drift, temperature, etc.), and the central part of the signal is Gaussian with 3-dB linewidth of 4 kHz. This narrow linewidth at 100 GHz frequency is obtained for a free-running microcavity soliton, which is driven by a pump laser with significantly broader linewidth ($\sim$ 200 kHz, New Focus 6700 series specification). We note that there are a few bumps around 50 kHz offset frequency, which are likely to be derived from the technical noise of the pump laser. To compare the signal coherence between conventional heterodyne method and the soliton method, the heterodyne signal of beating the pump laser and another 6700 series New Focus laser is also measured and shown in Figure 4.3d (blue trace). At the same RBW, the heterodyne signal has poor coherence and its frequency is drifting > 5 MHz. Our measurements show that using free-running microcavity solitons can reduce the linewidth of mmWave signals by 2 orders of magnitude, giving the microresonator soliton platform a key advantage over conventional heterodyne detection. No RF reference is used to stabilize the mmWave; in fact, the only controls used are the coarse temperature controls of the laser and the microresonator, used to offset the change in environmental temperature.

Next we verify the dependence of mmWave power increase on the number of comb lines, which is described in Equation 4.1. A line-by line waveshaping filter is used to select the number of comb lines that pass to the FUTC PD. We test the number of comb lines from 2 to 22 at four different photocurrent levels (optical power), and the result is shown in Figure 4.4a. Three representative optical spectra for 2, 12, and 22 comb lines are shown in Figure 4.4b. The measured mmWave power follows the calculated curves. Interestingly, a 3 or 5 dB increase of power only requires 4 or 9 comb lines. This relatively small demand for comb lines relaxes the microresonator soliton requirement in terms of its optical bandwidth.

The increase of mmWave power only happens when the beatnotes generated by different

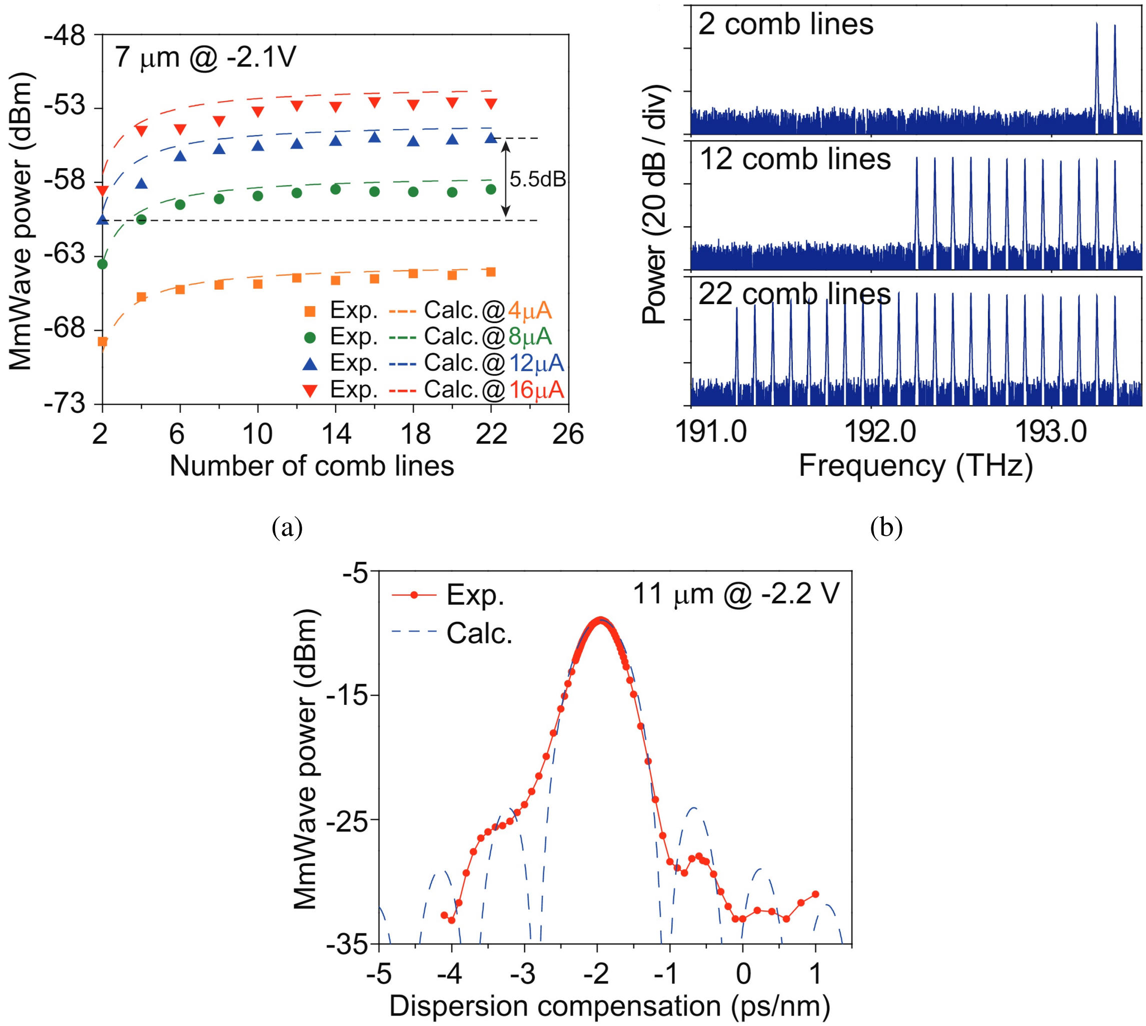

(a) (b)

(c)

Figure 4.4: (a) MmWave power at 100 GHz for different number of comb lines at four different photocurrents with the theoretical calculation based shown in dashed lines. (b) Corresponding optical spectra of two, twelve and twenty-two comb line measurements in panel (a). (c) MmWave power versus dispersion compensation added by waveshaper, d_c with a theoretical curve from Equation 4.2 shown in dashed line.[6]

pairs of comb lines are in constructive interference. This is not always the case if there is dispersion between the microresonator and the PD. This effect is studied by applying programmable dispersion using a waveshaper. The measurement of mmWave power versus waveshaper dispersion is shown in Figure 4.4c. The effect can be calculated analytically by adding phase to each comb line, and will modify Equation 4.1 to:

$$P_{PD} = \frac{I_{DC}^2 R_L}{2} \left[\frac{2\sin\left[(N-1)\pi c d f_r^2/f_p^2\right]}{N \sin\left[\pi c d f_r^2/f_p^2\right]} \right]^2 \times \Gamma, \tag{4.2}$$

where c is the speed of light, and $d = d_0 + d_c$ is the accumulated group velocity dispersion between the microresonator and PD. d_0 denotes the offset dispersion in the system introduced by fibers and amplifiers, and d_c represents the dispersion compensation added by the waveshaper. The derivation of Equation 4.2 is shown in the Materials and Methods section in [6]. The measurement and theory prediction agree very well when an offset dispersion of $d_0 = 1.95$ ps/nm is included. The offset dispersion exists in our system because of the 70 meter fiber used to connect the microcomb lab and photodetector lab (contributing 1.26 ps/nm), with the rest of the dispersion coming from the fibers in the EDFA. N is used as a free parameter for fitting the experimental curve, and $N = 15$ is used for the dashed line in Figure 4.4c. The fitted N should be interpreted as the effective number of comb lines to account for the spectral envelope shape. When the entire system is fully integrated, the overall length of waveguides will be well below a meter, and the dispersion will not impact the mmWave power.

We obtain a maximum output power of 7 dBm at 22.5 mA for the 8-µm device shown in Figure 4.5a. Using Equation 4.1 we find that the ideal heterodyne response for this 8-µm device would need 26.7 mA to achieve 7 dBm, which means we can produce the same power at lower average photocurrent using soliton excitation. The 7 dBm saturation power is recorded at -3.6 V bias. Increasing the reverse bias can improve the saturation power, however, ultimately this can cause PD thermal failure [73], which is due to the rise in junction temperature from the dissipated power in the PD (reverse bias × average photocurrent). One advantage of using solitons is that they can generate the same RF output power at a lower photocurrent than the two-laser heterodyne method, and thus can reduce the dissipated power and allow the PD to be operated further below the point of thermal failure.

We further characterize the phase noise of the mmWaves generated from the free-running microcavity solitons, and compare it to the phase noise from the heterodyne method. Similar to the linewidth measurement, the 100 GHz mmWave signal is down converted in an RF mixer where it is mixed with the fifth harmonic of a 20.2 GHz local oscillator. To minimize the effect of frequency drifting in the phase noise measurement, the frequency of the down-converted signal is further divided down electrically by a factor of 14 and 100 for the soliton and heterodyne, respectively. The phase noise is then measured in the electrical spectrum analyzer with direct detection technique,

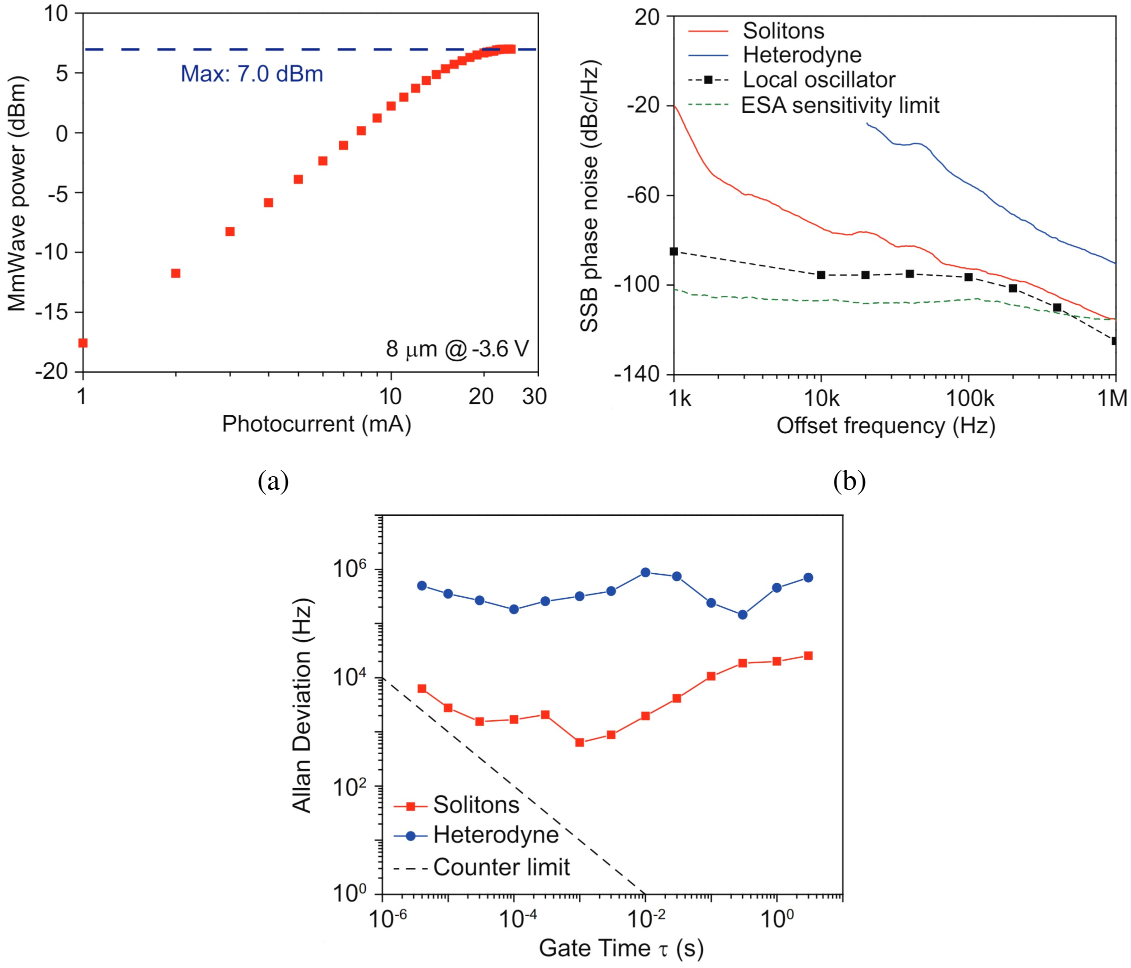

(a)

(b)

(c)

Figure 4.5: (a) Maximum power of 7 dBm is reached at 22.5 mA and −3.6 V bias voltage in the $8\mu m$ device. (b) Phase noises of the free-running soliton-based mmWave (red) and the heterodyne mmWave (blue) at 100 GHz. The measurement sensitivity floor is set by both the ESA sensitivity limit (dash green), and the local oscillator phase noise (dash black). (c) Allan deviation of the free-running soliton-based mmWave (red) and the heterodyne mmWave (blue).[6]

and the result (at 100 GHz) is shown in Figure 4.5b. Due to the large frequency drift, the heterodyne phase noise below 20 kHz offset frequency cannot be accurately characterized and thus is not presented. The soliton phase noise beyond 100 kHz is potentially limited by the measurement sensitivity, which is set by the noise floor of the spectrum analyzer (dash green), and the phase noise of the local oscillator (Keysight, PSG E8257D) used to down-convert the mmWave (dash black).

The measurement shows that the free-running solitons can reduce the mmWave phase noise by $>$ 25 dB from the heterodyne method. The reduction of phase noise from the pump laser frequency to the soliton repetition rate is a result of the noise transfer mechanism in microresonator solitons [62]. Our observation is in agreement with the previous reports of X-band and K-band microwave generation with microresonator solitons [62, 63, 74]. The phase noise of soliton-based mmWaves can be further reduced in the future by using a pump laser with higher stability [75], tuning the soliton into quiet operation point [62], and implementing better temperature control of the entire system. For instance, a compact external-cavity diode laser has achieved Lorentzian linewidth of 62 Hz recently[76]. Using this laser to drive the soliton could further reduce the free-running mmWave phase noise.

Finally, the Allan deviations of the mmWave generated from the soliton and the heterodyne detection are measured by counting the frequency of the down-converted signal on a zero dead-time counter (Figure 4.5c). At 1 ms gate time, the Allan deviation of the soliton-based mmWave reaches the minimum of $<$ 0.7 kHz, which is more than two orders of magnitude better than that of the heterodyne detection. Above 1 ms gate time, the Allan deviation of the soliton-based mmWave increases due to the drift of pump laser frequency and temperature fluctuation. Stabilizing the mmWave signal to a low frequency reference could provide long term stability, which will increase the system complexity, but is possible through the electro-optics modulation method [71], or dual microcavity soliton methods [53, 77].

In summary, we have demonstrated high-power, high-coherence mmWave generation at 100 GHz by using integrated microresonator solitons and FUTC PDs. The solitons, being inherently mode-locked, are measured to provide 5.8 dB additional gain through constructive interference among mmWave beatnotes, and the absolute mmWave power approaches the theoretical limit of conventional heterodyne detection at 100 GHz. In our free-running system, the soliton is capable of reducing the mmWave linewidth by two orders of magnitude from that of the pump laser. Our work leverages microresonator solitons and high-speed modified uni-traveling carrier photodiodes to provide a viable path to chip-scale high-power, low-noise, high-frequency sources for mmWave applications. Extending the frequency to several hundred GHz is possible. The proposed platform has the potential to be fully integrated on a single chip which can enable large-scale mmWave arrays. The four critical components: laser, Kerr microresonator, amplifier, and ultrafast photodiode, have all been shown to be compatible with Si_3N_4 photonic platforms through heterogeneous integration. Once all components are fully integrated, we expect that the platform can deliver a new paradigm regarding scalable, integrated photonics technologies for applications at very high frequencies, and thus provide a path to compact, low-noise high-frequency sources for spectroscopy, ranging, and wireless communications.

Chapter 5

Other MmWave Work

While the majority of this body of work revolves around FUTC PDs, two other projects at mmWave operating frequencies are worth noting as contributions towards the motivation behind photonic-based mmWave systems. The first, work towards an optically modulated scatterer probe operating at 60 GHz, was done with my friend and colleague Jizhao Zang and involved the development of an optoelectronic device that could be modulated around a resonant frequency, by designing a photovaractor semiconductor device and mmWave resonant network. The second, working with ultra-fast Germanium photodiodes (Ge PDs) designed and fabricated by our colleagues in Germany, IHP, involved characterization above 300 GHz for very fast photodiodes.

5.1 Zero-Bias Photovaractor with 60 GHz Resonant Network

The near-field radiation pattern of antennas contains data that are useful for antenna under test (AUT) diagnostics [78, 79, 80]. Indirect, monostatic measurement systems, infer an AUT's near-field pattern via signal scattering from a probe placed in the AUT's near-field, where an external source modulates the amplitude of the scattered signal [81]. Susceptibility to electromagnetic perturbation requires that the probe minimally influence the AUT's radiation pattern in order to attain high-precision measurements. Thus, the optically modulated scatterer (OMS) technique utilizes an optical external modulation source in conjunction with a photodetector as the probe's active device to modulate the signal via an optical fiber at zero-bias, eliminating the need for electrical bias lines [82]. Additionally, globally growing wireless communications demands of consumers for high data-rate information and entertainment has pushed communications operation towards the 60

GHz regime, due to an abundance of widely available spectrum [83]. It is therefore of interest and beneficial to develop antenna diagnostic tools, such as the OMS probe, operating around 60 GHz.

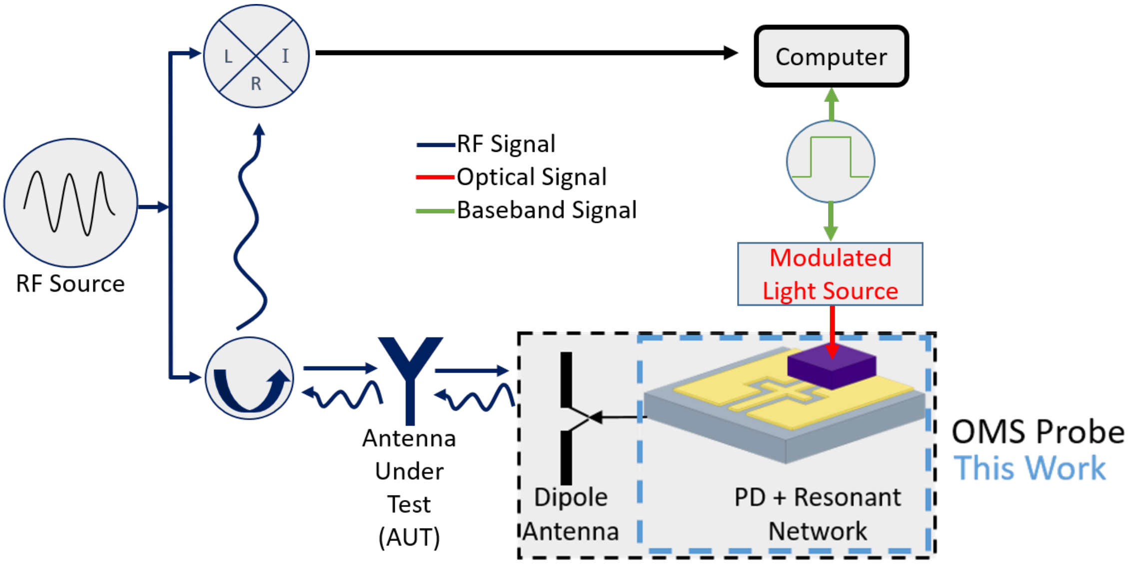

Figure 5.1: Overview block diagram of monostatic configuration of optically-modulated near field measurement probe and highlighted focus of this work.[84]

Highlighted in Figure 5.1, we demonstrate an optically modulated device to be used as an OMS probe operating around 60 GHz. As the active device, we use a photovaractor [85] that is flip-chip-bonded to a coplanar-waveguide (CPW) resonant matching network. An optical fiber input modulates the varactor and at low-photocurrent, the varactor fed CPW network resonates around 60 GHz. As the photocurrent increases, the resonance dip in the scattering parameter S11 changes by more than 50 dB, ∼15 dB greater than the device reported in [86] operating at 2.5 GHz.

5.1.1 Photovaractor Design and Characterization

The structure of the photovaractor is shown in Figure 5.2. The epitaxial-layers were grown on semi-insulating InP substrate by metal organic chemical vapor deposition. The first layer is a 50 nm InP buffer layer. This is followed by 400 nm lightly n-doped (5×1016 cm^{-3}) and 100 nm unintentionally doped (5×1015 cm^{-3}) InGaAs absorber. Finally, the top layer is a 200 nm heavily p-doped (1×1018 cm^{-3}) InP contact layer. The photovaractors are fabricated using the same process as that in [87]. Ti/Pt/Au/Ti and AuGe/Ni/Au metal stacks are deposited as p and n contacts, respectively. SiO_2 grown by plasma-enhanced chemical vapor deposition is used as a hard mask for the p and n mesa etch. Both the III-V material and SiO_2 are etched by an inductively coupled plasma system. The 2-µm thick contact pads are formed by gold electro-plating and the backside of the wafer is polished to reduce reflection. Finally, the wafer is diced into 1 mm × 3 mm chips.

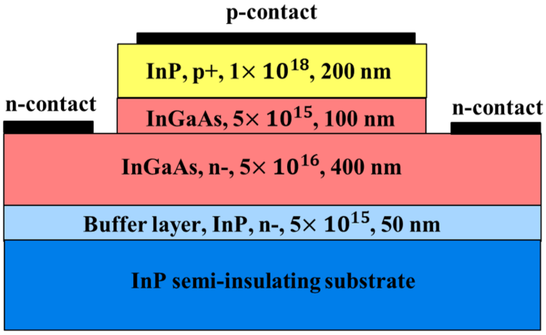

Figure 5.2: Epitaxial structure of photovaractor.[85]

The operation of the photovaractor is illustrated in Figure 5.3. At high frequencies, the capacitance of the p-n junction is dominated by the depletion capacitance, which can be expressed as:

$$C = \frac{\varepsilon_s A}{W_D} \tag{5.1}$$

where ε_s is the permittivity of the semiconductor, A is the effective area and W_D is the width of the depletion region. In Figure 5.3a, the dashed arrows denote the electric field lines. In the dark case, since the InGaAs absorber is thin and lightly doped, it is depleted to the semi-insulating substrate. Considering the capacitance between the p and n contacts, the effective area is the lateral area of the depletion region. When illuminated as shown in Figure 5.3b, the depletion region shrinks and a low-resistance channel is generated between the depletion region and the substrate due to the accumulation of photo-generated carriers. In this case, the effective area becomes the sum of lateral area and the bottom area. Although the lateral area decreases somewhat, the additional bottom area dominates because it is much larger than the lateral area. In addition to the increase of effective area, A, the depletion width, W_D, also decreases. The combination of these two effects enables a large change in capacitance with illumination. Figure 5.3c shows the corresponding band structure in the dark case and Figure 5.3d illustrates the band structure under illumination. There is a barrier in the valence band at the InP/InGaAs heterointerface. This barrier is very important to the operation of the photovaractor. In the case of illumination, the photo-generated holes accumulate at the interface. The accumulation of positive charge creates an increased potential in this region, which results in

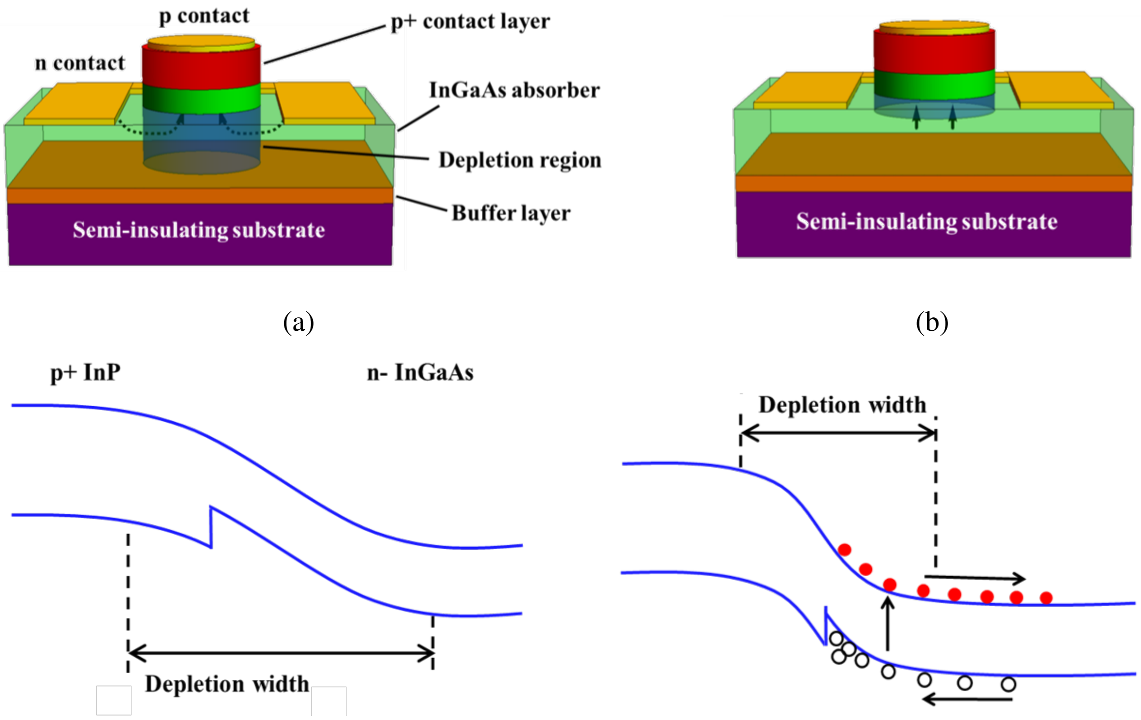

(a) (b)

(c) (d)

Figure 5.3: Depletion region of photovaractor in the dark case (a) and depletion region under illumination (b); band structure of photovaractor in the dark case (c) and band structure under illumination (d).[85]

a decrease in the depletion width, as shown in Figure 5.3d. Also, the slope in the depletion region becomes steeper.

The electric field distribution without bias was simulated with Crosslight software and is shown in Figure 5.4. The horizontal axis is the distance from the top of p+ InP layer. The dashed curve depicts the electric field in the dark case, while the solid one is that after illumination. The inset is an expanded view of the two curves. In the dark case, the electric field extends across the whole InGaAs absorber and the buffer layer, which means they are fully depleted. After illumination, the electric field drops to zero in most of the InGaAs absorber, an indication of decreased depletion width. Since the built-in potential remains relatively constant, the peak electric field intensity increases after illumination.

Figure 5.5a shows measured current-voltage curves for devices having diameters of 28-µm, 34-µm, 40-µm, and 50-µm. The forward current increases to the compliance value (1 mA) at 1.7

V, which indicates a relatively large series resistance resulting from the lightly-doped n-type region. At -5 V, the dark current of all the devices is approximately 1 μA. Figure 5.5b shows that the dark current exhibits a linear relationship with the square of the device diameter, an indication that bulk leakage dominates. The capacitance-voltage curves were measured with an LCR meter (HP4257A). It should be noted that this is the capacitance in the low-frequency range (100 KHz). At high frequency, such as the 60 GHz operating frequency of interest, the capacitance decreases owing to the frequency dependence of the junction capacitance. As shown in Figure 5.5c, the measured C-V curves can be divided into three regions. Near 0 V, the capacitance decreases rapidly with increasing reverse bias. As mentioned above, the influence of the AC voltage (∼0.2Vpp) of the LCR meter needs to be considered. Due to the low-frequency AC signal, the varactor operates alternately in reverse and forward bias, and the diffusion capacitance is comparable to, or even larger than, the depletion capacitance. From -0.5 V to ∼-2V, the capacitance decreases with bias voltage, because the depletion region under the n contact is increasing. When the reverse bias voltage is higher than -2 V, the capacitance is relatively constant. The capacitance at -5 V versus device diameter is shown in Figure 5.5d. In the dark case at -5 V,the depletion capacitance is dominate and the effective area is the lateral area, which has a linear relationship with the diameter.

Since the LCR meter can only test the capacitance at low frequencies, the impedance at high frequencies was determined by measuring the S11 parameters using a vector network analyzer. The experimental setup is shown in Figure 5.6. Light from a CW laser at 1550 nm is first amplified

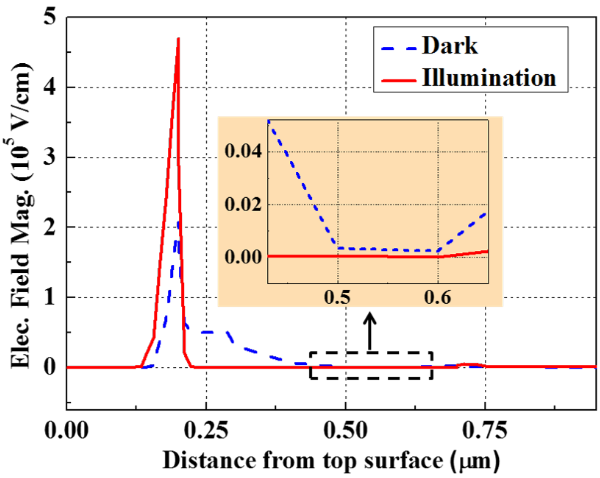

Figure 5.4: Vertical cut of simulated electric field distribution in photovaractor.[85]

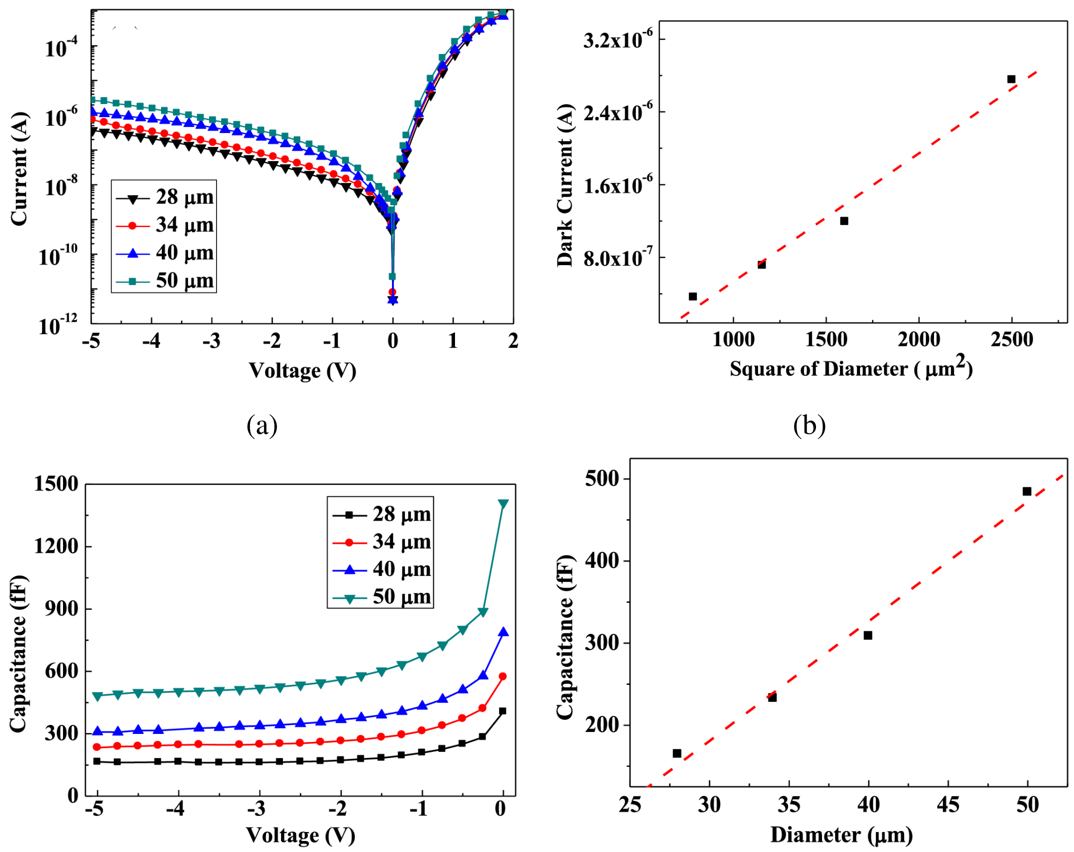

(a) (b)

(c) (d)

Figure 5.5: Measured IV of photovaractors with active area diameters of 28-µm, 34-µm, 40-µm, and 50-µm (a); dark current at -5 V bias vs. square of diameter of active area (b); measured capacitance-voltage curves for devices with diameters of 28-µm, 34-µm, 40-µm, and 50-µm diameter active areas (c); and capacitance at -5 V bias vs. active area diameter (d).[85]

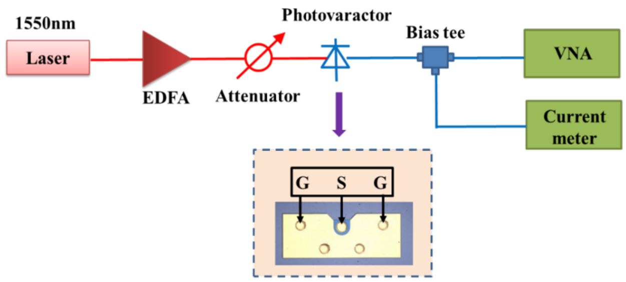

Figure 5.6: Block diagram for photovaractor S11 measurement setup.[85]

by an erbium-doped fiber amplifier, and then coupled into the photovaractor through a collimated fiber. An optical attenuator is inserted after the EDFA to adjust the incident signal level. To avoid the influence of the coplanar waveguide (CPW), the device is tested directly using a ground-signal-ground RF probe with pitch size of 150 µm. A current meter is used to measure the photocurrent through a bias tee. Finally, the S11 curve is measured by the vector network analyzer.

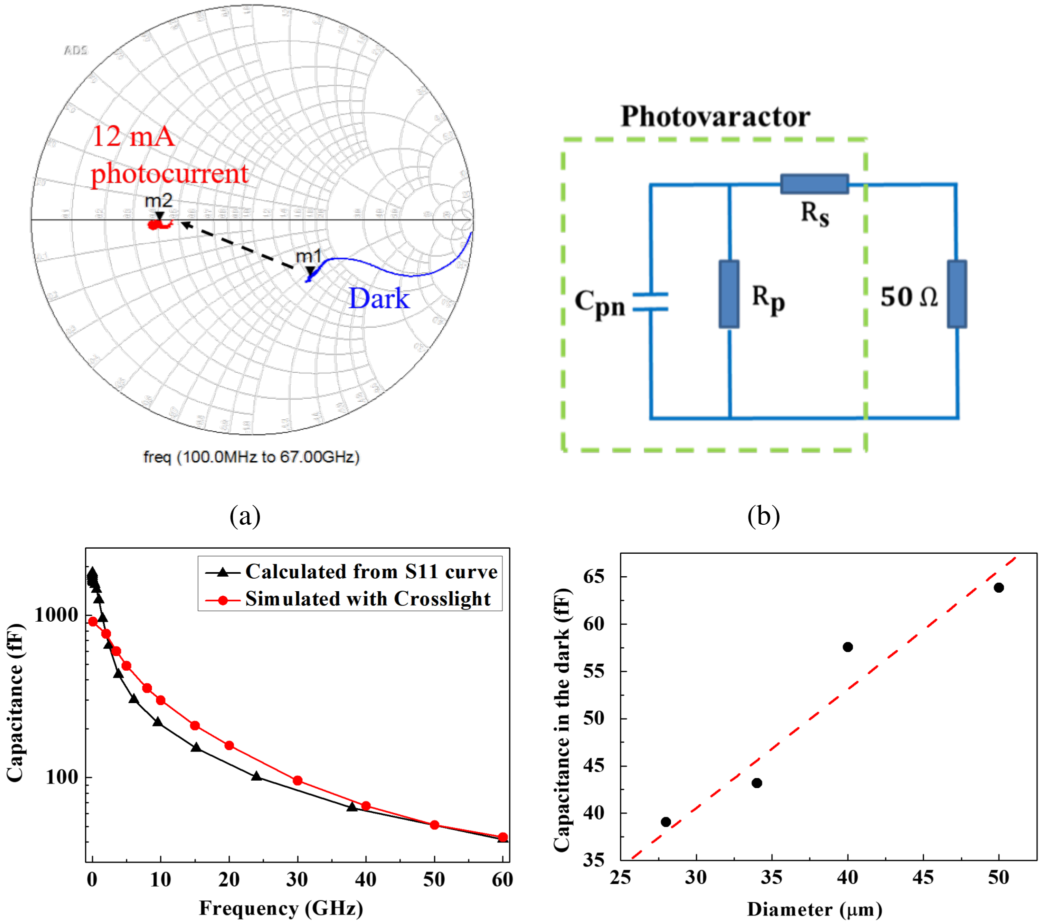

(a) (b)

(c) (d)

Figure 5.7: Measured S11 of 50-µm photovaractor in the dark case (blue, m1) and illuminated at $I_{PD} = 12mA$ (red, m2) (a); equivalent circuit model of the photovaractor (b); capacitance in the dark case for: a 50-µm diameter device vs. frequency (c); and capacitance at 60 GHz vs. device active area diameter (d).[85]

Figure 5.7a shows the measured S11 curves of a 50-µm diameter device in the frequency range 100 MHz - 67 GHz. As labeled, one curve is the S11 in the dark case, while the other is that with a photocurrent of 12 mA. Two markers in the figure show the impedance at 60 GHz: m1, the dark case, is $70.6 - j42.4\Omega$ while m2, the illuminated case, is $20.4 - j0.15\Omega$. After illumination, the resistance changes from 70.6 Ω to 20.4 Ω, which is a result of the photoconductive effect of the lightly-doped InGaAs absorber. The reactance at 60 GHz changes by ∼280x, which is caused by both the large capacitance and parallel resistance changes. To analyze the impedance changes, an equivalent circuit, shown in Figure 5.7b, was used to fit the S11 measurements. $\mathrm{C_{pn}}$, $\mathrm{R_p}$ and $\mathrm{R_s}$ are the junction capacitance, parallel resistance and series resistance, respectively. In the dark case, the parallel resistance is very large (∼MΩ) and can be taken as "open." Then the equivalent circuit becomes a simple cascaded RC circuit and the series resistance and junction capacitance can be calculated directly from the input impedance. However, in the case of illumination, the parallel resistance drops to less than 100 Ω and cannot be ignored. Curve-fitting of the measured amplitude and phase of S11 is needed to estimate the three parameters of the equivalent circuit.

At zero bias, the measured capacitance has two contributions: the depletion capacitance and diffusion capacitance, which are based on the transport of majority and minority carriers, respectively. As the frequency increases, both of these two types of capacitance decrease because the carrier transport cannot follow the rapidly-changing electric field. But the diffusion capacitance will relax first because the diffusion of minority carriers is much slower than the dielectric relaxation process of majority carriers. As estimated, the diffusion capacitance began to decrease at frequency above 1–10 MHz, while for depletion capacitance, that value is ∼10 GHz. In Figure 5.7c, the ▲ symbols are the calculated capacitance versus frequency in the dark case. For comparison, the value simulated with Crosslight is also shown by the • symbols. There is good agreement between these two curves. The overall capacitance decreases from ∼2000 fF to 40 fF when the frequency increases from 100 MHz to 60 GHz. Figure 5.7d shows the capacitance at 60 GHz for devices of different diameters. Similar to the trend in Figure 5.5d, the capacitance increases linearly with diameter. However, the absolute value is much smaller at 60 GHz. At such high frequency, the contribution of diffusion capacitance is very small and can be ignored. But the depletion capacitance, which is dominant, also suffers a large decrease due to its frequency-dependence.

As mentioned above, S11 curve-fitting is needed to estimate the capacitance in the case of illumination. In the fitting process, the frequency range needs to be chosen appropriately as a result of the frequency dependence of the capacitance. In Figure 5.7c, it can be seen that the capacitance does not change very much when the frequency is higher than 40 GHz. Therefore, we chose the S11 curves in the range of 40 GHz - 67 GHz to do fitting and estimate the capacitance at 60 GHz under illumination. Figure 5.8a shows the capacitance versus photocurrent. Since the

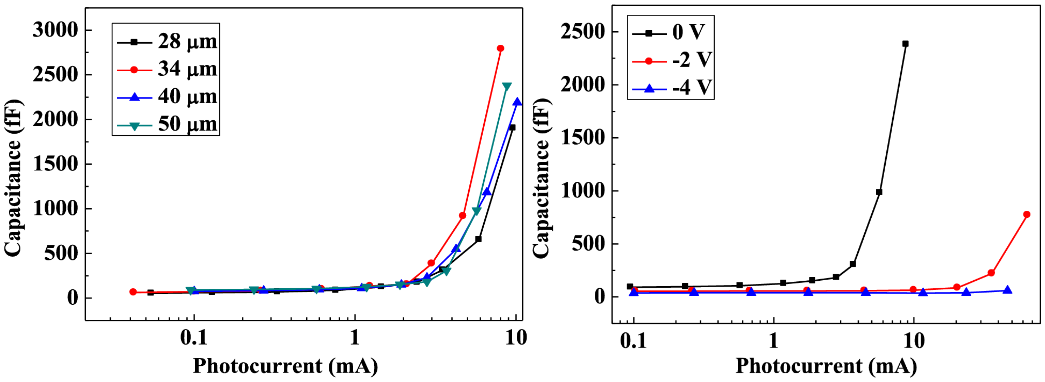

(a) (b)

Figure 5.8: Capacitance of devices with different diameters vs. photocurrent, measured at 60 GHz and 0 V bias (a), and capacitance vs. photocurrent for a 50-µm photovaractor at 60 GHz and various bias voltages (b).[85]

capacitance change relies on the accumulation of the photogenerated carriers, it increases slowly when the photocurrent is lower than 2 mA. The capacitance increase becomes significant when the photocurrent is higher than 3 mA. Compared with that in the dark case, the capacitance of the 50-µm diameter device increases from 63.8 fF to 2381 fF at photocurrent of 8.8 mA. The capacitance is increased by nearly 37 times. For the 28 µm-diameter device, the increase is 49x at photocurrent of 9.6 mA. Figure 5.8b shows the fitted capacitance versus photocurrent at different reverse bias voltages. As expected, the capacitance change becomes smaller when the reverse bias increases. At -4 V, the capacitance after illumination never exceeds 61 fF. The reverse bias aids hole transport at the InP/InGaAs heterointerface. Since the capacitance change is based on the accumulation of photo-generated carriers, the reverse bias will prevent the accumulation and minimize the capacitance change. Therefore, at high reverse bias voltage, the capacitance change is not as large as that at 0 V.

5.1.2 Resonant Network Design and Characterization

To enhance the change of impedance at low photocurrents and at 60 GHz, I designed a CPW resonant network in ADS. The design of the resonant network utilized an open-circuited stub resonator. The stub lengths were initially designed to be approximately a quarter wavelength at 60 GHz. The stubs were then implemented in ADS as CPW TLines-Waveguide, where the dielectric of the substrate (AlN at $\varepsilon_r = 9.6$), width, length, and gap to ground dimensions could be connected to the circuit model of the photovaractor, and tuned to create a complex conjugate match at 60 GHz

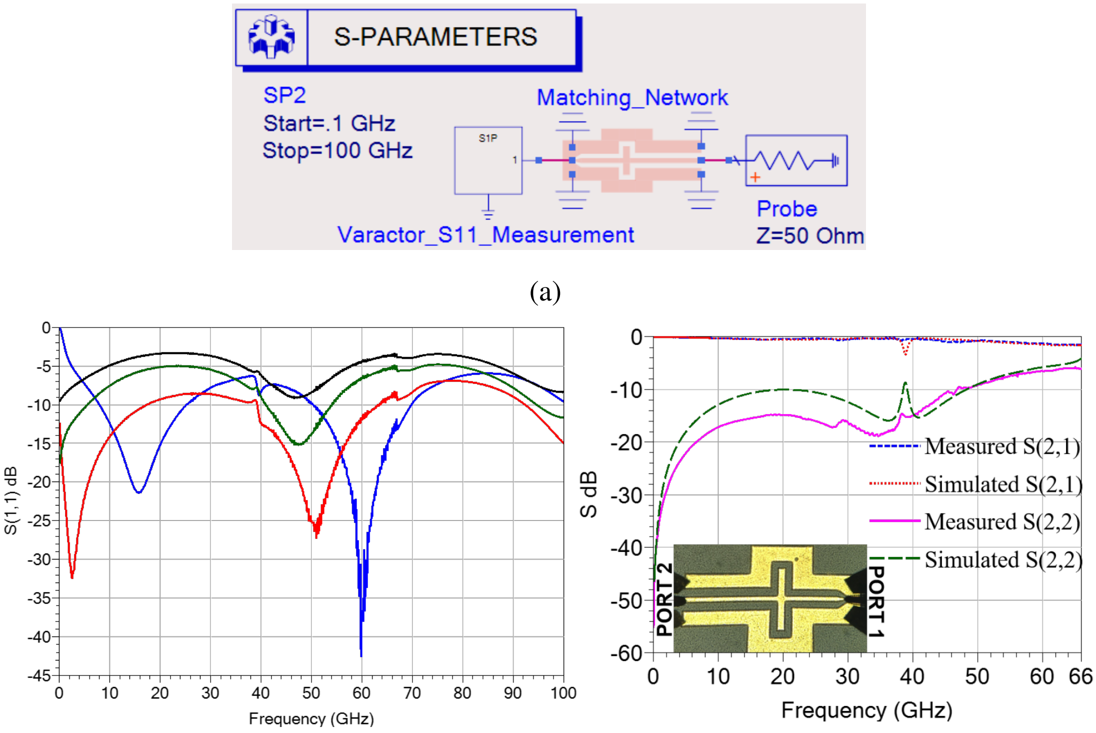

(a)

(b)

(c)

Figure 5.9: Circuit model implementing measured S11 data for the photovaractor with the open-stub, 60 GHz resonant network (a), simulated results of the model in the dark case, and at 3, 7, and 10 mA illumination (b), and measured vs. simulated 2-port data for matching network.

for 28-µm, 34-µm and 40-µm diameter photovaractors at low photocurrent. After the dimensions were determined through tuning of the circuit model, the open-stub resonant network was drawn and simulated from DC to 100 GHz in ADS as a GSG transmission line with 2-µm thick gold traces on a 380-µm thick AlN substrate. The input side of the CPW was designed to be compatible with the p and n metal of the photovaractor to enable flip-chip bonding of the varactor, and the output side was designed to be compatible with the 150-µm pitch probe. I then imported and implemented the data from the S-parameter measurement of the photovaractors as a file driven one-port element, as shown in the circuit model in Figure 5.9a. The results of the model in the dark case, and under illumination equating to 3, 7, and 10 mA photocurrent, are shown in Figure 5.9b. In the dark case, a good match at 60 GHz is achieved with a notch depth of ∼40 dB with a full-width-half-max (FWHM) of ∼4 GHz. At 3 mA the resonance shifts to 50 GHz and there is a 30 dB change at 60 GHz, improving to 35 dB at 10 mA. It should be noted that S11 measurements of the varactor were only taken up to 67 GHz, so the simulated data above 67 GHz in Figure 5.9b assumes 50-Ω looking into the data file port. The final step was to design a mask for the resonant-stub circuit and fabricate the circuit.

The circuit was fabricated by depositing a 120 nm seed layer of Ti/Au on a 380-µm AlN substrate. Hard contact lithography was performed next using 8-µm thick photoresist. The metal pads of the CPW network were then Au plated to a thickness of ∼2-µm. The photoresist was then lifted off with the excess Au, and a Au wet etch was done to remove the Au seed-layer. Finally, the sample was diced into individual arrays of the circuit, for flip-chip bonding with the photovaractor die. After fabrication and before flip-chip bonding, two-port measurements were done on the unloaded resonant network and compared to simulated results, which showed good agreement, as seen in Figure 5.9c. The inset of Figure 5.9c shows a microscope image of the resonant network being probed for the 2-port VNA measurement. The photovaractor die was then flip-chip bonded to the open-stub resonant network through Au-Au thermal compression bonding, connecting the p-mesa and n-mesa of the varactor to the signal and ground lines of the CPW matching network, respectively. A microscope image of the flip-chip bonded device can be seen in Figure 5.10.

5.1.3 Results

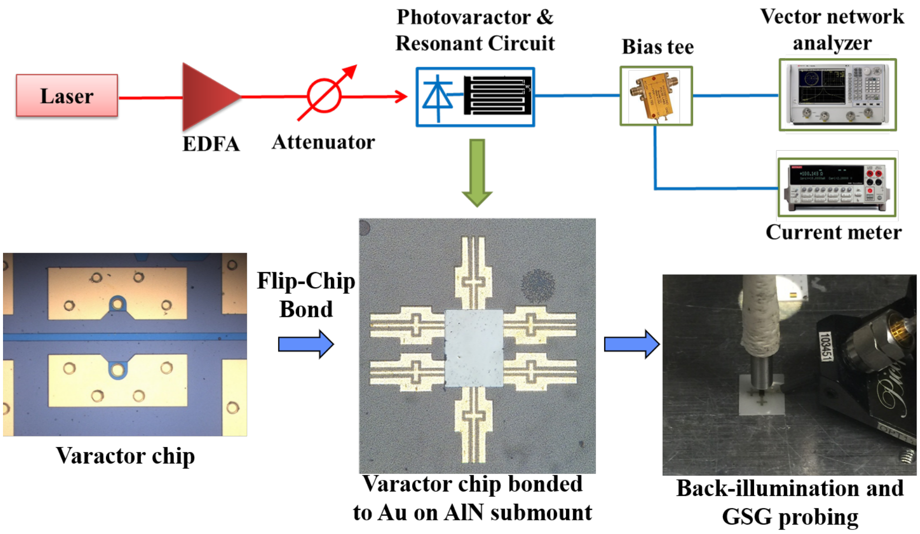

Figure 5.10: Measurement setup for photovaractor and 60 GHz resonant network.[84]

The measurement setup used to characterize the photovaractor with resonant network is shown in Figure 5.10. Light from a 1550 nm laser source was amplified in an EDFA and coupled into the photovaractor using an 8-μm spot-size collimated fiber. We used a high frequency RF probe followed by an external bias-tee to extract the signal from the output of the CPW. Photocurrent was monitored with a source meter and S11 was measured with a vector network analyzer. The probe was calibrated with a GGB Au calibration substrate (CS-5).

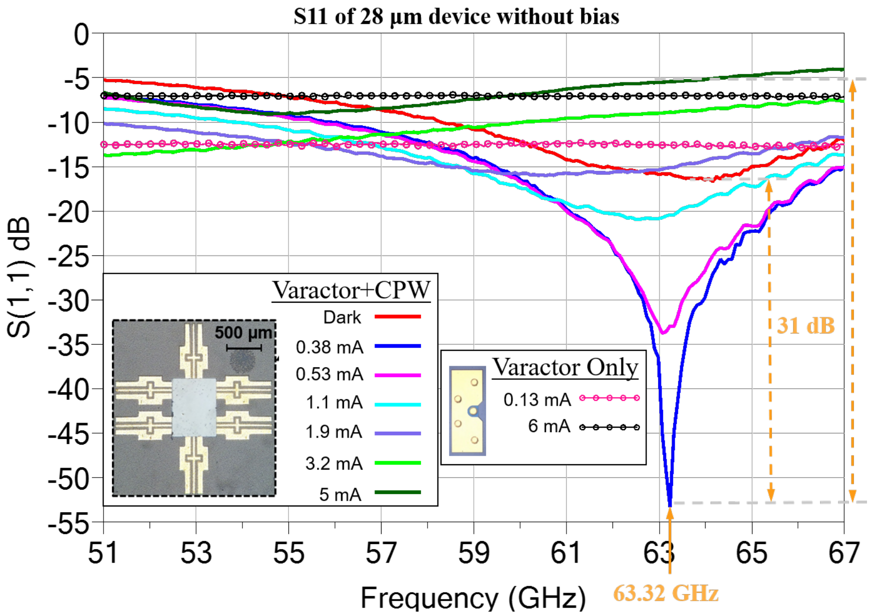

Figure 5.11: Measurement results for a 28-μm photovaractor under varying photocurrents before and after flip-chip bonding to resonant matching network.

Figure 5.11 shows a comparison of scattering parameters at low and high photocurrent before and after flip-chip-bonding a 28-μm photovaractor. With matching network at 0.38 mA photocurrent, the device achieves a notch depth of 53 dB, with a FWHM of ~3 GHz, and the change in scattering at 5 mA photocurrent was 52 dB. Compared to the varactor without CPW, the resonant network from low photocurrent to high photocurrent increases the change in scattering by almost 9x. Figure 5.12 shows the equivalent change in scattering parameter to impedance for both cases. Looking into the resonant network, this change in scattering equates to a change in real impedance by 3x from 50 Ω to 154 Ω, and 200x change in imaginary impedance from 0.2 Ω to 40 Ω. For the varactor alone, the change in real impedance is 2.5x and in imaginary impedance is 12x. Figure 5.13 shows the S11 measurement results for a 34-μm and 40-μm varactor with matching network. The 34-μm device resonates at 64.3 GHz, with a notch depth of -61 dB at 220 μA, changing to -12 dB at 2 mA photocurrent, which corresponds to an impedance change from $49.9 + j0.01\Omega$ to

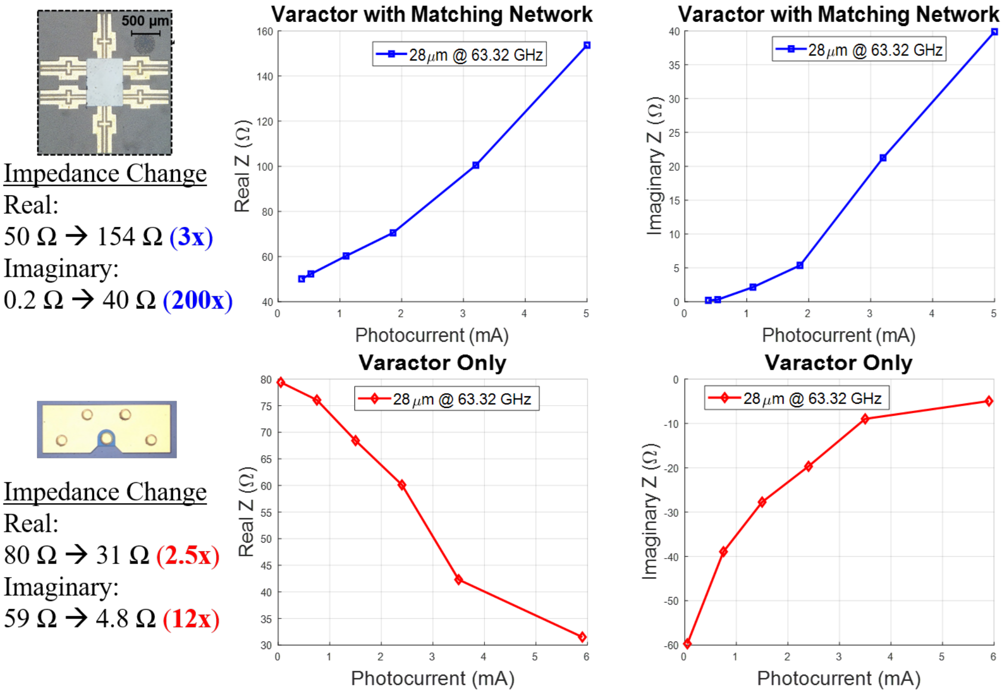

Figure 5.12: Analysis of real and imaginary impedance change for a 28-µm photovaractor at 63.32 GHz under varying photocurrents before and after flip-chip bonding to resonant matching network.

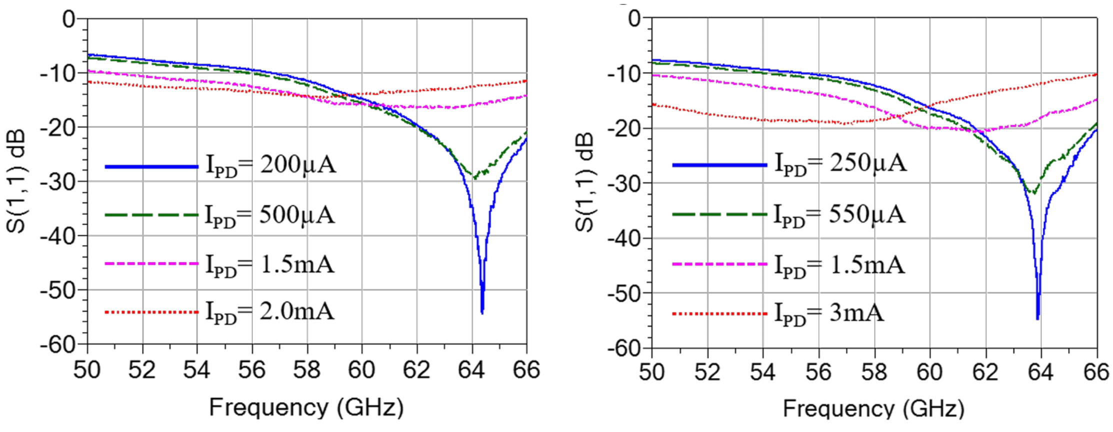

(a) (b)

Figure 5.13: S11 measurement results for photovaractor and CPW resonant network at varying photocurrents for a 34-µm device (a), and a 40-µm micron device (b) measured at 0 V bias.[84]

$79.8 + j10.7\Omega$. For photocurrents of 250 µA and 3 mA, the change in scattering with resonant network increased by 35 dB for the 40-µm diameter photovaractor at 63.8 GHz. Looking into the resonant network, the real part of the impedance changed from 50 Ω to 78 Ω and the imaginary part from 0 Ω to 15 Ω. It is important to note that the circuit was designed in ADS to resonate at 60 GHz; however, measurements were consistent at a resonance of 64 GHz for multiple devices. This shift occurs because of parasitics introduced from flip-chip bonding. By increasing the length of the stubs, we expect to shift the resonance back down to 60 GHz. These results represent an important step towards a first published zero-bias OMS probe operating at 60 GHz.

5.2 Ultra-Fast Germanium Photodiodes

In another project, we were given the opportunity to really flex our measurement capability, and help with characterizing the fastest germanium (Ge) based photodiodes ever developed. When I joined the group in 2016, our frequency measurement capability was limited to 110 GHz. During the packaged photodiode project, my predecessor bumped this capability up to 170 GHz. During the emitter experiment, I took the capability up to 220 GHz. Then finally, in 2021, we had a batch of devices that pushed us all the way through the mmWave frequency band, to 325 GHz (350 GHz uncalibrated). In order to continue pushing this measurement capability, special attention needs to be paid to the RF probes, especially concerning pitch size, probe tip size, and compatibility with power meters. More about the measurement setup can be found in Chapter 8. In collaboration with a partner in Germany, IHP, we measured 3-dB bandwidth in Ge waveguide-coupled PDs at more than 260 GHz, besting the previously reported record by more than 100 GHz. Furthermore, comparing our results from DC-110 GHz with ihp's LCA measurements, gave us a surer foot of our precision. Figure 5.14 shows the measurement results for three of the Ge PDs measured in our lab. The devices, measured at -2 V bias and 1 mA photocurrent, achieved 3-dB bandwidths of 265, 245, and 221 GHz, with the bandwidth result scaling with PD active area. [88]

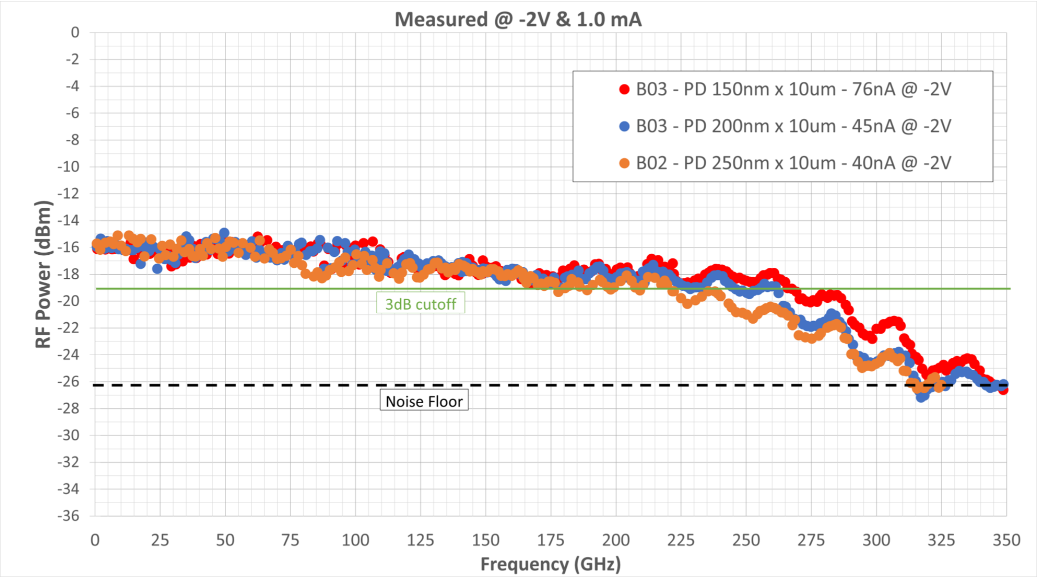

Figure 5.14: Measurement results for fast Ge photodiode devices.

Chapter 6

Design of the Next Generation of High Speed Photodiodes

Applying lessons learned from both the surface normal and waveguide FUTC photodiodes, I have designed the next generation of photodiodes for our the Optoelectronic Device Group at UVA to achieve broadband, DC-300 GHz performance, covering the mmWave spectrum. The following chapter covers the design behind these photodiodes.

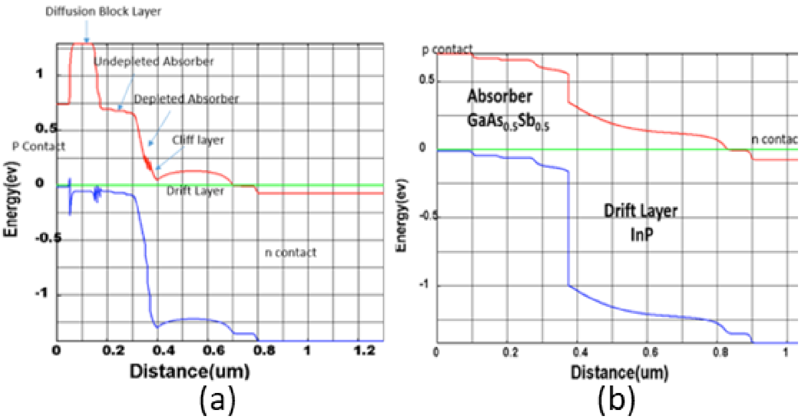

Figure 6.1: Band diagram illustrating the absorber/drift layer heterointerface of Type-I InGaAs/InP (a) and Type-II GaAsSb/InP (b) band alignments under zero-bias.

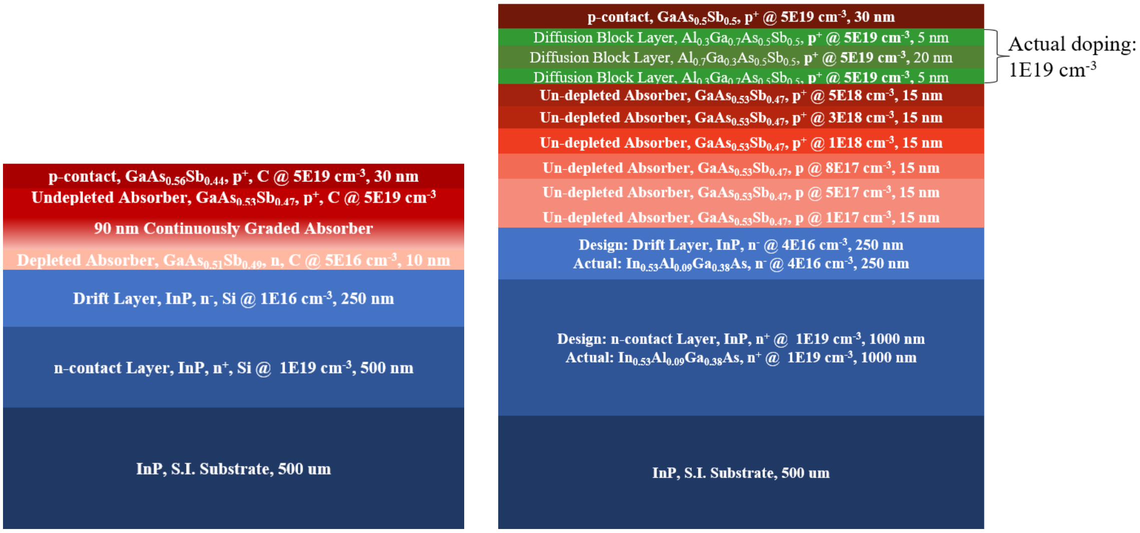

(a) (b)

Figure 6.2: Hong Kong epitaxial structure (a) and NIST epitaxial structure (b).

6.1 Epitaxial Design

The epi design for FUTC shown in Figure 2.2 has a relatively complex stack-up, largely due to the discontinuity in the conduction band at the InGaAs/InP absorber/drift layer heterointerface. In order to smooth this discontinuity and promote electron transit, as illustrated in Figure 1.4 quaternary InGaAsP smoothing layers are grown. By replacing the InGaAs absorber (type-I band alignment) with a GaAsSb absorber (type-II band alignment), this discontinuity is removed at the interface to the InP, as illustrated in Figure 6.1. In addition to reduced complexity in the epi design and consequently growth of the material, removing this band continuity should also help facilitate high speed operation at lower DC power consumption, with less demand for bias voltage. The final epitaxial layer stack-ups I designed are shown in Figure 6.2.

The first 'Hong Kong' (HK) stack-up in Figure 6.2a, I designed for growth by our academic collaborator, Professor Kei May Lau, at Hong Kong University of Science and Technology (HKUST). The full details of the growth can be found in Appendix B. To my knowledge this is the first PD absorber to utilize a continuous grading in the absorber. The second stack-up which I designed for a project with NIST, Figure 6.2b, was grown by a commercial vendor, Intelli-Epi, and utilizes the traditional step-graded absorber used in FUTC. Note that in Figure 6.2b, the designed epi differs from the actual epi grown, as noted. There is a constraint often faced with commercial crystal growers, in finding phosphide-containing compounds available for growth in the same chamber as other materials; in this instance, GaAsSb, and so we had to replace InP with a quaternary layer of InAlGaAs. This puts the HK epi at a unique position as our academic collaborator could grow the designed epi. As mentioned in chapters 1.3, the gradient of doping in the absorber is used to generate an internal field to help accelerate charge carriers through the absorber, in for electrons into the drift layer for collection. By removing abruptness in grading density with a continuous absorber, we may achieve a smoother electric field profile which could lead to a more efficient electron transport occurring at maximal drift velocity, ideally faster than that of the FUTC velocity. Furthermore, because of the continuous grading, I believe we can enable improved performance with a larger variance in p doping going from the p-contact through the absorber and to the drift layer. As seen in Figure 6.2a, the p-doping in the top of the absorber is an order of magnitude higher than in the FUTC stack-up Figure 2.2, and the p-contact doping is consequently higher as well which should reduce series resistance in the device, which, as mentioned with Equation 1.3, becomes an important factor when designing small devices. If the absorber field can retain its strength for longer as more carriers are generated from higher illumination power, then the photogenerated carrier effects on the applied field can be delayed allowing the applied field to retain strength in the drift layer under higher optical power, and thus reach a higher RF power output performance metric.

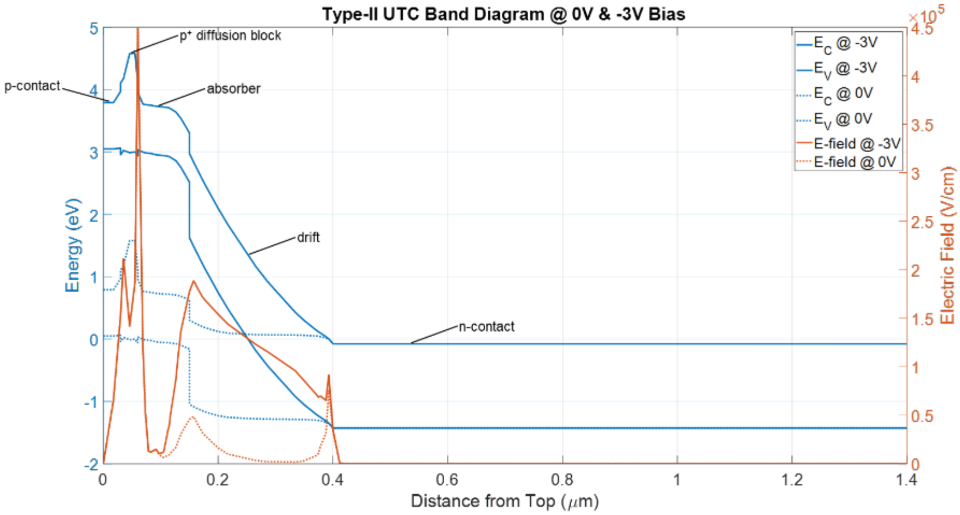

Figure 6.3: Band diagram and electric field profile of originally designed (GaAsSb/InP) NIST epi at 0 V and -3 V bias with no illumination.

Another difference between the HK and FUTC/NIST epis is the lack of blocking layer.

With no electron blocking layer it may be possible to achieve a more uniform field at the p-contact, albeit at the same time risking back flow of electrons into the p-contact; however, efficient electron transport towards the drift layer will ideally be maintained from the field generated by the continuous doping grading. Calculations done on a GaAsSb/InP epi with no blocking layer from a previous student seem to point towards this back-flow not negatively impacting efficiency of the generated carrier transit, though, further investigation is warranted. Therefore, for the NIST epi in Figure 6.2b, in hopes to gain further insight into the trade-off of the diffusion blocking layer, a blocking layer was included. The simulated band diagram and electric field is shown in Figure 6.3 for the originally designed epi with a GaAsSb/InP heterointerface. After simulating the stack-up in ANSYS Lumerical, the doping of the blocking layer was compared at different doping densities, and was ultimately designed to be high doping in order to generate a thinner barrier to holes in the valence band shown in Figure 6.4. It should be noted that the maximum doping the grower could provide in the diffusion blocking layer was 1E19 cm^{-3} as opposed to the 5E19 cm^{-3} illustrated in the original design structure in Figure 6.2b.

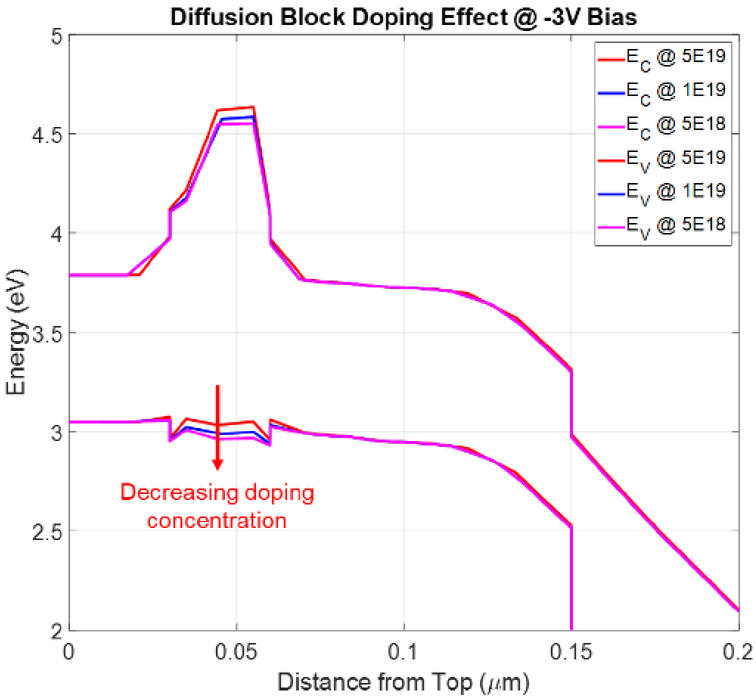

Figure 6.4: Effect of doping concentration on valence band barrier in NIST epi.

In designing the doping in the drift layer, there is a trade-off: with higher doping, you can

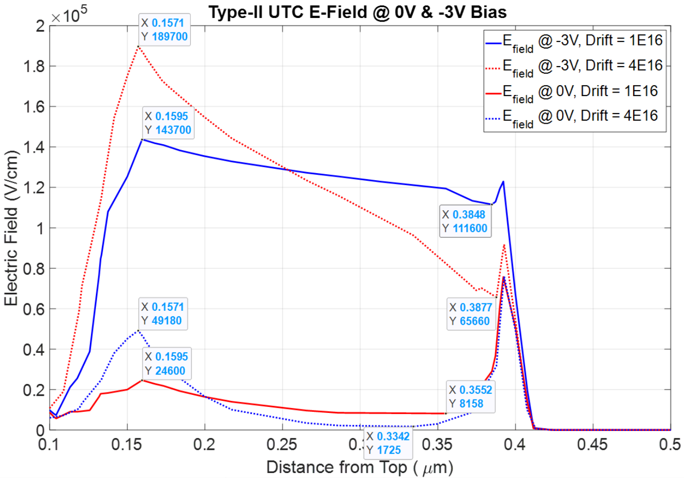

Doping (cm^{-3})	Bias	J_{sat} (mA/cm^2)	I_{PD} 4-μm Ø	I_{PD} 8-μm Ø
1E16	0 V	2.9E7	**3.6 mA**	**14.5 mA**
1E16	-3 V	5.6E7	**7.1 mA**	**28.3 mA**
4E16	0 V	8.3E7	**10.5 mA**	**41.9 mA**
4E16	-3 V	21.8E7	**27.4 mA**	**109.5 mA**

Figure 6.5: Electric field in an InP drift layer for different doping density and corresponding calculated saturation currents for a 4-μm and 8-μm PD.

achieve a larger electric field gradient under reverse bias, and thus higher saturation current, at the cost of needing a higher reverse bias to fully deplete the region. Higher bias, however, can also lead to more rapid thermal failure in the devices. A comparison of two doping densities is shown in Fig. 7-5, with corresponding saturation currents shown for a 4-μm and 8-μm device. Saturated current density was calculated using Ohm's Law:

$$J_{sat} = \sigma E, \tag{6.1}$$

where σ is conductivity, and E is the electric field in the collector. Considering the movement of only electrons drifting through the collector, the current density can be found by solving Poisson's equation in the collector and is written as [89]:

$$J_{sat} = \frac{2\nu_{sat}\varepsilon_{InP}}{d_{InP}^2}\left(V_{bi} + V_{PD} - E_{crit}d_{InP} + \frac{qd_{InP}^2}{2\varepsilon_{InP}}N_{DC}\right), \tag{6.2}$$

where ν_{sat} is the saturation velocity of electrons, ε_{InP} is the dielectric constant of InP, d_{InP} is the thickness of the drift layer, V_{bi} is the built-in voltage, V_{PD} is the voltage across the PD, E_{crit} is the electric field below which the electron velocity is not saturated, and N_{DC} is the doping in the collector. To examine the trade-off in doping density, the two epis have been doped to the two simulated densities as seen in Fig. 7-5. We see that while we simulate a 4X increase in saturation current at high bias (-3V, red dotted line) at 4E16 cm-3 doping, we effectively have zero field at lower bias (0V, blue dotted line). Whereas, a lower doping of 1E16 cm-3, maintains a field gradient at both high and low bias (blue solid line, red solid line).

6.2 Device Design

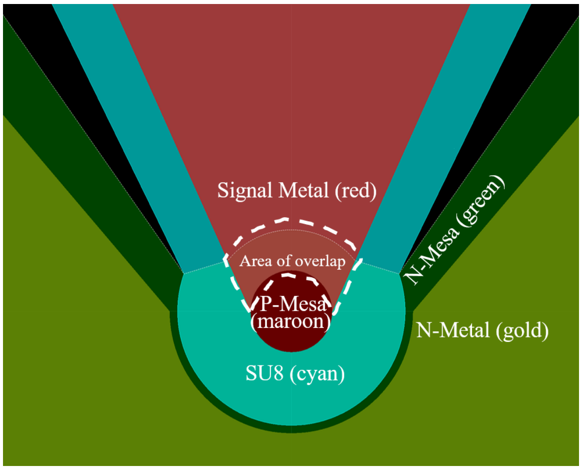

Figure 6.6: Illustration of device tolerance of p-mesa (maroon) to edge of n-mesa (green) area sitting under the signal metal.

When approaching device design, I wanted to look into the potential of reducing parasitics, by pushing towards smaller tolerances of the p-mesa to the edge of the n-mesa. Looking at Figure 6.6, by reducing the amount of area of the signal metal (red) sitting on top of the SU8 (cyan), in which the signal metal is overlapping (white dashed outline) the n-mesa (green), I am attempting to reduce parasitic capacitance created by this overlap, which ultimately contributes to the total equivalent junction capacitance, C_{pn}. If the overlapped area is proportional to the distance from the edge of the p-mesa to the edge of the n-mesa, at a >5-µm distance in the previous generation of devices, stray capacitance was extracted to be ∼7-fF (Figure 2.7). By cutting this distance in half to 2.5-µm, using an approximate area of overlap (white dashed line), ε_{SU8} of 4.2, and distance between signal metal and n-mesa (SU8 thickness) of 980 nm, and plugging these values in to Equation 1.2, this parasitic capacitance can theoretically be reduced to <1-fF. This reduction could prove critical when considering a 3-µm device C_{pn} of ∼2.5 fF.

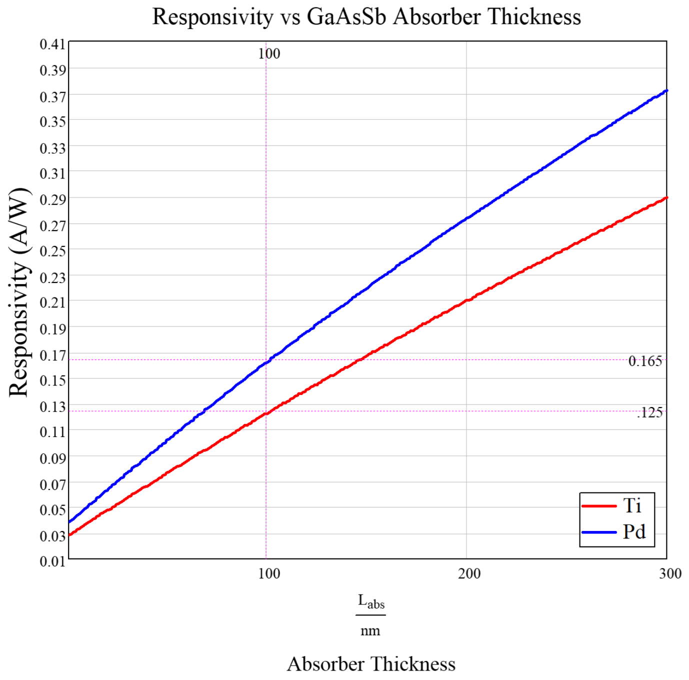

Figure 6.7: Effect of doping concentration on valence band barrier in NIST epi.

The absorber thickness was designed around the trade-off of reduced transit time limited bandwidth (Equation 1.5) and responsivity. A thinner absorber means shorter carrier transit time, but in turn means less material for light to be absorbed. I believe a way to combat this trade-off is by utilizing a higher reflectivity metal on top of the p-contact. After a literature review, I determined that Pd could be used as the first layer of our p-metal stack instead of our traditional Ti layer [90]. At 1550 nm, the reflectance of Pd is 86.1% as opposed to 65.9% in Ti; therefore, using Pd as the reflecting metal can provide more light for the second pass absorption. Shown in Figure 6.7, using a 100-nm thick absorber, Pd as the reflecting metal capping the p-contact epi layer, can increase responsivity by 24%, from 0.13 A/W to 0.17 A/W. The plot in Figure 6.7 shows responsivity as a function of absorber length, defined by:

$$R_{Gb} = R_{ideal} \cdot (1 - R_0) \cdot \left[\left(1 - e^{-\alpha_{Gb} L_{abs}}\right) + R_m \cdot e^{-\alpha_{Gb} L_{abs}} \cdot \left(1 - e^{-\alpha_{Gb} L_{abs}}\right) \right], \tag{6.3}$$

where, "*Gb*" is GaAsSb material, L_{abs} is the height of the absorber, R_{ideal} = 1.25 A/W, R_0 = 0.01 as the reflection at the surface of the PD, α_{Gb} = 6.8E3 cm^{-1} as the absorption coefficient, and R_m is the reflectance of the metal at 1550 nm. To eliminate unknowns of a new metal stack, Pd will not be used in the first round of fab for the devices, but offers a pathway to improved efficiency.

6.3 RF Design

The primary focus of the next generation of photodiodes is performance over the broad, mmWave range of frequencies, covering DC to 300 GHz and beyond. To achieve this, pitch-size, or distance from the center of the signal plane to edge of the ground plane becomes an important metric. Previously, we had worked towards a packaged application and up through W-band (110 GHz) coverage, and utilized a large, 250-µm pitch CPW transmission line, to accommodate both the RF probes we had working from DC-110 GHz, as well as to accommodate in-chassis epoxying to the glass bead of a coaxial connector. Now, as we move to a frequency range beyond current coaxial technology (>127 GHz), wavelengths become fractional to this pitch size leading to loss from higher order modes. This loss is highlighted by the probe companies who have maximum pitch widths they're willing to fabricate relative to the operating frequency of the probe. Therefore, the pitch width of the CPWs being designed for the next generation of high-speed PDs have a minimum pitch width of 90-µm for operation to 300 GHz. In order to accommodate the 150-µm probes already purchased for some of the frequency bands, the ground planes are extended far enough to accommodate a 150-µm pitch. As we push into the sub-THz regimen, we will need to decrease the pitch size further, and move away from the wide 150-µm pitch ground planes.

In the previous generation of devices, we flip-chip bonded the PDs with the understanding that using a thermally conductive submount could prevent failure due to thermal effects [9]. In order to accommodate the mechanical tolerances inherent to flip-chip bonding, large metal pads were used for the signal and ground planes, so as to provide enough metal beyond the PD die to be probed. Looking at the right side of Figure 2.4, it can be seen on the left and right side signal pads of the PD die, how the markings on the signal pad made by the RF probe, are encroaching on the PD die. As we begin to reduce pitch size and use less metal in CPWs, accommodating RF probing after flip-chip bonding will become more difficult to yield. Therefore, I believe by making this new generation planar, non-flip chip bonded devices, we can more confidently create small pitch-size, small metal footprint CPWs, that can be successfully probed. Additionally, since very little data exists above 100 GHz in our group, making this generation of PDs planar, will start our foray into the mmWave with reduced complexity in CPW and PD integration, and ideally help us gain insight into if we're thermally limited at these high operating frequencies.

To achieve true broadband performance, it has become necessary to move away from the inductive peaking submount that was used in the previous generation of devices Figure 2.13. While effective for the design frequency, inductive peaking is followed by increased roll-off of ca.

40 dB/decade beyond the 3dB bandwidth. Instead, we now want to achieve maximally flat roll-off, ideally, with closer to the ideal RC filter roll off of 20 dB/decade. Furthermore, as mentioned previously, it is of interest to begin reducing the total metal footprint used in our CPWs, as operating RF wavelengths become shorter. To achieve a maximally flat response, I have designed a tapered 50-Ω CPW, which can maintain $\sim$50-Ω impedance through the mmWave band to 300 GHz. To begin to investigate and characterize the effect of using a minimized metal footprint, I designed a CPW based on the broadband DC-220 GHz GSG pads in [91], using small RF pads just large enough to accommodate the RF probe tips. While losing the impedance driven performance of a 50-Ω matched CPW, these minimized metal pads could potentially emulate direct probing of the PD mesas. (It should be noted, in order to accommodate many of the RF probes available for measurement, this minimized metal design had to include 150-µm pitch compatibility, though, ideal design would have the GSG pads all the same dimensions at a fixed pitch.)

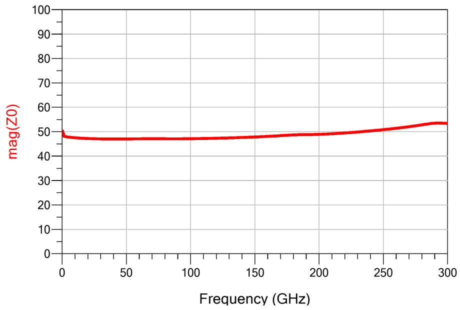

Figure 6.8: Simulated impedance of 50-Ω CPW from 0.1 to 300 GHz.

In ADS, I used the Controlled Impedance Line Designer tool as a starting point to make a simple rectangular pad 50-Ω CPW, focusing on a pitch size of 90-µm and a signal pad large enough to accommodate the probe tips of our RF probes. I then used those dimensions as a starting point to begin the design on the PD side of the CPW, sectioning the signal pad into smaller separate blocks by implementing the same design approach outlined in Section 5.1.2. I then designed the CPW in a Layout and ran a Method of Moments (MoM) frequency sweep from 0.5-300 GHz to generate the electromagnetic model for the CPW. I then calculated the characteristic impedance of the line using the two-port s-parameter sweep data. Figure 6.8 shows the result, with a $\sim$50-Ω match from low frequency to 300 GHz. Finally, for both the 50-Ω and minimal metal CPWs, I simulated their performance with the different sized PDs I planned to fabricate. Figure 6.9 summarizes and shows the circuit model, simulated bandwidth results, and design tolerances associated with each CPW. Figure 6.9a shows the PD circuit model as well as the implementation of the PD's transfer function in the current source. The junction capacitance was calculated using Equation 1.2. Figure 6.9b shows the results of the 50-Ω CPW, with a 14-µm PD achieving a 3-dB bandwidth of $\sim$50 GHz, and a 3-µm PD achieving a 3-dB bandwidth of 170 GHz. Figure 6.9c shows the results of the minimal metal CPW design.

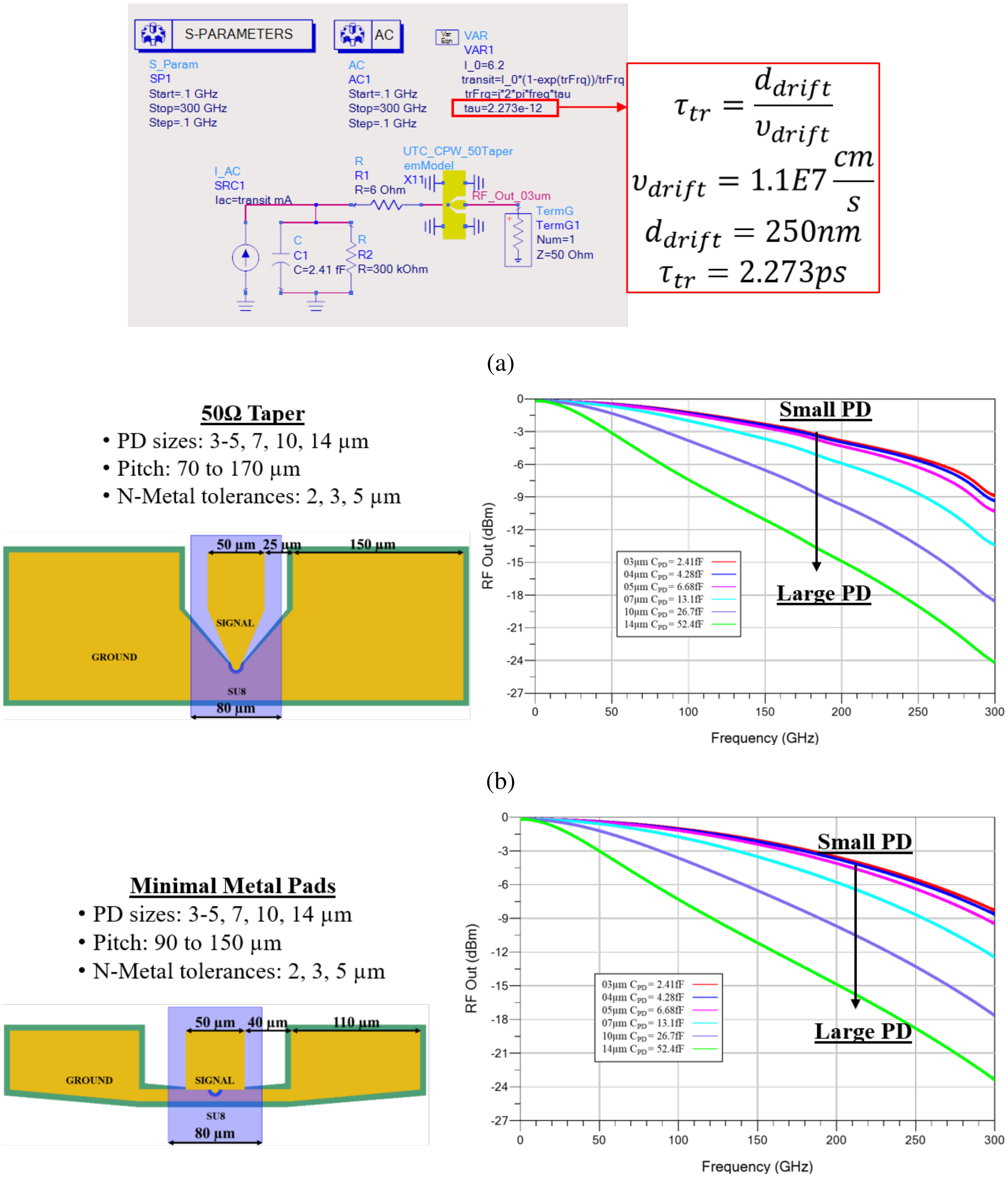

(a)

(b)

(c)

Figure 6.9: (a) PD and CPW circuit model showing transfer function dependent current source; designs with critical dimensions shown and projected bandwidth for the (b) 50-Ω CPW and (c) minimal metal pads CPW.

6.4 Fabrication Procedure

Taking a page from the waveguide FUTCs demonstrated in Chapter 3, as a way to reduce parasitics, improve device tolerances, and alleviate some of the constraints with available fabrication equipment (specifically contact lithography), I developed a new approach for fabrication of surface normal PDs as illustrated inFigure 6.10. This approach uses the insulating properties of SU8 to reduce the risk with the p-open step of fabrication and as discussed previously, push the devices to smaller dimensions in the p-mesa diameter and the p-mesa to n-mesa and n-metal tolerances. A challenge faced in the previous generation of surface normal PD fabrication and illustrated in Steps 7 and 8 of Figure 2.3, was the alignment tolerance of the p-open. If for instance you have a 4-μm diameter device, this alignment might be along the order of fitting a 2-μm feature from the photomask into the 4-μm circle. If this tolerance is not met, and, for instance, the smaller feature is off by as little as 2-μm, while it still might be within enough tolerance to achieve a contact to the p-metal, the misalignment can lead to Step 10 of Figure 2.3 shorting the p-mesa to the stack beneath. This ultimately reduces the feature sizes that can be reliably fabricated. As I hope to push speed of PDs, it is necessary to continue to shrink the sizes of the PD. This is what I hope to accomplish with the SU8 planarization shown in Steps 8 and 9 of Figure 6.10. SU8 also acts as a non-conductive bridge for the signal pad to sit on to insulate from the overlap with the n-mesa, thus eliminating the need for seed-layer and air-bridge lithographies and plating deposition and lift-off. Finally, SU8 also acts to passivate the sidewalls of the p-mesa.

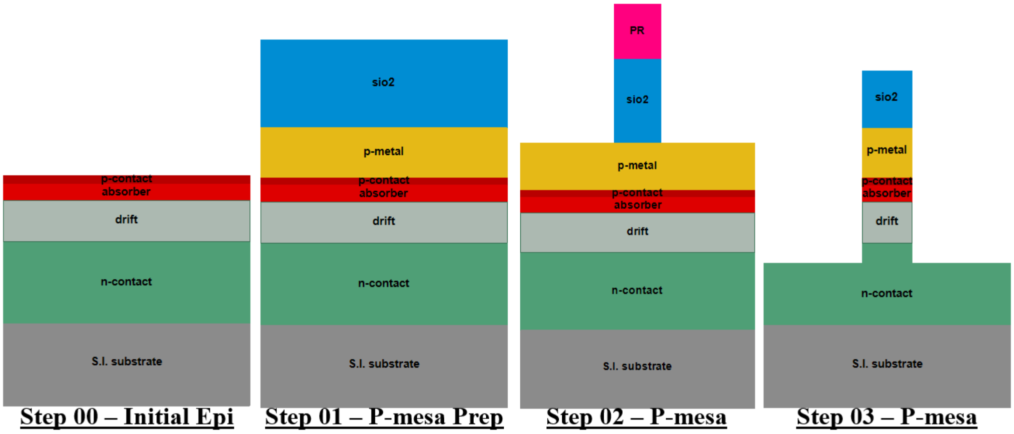

Step 00 – Initial Epi Stack **Step 01 – P-mesa Prep** **Step 02 – P-mesa Hard Mask Etch** **Step 03 – P-mesa Formation Dry Etch**

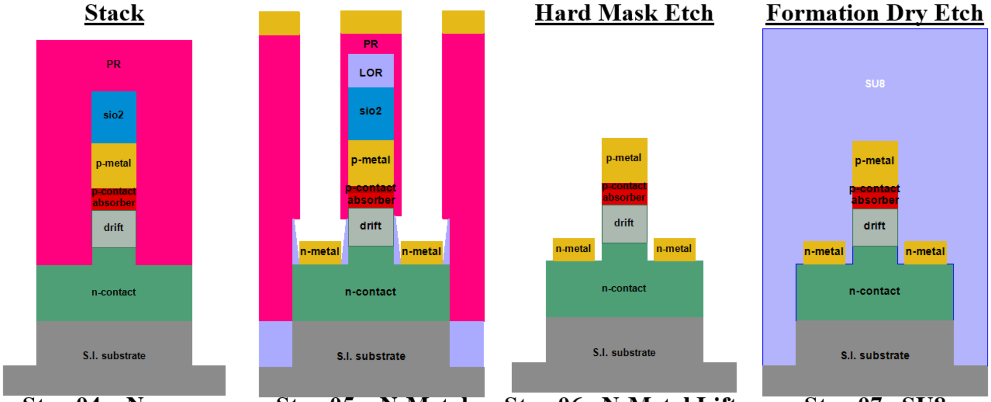

Step 04 – N-mesa Formation Dry Etch **Step 05 – N-Metal Deposition** **Step 06– N-Metal Lift-off & SiO_2 Wet Etch** **Step 07– SU8 Planarization**

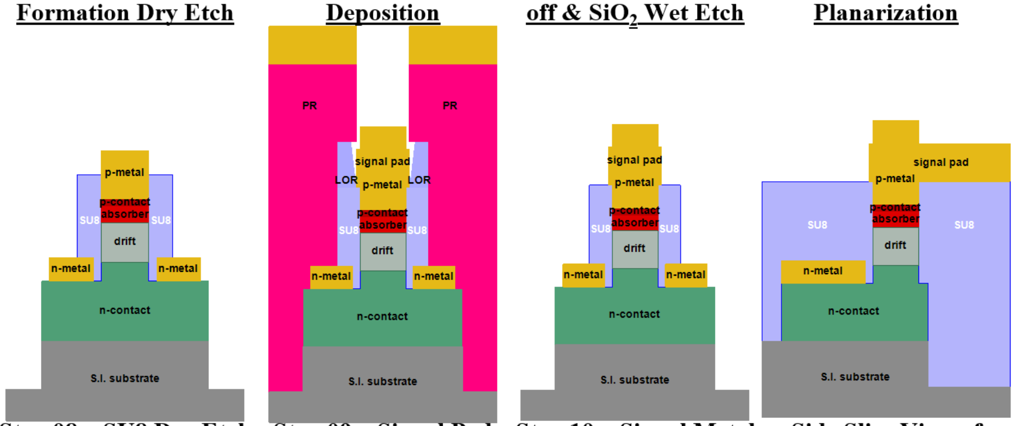

Step 08 – SU8 Dry Etch **Step 09 – Signal Pad Deposition** **Step 10 – Signal Metal Lift-off – Completed Device Front View** **Side Slice View of Completed Device**

Figure 6.10: Fabrication flow for new generation of surface normal photodiodes. Epi-stack layers and metal stacks shown to scale.

Chapter 7

Fabrication

To further push the performance of photodiodes towards the mmWave regime, a new method of surface normal photodiode fabrication was designed. The primary design constraints with device size (i.e. downscaling) and alignment tolerances were dictated by the equipment available to our group working in the cleanroom at UVA. This chapter will outline the lessons learned and adaptations needed to fabricate the smallest surface normal PDs fabricated by our group.

7.1 P-Mesa

In the past, the first step of the double-mesa fabrication procedure, the p-mesa step, has been a low-risk contact lithography and etch step. However, as we push towards smaller features, in particular 3-µm diameter dots, proximity of the chip to the mask becomes critical, as feature-size approaches the exposure wavelength. Edge-bead resulting from the spin-on of photoresist (PR) over a square chip (non-circular) surface in addition to any backside debris, then makes absolute flatness of the chip with respect to the lithography mask very difficult to achieve. Thus, in combination with a best effort edge-bead removal and backside cleaning after spinning resist, vacuum contact lithography helps push-out gaps present in hard-contact lithography. With any gap present between mask and chip, constructive interference of the light from the exposure lamp around the features of the mask, begins to degrade features from the inside out, for a sinc function type exposure. Figure 7.1a shows a microscope image after lithography and development, of a 3-µm PD p-mesa. In the inset, at 100X microscope objective, the color difference is just barely noticeable but shows an inner circle within the 3-µm dot that resembles that of the surrounding substrate, and a clear donut of PR. In Figure 7.1b, a microscope image shows the 3-µm PD p-mesa after dry etch of the SiO_2

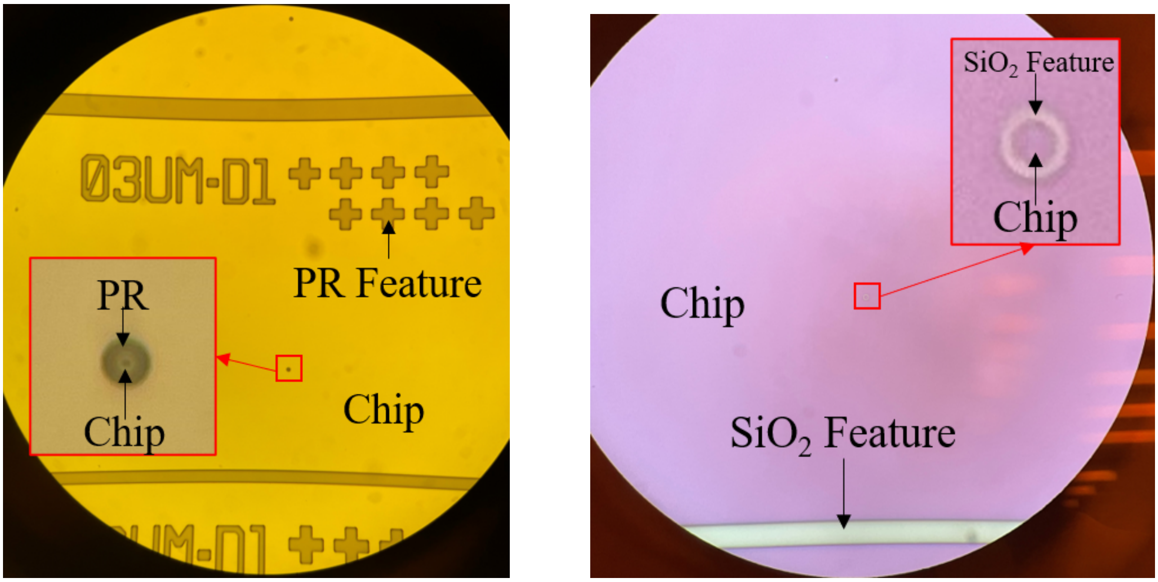

(a)

(b)

Figure 7.1: Microscope image of 3-µm p-mesa with donut structure after lithography (a) and after SiO_2 hard mask etch (b).

hard mask. Zoom in of the p-mesa shows the clear distinction of semiconductor vs. SiO_2. Scanning electron microscope (SEM) images shown in Figure 7.2 were taken and top view measurements of the donut hole of two different 3-µm PDs showed a hole size of approximately 320 nm in Figure 7.2a and 640 nm in Figure 7.2b, after a lithography exposure at 320 nm wavelength light. Figure 7.2c is a side view of the 3-µm PD in Figure 7.2b, verifying the depth of the donut structure which was measured to be approximately the thickness of the SiO_2 hard mask deposited on the chip. It should be noted that for some lithography iterations, especially when exposure time was increased during recipe optimization, donuts were also seen in the 4-µm PDs and in some 5-µm PDs. Too short of an exposure time led to underexposed larger features and no exposure of the smaller 3 and 4-µm dots. The donut structure was not observed in the 7-µm, 10-µm, and 14-µm PDs.

It was determined empirically, that with an appropriate exposure time, and precise edge-bead removal and back-side cleaning after PR spin, approximately 30-60% of the 3-µm diameter PDs could be successfully exposed and developed using standard hard contact lithography. However, with the addition of the SUSS MA6 aligner to the cleanroom, a consistent yield of greater than 90% of full-structured 3-µm dots could be achieved. The recipe for p-mesa in Appendix A pertains to use of the MA6 aligner.

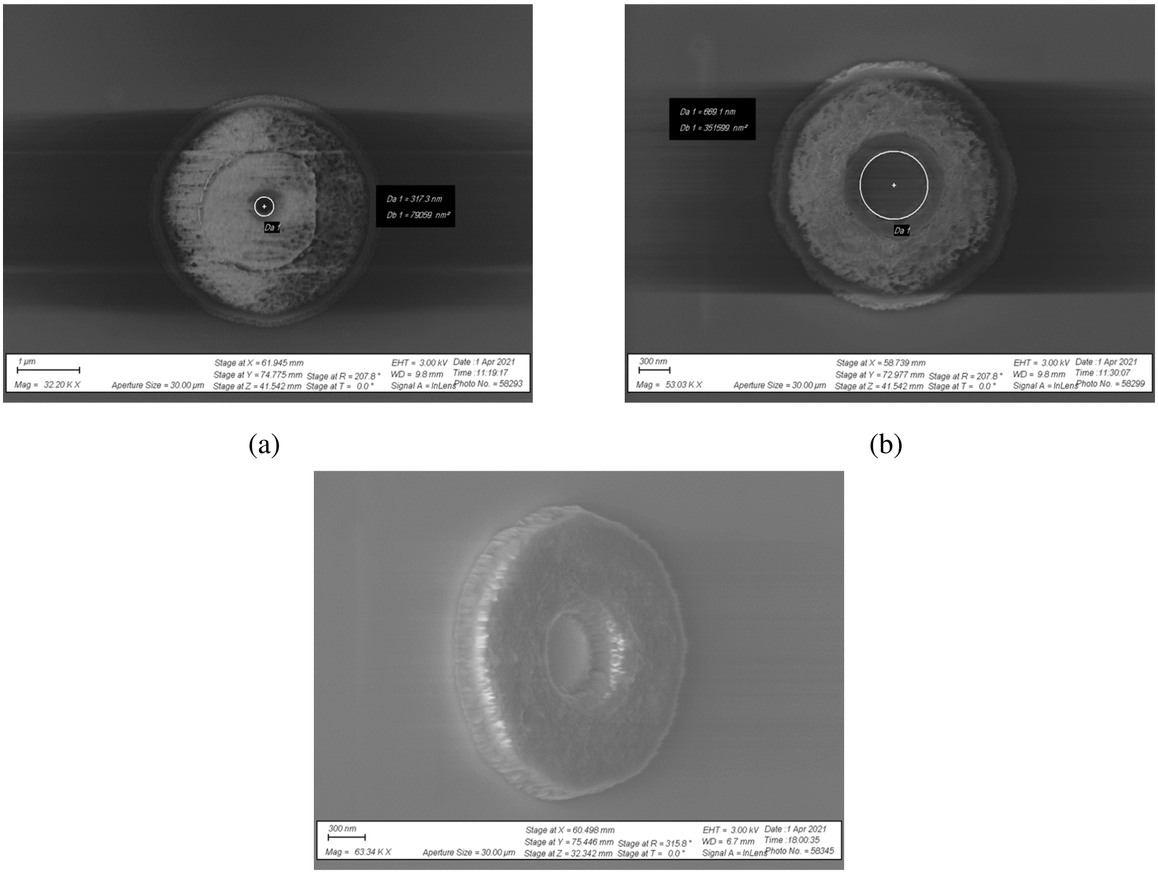

(a)

(b)

(c)

Figure 7.2: Scanning electron microscope images of SiO_2 p-mesa donut structure in 3-µm devices from top view (a) (b), and side view (c).

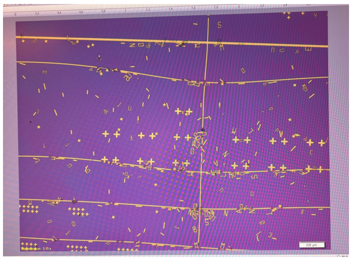

Figure 7.3: Microscope image of shifted photoresist features after development.

A second issue encountered with the p-mesa step, had to do with adhesion of PR to the sample, as shown in Figure 7.3. With relatively high fluctuations in humidity in the cleanroom, there was uncertainty with the repeatability of the spin-coating and soft-bake process. In prior years this issue was not common, which may further point to an issue with the smaller features being more difficult to work with. It was ultimately determined, that post spin of HMDS, a 3-5 minute bake at 110°C created a strong adhesion with the PR, and the issue was solved. Many thanks to Research Scientist in the UVA cleanroom, Jian Zhang, for his insights into a solution to the adhesion issue.

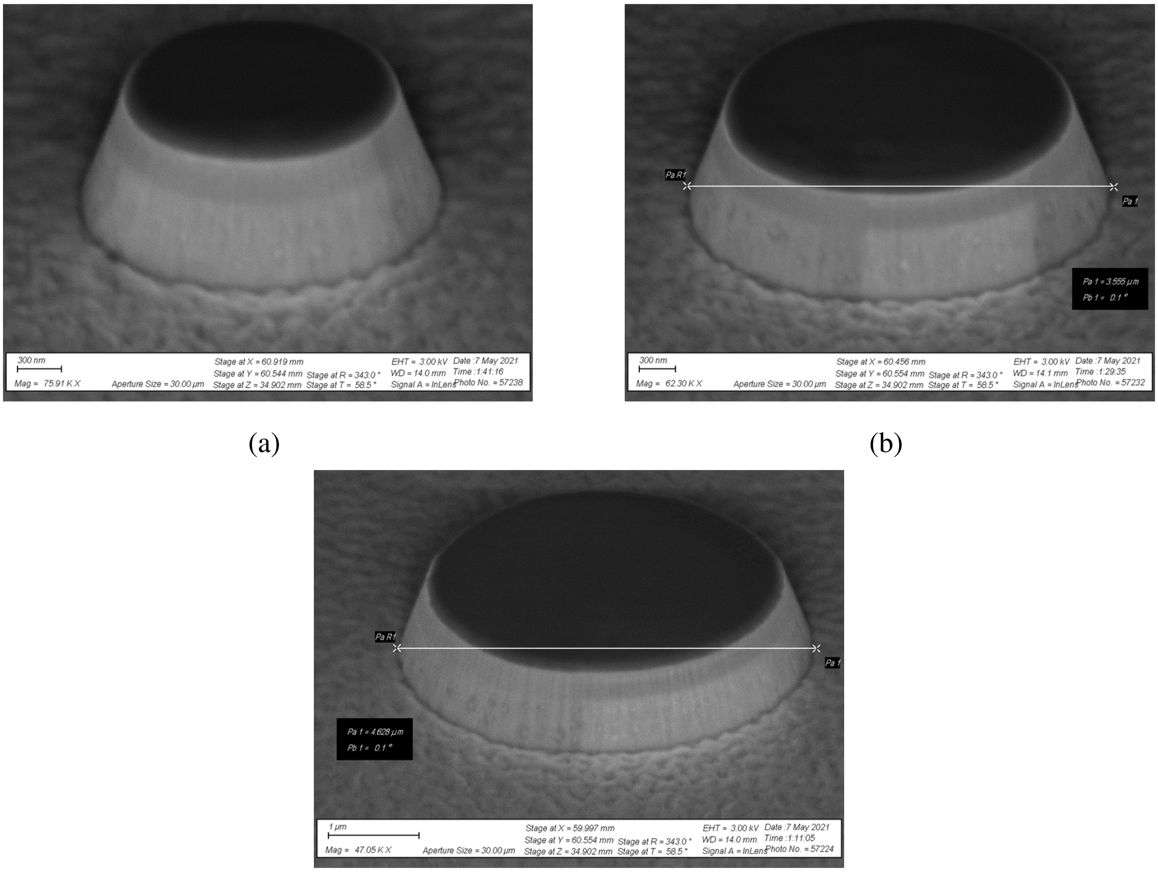

(a) (b)

(c)

Figure 7.4: Side-view SEM images of completed 3-µm (a), 4-µm (b), and 5-µm (c) p-mesa structures.

After correcting the aforementioned issues, the p-mesa recipe, as outlined in Appendix A, was applied to the samples. Figure 7.4 shows SEM images of 3, 4, and 5-µm diameter p-mesa devices. For the SiO_2 hard-mask etch, SiO_2 etched at a rate of $\approx$ 7 nm/min, with the PR etching at $\approx$ 4 nm/min. For the III-V etch, SiO_2 etched at $\approx$ 23 nm/min, GaAsSb at $\approx$ 115 nm/min, InGaAs at $\approx$ 110 nm/min, InAlGaAs at $\approx$ 180 nm/min, InP at $\approx$ 100 nm/min, and Au at $\approx$ 45 nm/min.

7.2 N-Mesa

The second lithography step in the double-mesa process, the n-mesa, was repeatable and consistent with n-mesa fabrication in previous years. With the lack of access to a plasma enhanced chemical vapor deposition (PECVD) machine, however, in lieu of a second SiO_2 hard mask for the n-mesa, photoresist AZ-4330 was used, as documented in Appendix A. After etch of the n-mesa and PR removal, the structures were measured using a profilometer, and the feature sizes matched the mask design. The etch rate for AZ-4330 was $\approx$ 180 nm/min. A new recipe for n-metal was developed to accommodate the lack of SiO_2 hard-mask benefits with lift-off, and will be documented in the following section.

7.3 N-Metal

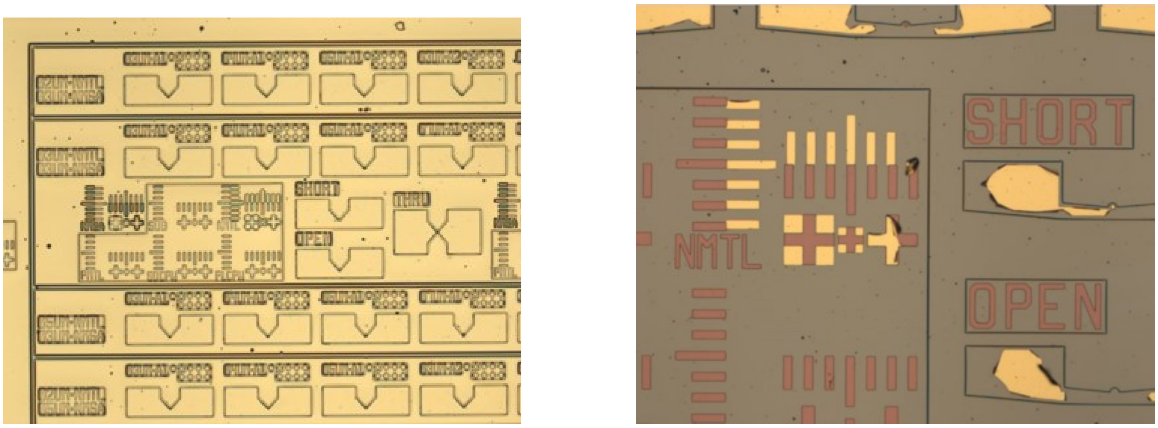

(a)

(b)

Figure 7.5: N-metal step with n-metal deposited on chip (a) and n-metal after lift-off (b).

After etching the chips to the substrate to form the n-mesa, n-metal lithography, metal deposition, and metal lift-off were done to form the n-contacts and RF ground planes for the devices. The recipe for this process has been passed down for years in the group with no issues related to metal adhesion to n-contact epi. This time however, during lift-off involving an acetone soak and low power sonicator, the gold on the n-mesa lifted off either in pieces or completely. Shown in the microscope images in Figure 7.5, Figure 7.5a is a sample after n-metal deposition with the result after lift-off shown in Figure 7.5b. It can be seen, particularly around the corners of the n-metal pads, that metal has peeled up or completely lifted off. When using SiO_2 as a hard mask, immediately prior to step 6 of Figure 2.3, an SiO-2 selective wet etch with BOE is done to remove the SiO_2 inside the n-metal opening. Even with a thin, $\approx$ 40 nm layer of SiO_2 removed, enough undercut is generated with the PR to create the separation needed between the metal on the sidewall of the PR and the metal on the n-contact, to result in successful lift-off of the metal. Now using AZ4330 resist in lieu of SiO_2 hard mask to etch the n-mesa, the lack of hard mask etch prior to n-metal deposition was unsuccessful. With an adhesion problem we would expect to see metal lost during lift-off originating more towards the center of the pads, but in this case, as can be seen in Figure 7.5b, the lost metal is around the edges, where the metal on the sidewall of the PR would be easily lifted up if the link between n-mesa and PR were continuous. In order to remedy this, LOR (i.e. lift-off resist) was incorporated into the recipe. LOR is able to create an undercut, separating the sidewall of the PR from n-mesa. It should also be noted, that the etch of SU8, does etch metal, albeit at a slow etch rate. However, if an initial SU8 coating needs to be completely removed for a second coating, significant removal of the n-metal can occur. With this in mind, it is recommended that if repeating this recipe, the n-metal deposition be increased from 150 nm, to 300 nm.

Another tolerance I hoped to gain some insight into with respect to the n-metal, was sidewall coverage, and if our 120 nm thick n-metal could connect the n-mesa to the substrate via deposition on the sidewall. Especially as we push towards efforts such as monolithocally integrated antennas and PDs, the ability to deposit a continuous metal from n-contact to substrate alleviates the need for plating, which ultimately reduces the number of lithographies and complexity in device fabrication. Figure 7.6 shows a series of SEM images of a log-periodic antenna monolithocally

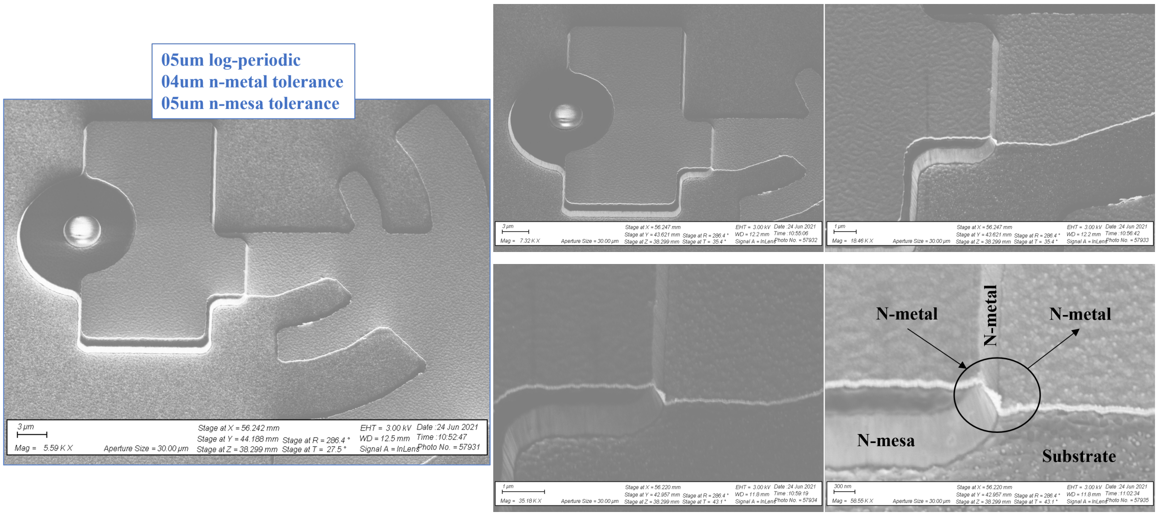

Figure 7.6: SEM images of successful n-metal sidewall coverage from top of n-mesa to substrate.

integrated with one of the 03-µm diameter photodiodes. The SEM shows that sidewall coverage was achieved. A simple DC continuity test also verified the result.

7.4 SU8 Planarization

The majority of lessons learned happened with the SU8 planarization step. SU8 offers a number of challenges when trying to achieve a planar surface across square-edged and sometimes oblong shaped (non-circular) chips. I will detail in this section each challenge faced and the solution found.

7.4.1 Spin-on Uniformity

When working with less viscous material such at AZ514 and LOR, a fast ramp and fast spin-on of non-circular samples generally results in minimal/easily corrected edge bead, and uniformed coating. SU8, however, requires more attention to ramp and spin speed in order to achieve the best possible uniformity with coating. Even with attention to this detail, it is still common to see variance in SU8 thickness from one region of the chip to another of up to 300 nm. It is thus recommended, that when using samples of non-circular shape, and attempting to use SU8 as an exposure/planarity tool, to allow at least 500 nm of tolerance of SU8 with respect to the surface to be exposed. While better than 50% yield was achieved in the Hong Kong sample, an initial p-metal deposition of 500 nm as opposed to 300 nm, would've relaxed the SU8 tolerance and dramatically improved yield across the chip. A number of spin speed ramps and terminal velocity combinations were tried. Ultimately and as outlined in the recipe in Appendix A, implementation of ramp speed and terminal velocity was adopted from SU8 data sheets. Edge-bead removal with acetone and swab after soft bake was especially critical as prior to soft bake, acetone was more prone to move inward on the chip and affect other portions of the SU8.

7.4.2 Uniformity vs. Feature Size

After the post-exposure bake and especially prevalent after cure baking, was a cliff-like edge on the perimeter of the SU8 features. While the height of this cliff did decrease after switching from 320 nm exposure wavelength to 365 nm exposure wavelength, it still remained. There are two places that this became an issue. The first, is with respect to actual etching down to the p-mesa. The initial SU8 mask gave roughly 5-µm of space between the edge of the p-mesa and the edge of the

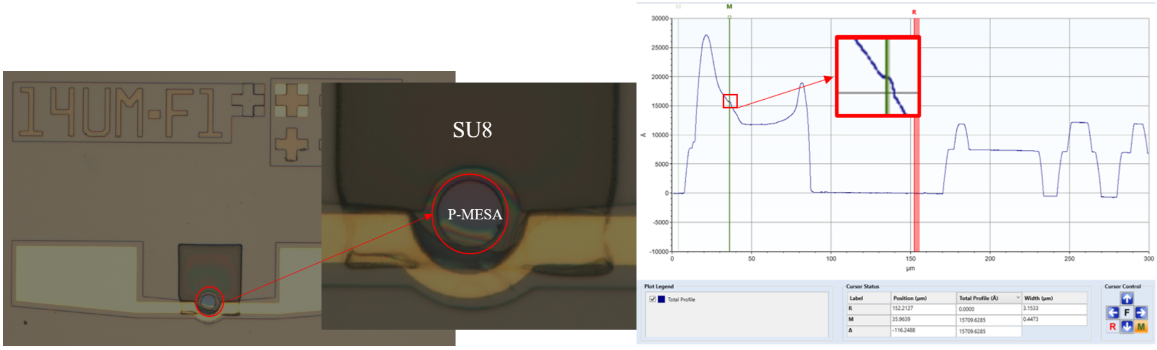

Label	Position (µm)	Total Profile (Å)	Width (µm)
R	152.2127	0.0000	3.1533
M	35.9639	15709.6285	0.4473
Δ	-116.2488	15709.6285	

(a)

(b)

Figure 7.7: N-metal step with n-metal deposited on chip (a) and n-metal after lift-off (b).

SU8 feature. However, this resulted in a semi-exposed p-mesa surface. The slope of the cliff-like edge, compounded with the ≈ 1 µm p-mesa feature height, led to a sidewall slope that left only a portion of the p-mesa sitting under a planarized surface of SU8. Shown in Figure 7.7a, a microscope image shows the uniform color of the exposed p-mesa surface in the first and second quadrants of the p-mesa, and the multi-colored surface of the SU8 still on top of the mesa in the third and fourth quadrants. A corresponding profilometer measurement of the device is shown in Figure 7.7b, where it can be seen that the cliff-like edge wall of the SU8 slopes directly towards the partially exposed p-mesa. A similar issue encountered with planarity occurred as a function of width of SU8 feature size. Across the chip, narrow pads on one side had a thicker SU8 across the portion of SU8 on substrate. To correct both of these issues, a new SU8 mask was designed. The width of the pads was standardized across devices on the chip, and the proximity of the SU8 edge to the p-mesa was increased up to 20 µm. The edge of the SU8 was sitting on top of the substrate, minimizing the towering affect over the p-mesa.

7.4.3 SU8 Etching and Surface Roughness

Ideally, when the p-mesa is exposed after etching the SU8, the surface is smooth with as much area of p-mesa exposed as possible, in order to promote as large as possible surface area for p-mesa contact with the signal pad. There are a few considerations with the etching of SU8 and surface treatment. The first is with respect to surface roughness. With a purely O_2 etch, antimony in the SU8 reacts with the O_2 to create localized masks [92], which, after minutes of etching, leads to up to 200 nm surface roughness. This can be alleviated by including some percentage of SF_6

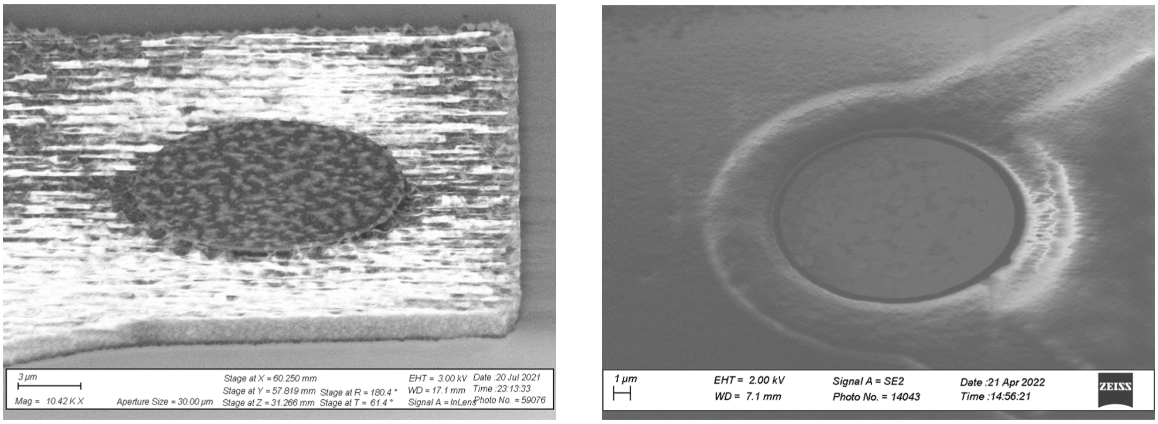

(a) (b)

Figure 7.8: Exposed p-mesa of 14-µm PD showing difference in surface roughness generated by Sb localized masking from SU8 using an etch recipe of O_2 only (a) vs. O_2 + SF_6 (b).

with the O_2 [92]. I used 10% SF_6 as documented in Appendix A. Shown in Figure 7.8a, is the exposed p-mesa for a 14-µm PD when using only O_2 as the etchant, and in Figure 7.8b a 14-µm PD using O_2 and SF_6 as the etchant. In Figure 7.8a, a clear correlation can be seen between the surface roughness of the SU8 surrounding the p-mesa, and the surface of the p-mesa itself. In Figure 7.8b, the SU8 surrounding the p-mesa shows minimal surface roughness, and the p-mesa itself shows a smooth surface. The slight discoloration on the p-mesa surface in Figure 7.8b can be attributed to the 10 nm of Ti partially etching away during the BOE wet etch of the SiO_2 hard mask. Profilometer measurements were taken across the mesa's to verify surface condition. Due to the introduction of SF_6, SiO_2 is also etched, albeit at a slow ($\sim$10 nm/min) rate. The final consideration with the etching of SU8 is the etching of Au. Although very slow, it still happens. So as a means of pre-emptive buffer, it is recommended that the n-metal be deposited at a thickness of at least 200 nm, should the SU8 need to be completely removed. Within the etch recipe itself, the pressure of the chamber is critical [92]. High surface roughness and inconsistent etch rates were found for chambers with pressure higher than 100 mTorr.

7.4.4 Recommendations for Future Use

There are tweaks to the recipe I used that can improve yield and ease of use when working with SU8 as a planarization tool. Because inevitably, even with the aforementioned fixes to planarity, there will be some variance in SU8 step height across the chip, in practice this variance was found to be a maximum around 300 nm. With a 300 nm initial p-metal deposition, and a p-contact layer thickness of 30 nm, the tolerance for etching to expose the p-mesa evenly across the chip without over-exposing and shorting the devices was small. Thus, the SU8 thickness/step height for the bulk of the devices in the center of the chip was prioritized, and the devices more towards the edge of the chip where the spin-coating was less evenly distributed were found to be either open or high in leakage current due to over-exposure of the intrinsic and sometimes n-regions. This could be solved by potentially increasing the thickness of the p-contact epi layer, or even more easily so by increasing the thickness of the initial p-metal deposition from 300 nm to 500 nm or more. Another fix to make SU8 more user friendly and mentioned previously, would entail increasing the n-metal deposition from 150 nm, to 200 or even 300 nm. When etching SU8 completely away for reprocessing of the SU8 step, the slow etch rate of the metal eventually matters; therefore, increasing the n-metal thickness allows multiple runs of SU8 without show-stopping the n-metal of the device. Finally, to make ease of testing and analyzing the planarity of the SU8, it is highly recommended that simple square structures made up of SU8 features on top of sub-features (p-mesa, n-mesa, n-metal) be fabricated alongside the devices, for easy side to side or top to bottom profilometer measurements. When dealing with a small 3-µm diameter p-mesa, and attempting to measure the step height of SU8 sitting on top of it, it is very difficult, whereas having a simple square structure close enough to the device to have the same SU8 step height, could aid in determining final uniformity and planarity across the chip. Also consider using SiO_2 instead of SU8.

7.5 Signal Metal

The signal metal step is straightforward. That said, LOR was used to aid in lift off. In previous surface normal PDs, the signal metal has been plated as an air-bridge using thick resist and acetone sonicator lift-off. To reduce the need for strong sonicator, as well as promote lift-off with a thick e-beam metal deposition, LOR can be used. Soak at 50° C in Remover PG to promote lift-off, then if needed, the sonicator can be used at minimal power for minimal time.

7.6 Backside Polishing

Backside polishing was done at UVA. Polishing pads on the chemical mechanical polishing (CMP) machine are crucial, as sandpaper method cannot achieve mirror/optical finish. The vacuum tube connected to the polisher inevitably exerts some force on the polishing jig, which can either push the chip into the pad to the point with the silicate fluid skirts around the chip, or pull the chip too far off the pad so that there isn't enough surface contact for the frictional polishing. It is important then to adjust the pressure control of the CMP jig, and position the vacuum tube such that the silicate fluid is able to distribute radially on the pad and under the chip. Once this balance was found, the chip was polished as long as 2 hours without any sign of movement.

Chapter 8

Optoelectronic Device Group Measurement Setup

This chapter will outline and detail the measurement setup shown in Figure 2.10 that has been put together to measure the mmWave spectrum in our lab.

8.1 Lasers

For 1550 nm tunable lasers, the lab has both thermally tuned distributed feedback (DFB) lasers, as well as mechanically tuned external cavity lasers (ECL). In practice, when tuning the DFB through a very large range of temperature in order to achieve RF beat note frequencies from DC to 100's of GHz, the laser being tuned demonstrates an increase in power, dependent on the increasing thermal tuning; it is necessary to re-equalize the power in the lasers to achieve 100% modulation depth. The ECL being tuned does not demonstrate any power dependence on the mechanical tuning and thus eliminates the need for repeated power equalization in the two lasers being beat together from DC-350 GHz. Although I tested the power drift in the DFBs from DC-110 GHz and found no significant affects on modulation depth, I decided to measure the devices with the ECLs both for the power stability and the more user friendly tuning mechanism.

8.2 RF Probes

The RF probes used to complete the measurements from DC-350 GHz consisted of a 1-mm coaxial probe from DC-110 GHz using an external bias-tee, and 3 rectangular-waveguide (WR) coupled probes for the frequency bands from 110-350 GHz. The 1-mm coaxial coupled GGB probe, model number 110H-GSG-150-P, had a 150-µm pitch, and used an external bias-tee. For the WR-6 band, 110-170 GHz, the GGB probe with model number 170-GSG-90-BT, used BeCu tips, a 90-µm pitch, and an integrated bias-tee with standard SMA connection. The WR-5 band operating from 140-220 GHz, used a GGB probe 220-GSG-150-BT, with the same tips and integrated bias-tee as the WR-6 probe, but with a larger pitch size of 150-µm, due to the CPW of the original project the probe was used for. The WR-3 band from 220-325 GHz (calibrated) used a GGB probe with model number 325-GSG-90-BT, also using BeCu tips, a 90-µm pitch, and built-in bias tee which uses a mini-SMP cable connection for the source meter. The manufacturer recommended a pitch size of 30 to 90-µm for the WR-3 band probe to achieve best performance.

8.3 Power Meters

Two different power meters were primarily used for the measurements. For the DC-110 GHz measurements, a Rohde and Schwarz (R&S) NRP-58 model power meter with 1-mm coaxial input was used. For 110 GHz and beyond, the PM5 power meter from Virginia Diodes Incorporated (VDI) was used. While these two power meters covered all frequencies of interest, a Keysight E441B power meter was sometimes used in the W-band frequency range (75-110 GHz) using a 1-mm coax to WR-10 conversion block, and upper V-band range (60 GHz) to corroborate measurements from the R&S.

8.4 Calibration

Calibration for DC-110 GHz required calibrating an external bias-tee link, RF probe, and frequency dependent power meters. The bias-tee link included a 4-cm long 1-mm coaxial cable connecting the RF probe to the bias-tee, and an SHF BT 110 B bias-tee operating from 50 kHz to 110 GHz. The calibration was done using a 2-port 10 MHz to 110 GHz Keysight PNA with 110 GHz extenders, which itself was calibrated with a 7-step SOLT and offset shorts calibration kit (short (4), open, load, through). The probe calibration data was taken from the manufacturer calibration data sheet. The RF power meters were set to the particular frequency of beat note being measured in order to apply their frequency dependent calibration. Calibration from 110-325 GHz involved calibration of the WR coupled probes and the WR tapered waveguide blocks that transitioned the probe output to the PM5. From DC-110 GHz, the frequency dependent bias-tee link loss was combined with the probe calibration using MATLAB, and for 110+ GHz the tapered waveguide block loss added to the probe loss. Figure 8.1 shows the fully calibrated measurement for the Ge PD frequency response. Good overlap is shown between the minimum and maximum frequency range for the 4 measured frequency bands. Small signal LCA measurements performed by IHP from DC-110 GHz and normalized to 1 mA for comparison, are shown in grey.

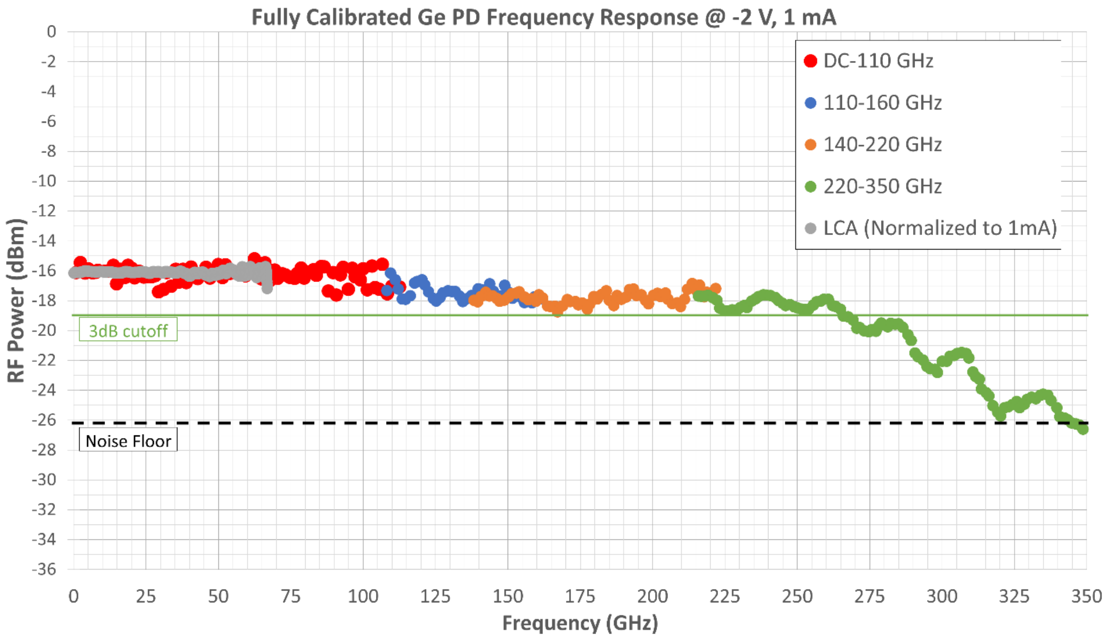

Figure 8.1: Fully calibrated (DC-325 GHz) frequency response for Ge PD measurement highlighting measurement overlap between 4 bands of measurement, measured at -2 V bias and 1 mA. Noise floor shown at maximum calibrated RF probe frequency of 325 GHz.

Chapter 9

Next Generation High Speed Photodiode Results

50-Ω Taper CPW Design

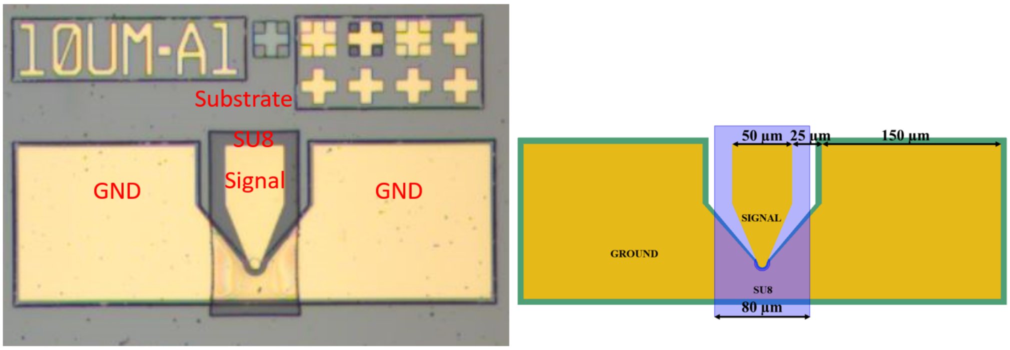

Minimal Metal Pads CPW Design

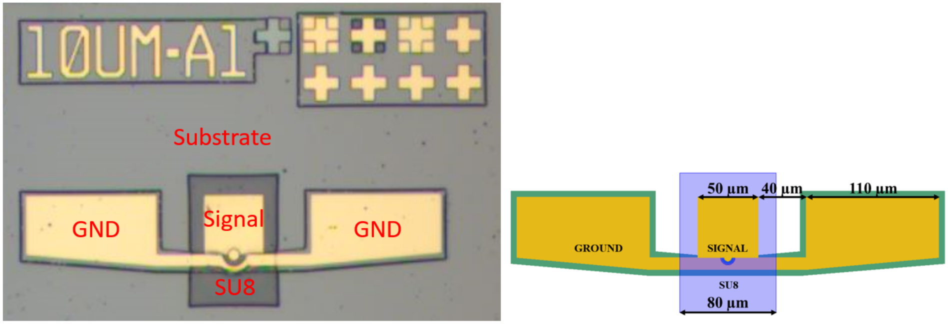

Figure 9.1: Microscope images of completed 10-µm PDs on 50-Ω taper CPW (top) and minimal metal pads CPW (bottom) along with ADS design and CPW dimensions from top view.

The fabricated devices, shown in Figure 9.1, were measured and characterized and are described in this chapter. The analysis is shown for the Hong-Kong epi (Figure 6.2a), which was successfully fabricated with the new fabrication procedure (Figure 6.10), and achieved better than 70% yield, or 49 working PDs out of 68 total PDs in one array. The NIST epi (Figure 6.2b) was also fabricated with working devices; however, as mentioned in Section 7.4.4, the tight tolerance with respect to the height of the p-mesa and the surrounding SU8, and the fact that this chip was the initial sample to undergo the full fabrication run, resulted in an over-etch of the SU8, leading to dark current on the order of µA's at $<$-1 V bias and a large percentage of devices with p-mesa shorted to the n-region. Therefore, measurements and characterization were only performed on the Hong Kong sample.

9.1 IV and Responsivity

IV curves taken on the Hong Kong devices are shown in Figure 9.2, for devices on the 50-Ω CPW Figure 9.2a and minimal metal CPW Figure 9.2b. At -3 V bias, on the 50-Ω CPW, the 03-µm PD has a dark current of 48 pA, 04-µm of 57 pA, 05-µm of 76 pA, 07-µm of 105 pA, 10-µm of 109 pA, and the 14-µm of 152 pA. This low dark current result speaks to the high quality of the epi material as well as the passivation from the SU8. Forward compliance is set to 1 mA, and is reached at or below 0.75 V bias in the 05, 07, 10, and 14-µm PD. The compliance is reached at higher bias for the 03, and 04-µm PDs, which will be discussed further in the S11 fitting results section.

Figure 9.3a shows the measured responsivity vs. input optical power for a 10-µm PD at 0 V bias and Figure 9.3b shows a 10-µm and 14-µm PD measured at -1.8 V reverse bias, at an optical wavelength of 1545 nm. The measurement was done using an 8-µm spot-size, collimated lensed fiber. At 0 bias the average responsivity is 0.08 A/W, with a relatively flat responsivity. The average responsivity for both PDs at -1.8 V is 0.1 A/W. At low optical power the responsivity is $\sim$0.075 A/W. With increasing optical power, the responsivity increases until flattening out at 0.11 A/W in both devices. The dependency on optical power could be attributed to the fact that there is no blocking layer, and at low optical power, with low current the self-induced field in the undepleted absorber is also low[93]. This means electrons can diffuse more easily into the p-contact and recombine, and therefore not contributing to the DC photocurrent. With increasing optical power, the self-induced field increases as well, supporting electron transit to the drift layer where they can then be collected. This responsivity was measured after backside polishing of the PD chip to achieve approximately

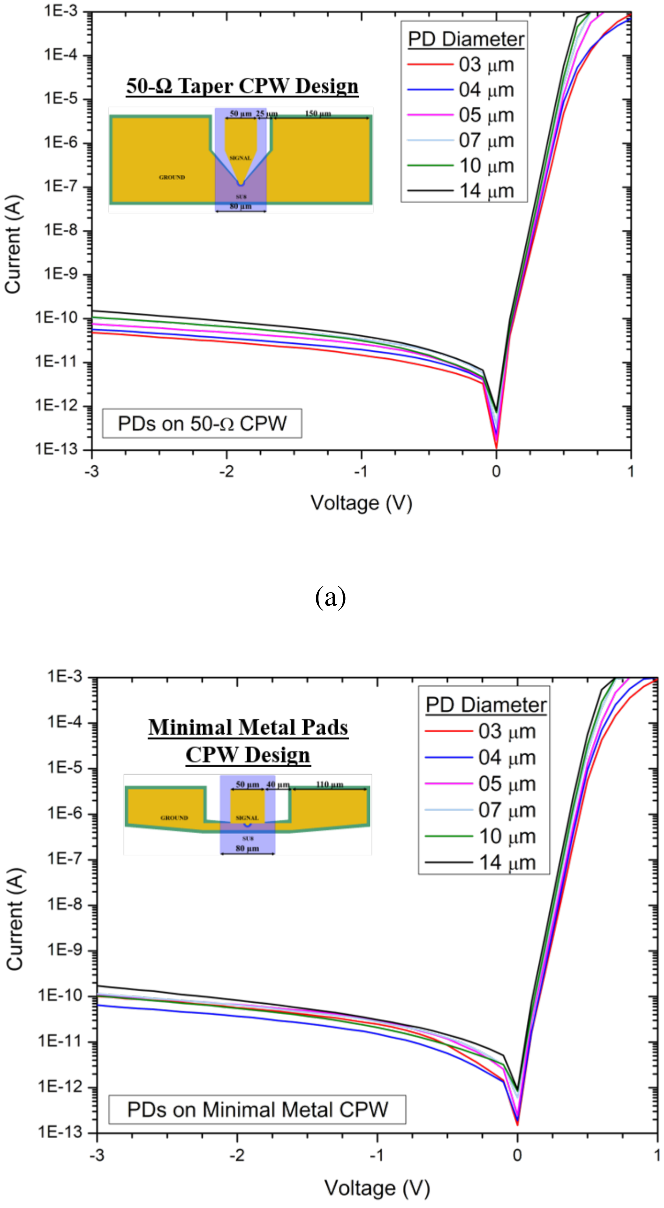

(a)

(b)

Figure 9.2: IV curves for Hong Kong sample for devices on the 50-Ω CPW (a) and minimal metal CPW (b) measured from -3 V to 1 V.

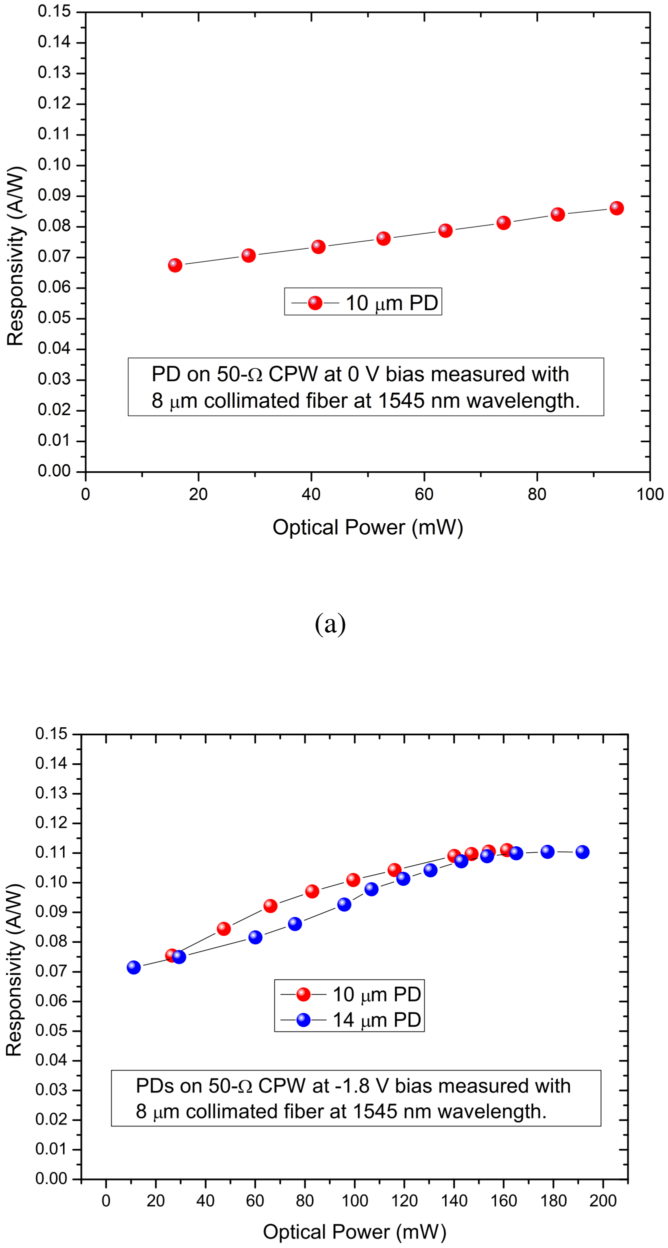

PD on 50-Ω CPW at 0 V bias measured with 8 μm collimated fiber at 1545 nm wavelength.

(a)

PDs on 50-Ω CPW at -1.8 V bias measured with 8 μm collimated fiber at 1545 nm wavelength.

(b)

Figure 9.3: Responsivity curves for a 10-μm PD at 0 V bias (a) and a 10-μm and 14-μm PD at -1.8 V bias (b) measured at 1545 nm using an 8-μm collimated lensed fiber.

a mirror finish. Responsivity was also measured before backside polishing, and was measured to be ∼0.002 A/W, which was too low to effectively measure saturation power in the PDs. There was no anti-reflection AR coating on the sample. With AR coating, we should achieve a responsivity ca. 27% higher, or 0.14 A/W under bias, close to that calculated and shown in Figure 6.7. With AR coating, responsivity at zero bias should be 0.1 A/W. Compared with the FUTC generation, the absorber thickness has been decreased by 60%, and with AR coating responsivity should only be reduced by 30%, which bodes well for the absorption in GaAsSb.

9.2 S11, Parameter Fitting and Bandwidth

S11 measurements were taken up to 110 GHz on the devices at various bias voltages using a Keysight PNA with 110 GHz extender. A 150-µm pitch GSG GGB RF probe was used with an external, 110 GHz bias tee, and calibration was done using the GGB CS-5 calibration substrate. The PD circuit model shown in Figure 6.9 was used to fit the data.

Figure 9.4a and Figure 9.4c show the results of the S11 measurement at -1 V bias (blue), along with the fitting results (red) and the originally calculated values (black), for a 10-µm and 07-µm PD, respectively. Figure 9.4b shows the bandwidth results for a 10-µm PD on 50-Ω CPW, measured at -1 V bias and 2 mA (blue), also compared to the fitted results (red) and originally calculated results (black). A second order polynomial fit of the bandwidth measurement from DC-180 GHz shows a 3-dB bandwidth of 84 GHz. Calculated bandwidth for the device was 86 GHz. Figure 9.4d shows the bandwidth results for a 07-µm PD on minimal metal CPW, also measured at -1 V bias and 2 mA (blue), compared to the fitted results (red) and originally calculated results (black). A second order polynomial fit of the bandwidth measurement from DC-220 GHz shows a 3-dB bandwidth of 100 GHz. Calculated bandwidth for the device was 124 GHz.

The results of the S11 fitting and bandwidth for PDs on the 50-Ω CPW are summarized in Table 9.1, and the bandwidth measurements are shown in Figure 9.6 (spheres) along with their second order polynomial fits (solid lines). The fitted junction capacitance, C$_{pn}$ fit, was close to the calculated value, C$_{pn}$ Calc., for all sized PDs. Figure 9.5 shows the plot for the calculated and fitted junction capacitance values. A linear fit of the extracted values at -1 V bias is used to determine the stray capacitance, C$_{st}$ in the devices. This value is found to be 1.5 fF, which is ∼0.5 fF higher than that calculated in Section 6.2. It should be noted that this number represents more than a 4x reduction in stray capacitance compared to the backside illuminated FUTC. The extracted series resistance is also shown. Larger resistance was found for smaller devices. Larger area PDs have

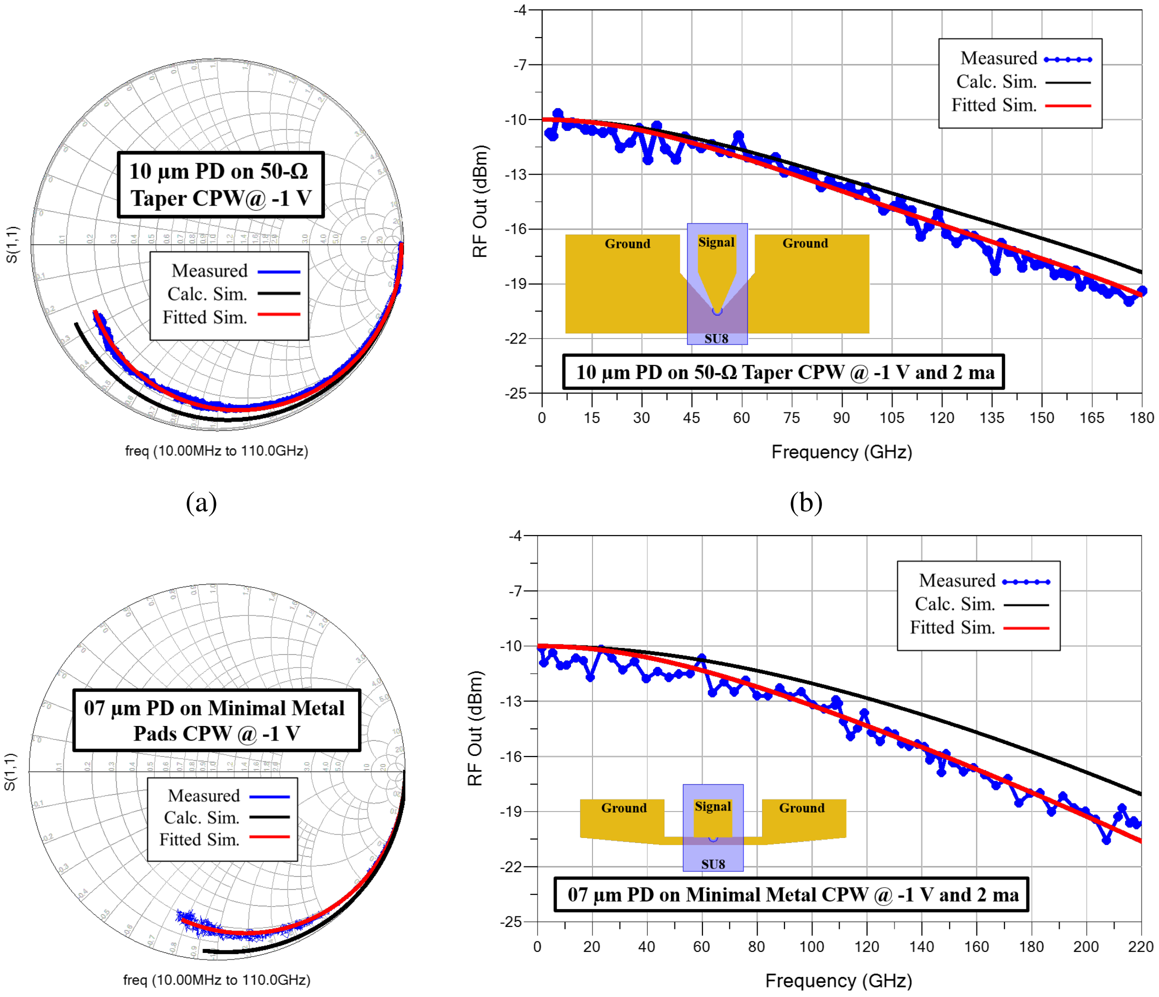

(a) (b)

(c) (d)

Figure 9.4: Measured data (blue) vs. calculated simulation (black) vs. S11 fitted simulation (red) for S11 (a) and bandwidth (b) for a 10-µm PD on 50-Ω CPW, and a 07-µm PD on minimal metal pad CPW S11 (c) and bandwidth (d). Bandwidth was measured at -1 V bias and 2 mA photocurrent.

PD Diameter	C_{pn} Calc.	C_{pn} fit	R_s	f_{3dB} Calc.	f_{3dB} @ -1V 2mA
03-µm	2.4 fF	3.8 fF	200 Ω	179 GHz	15 GHz
04-µm	4.3 fF	6 fF	110 Ω	173 GHz	67 GHz
05-µm	6.7 fF	8.7 fF	50 Ω	164 GHz	–
07-µm	13.1 fF	16.8 fF	26 Ω	132 GHz	>110 GHz
10-µm	26.7 fF	28 fF	14 Ω	86 GHz	84 GHz
14-µm	52.4 fF	56.4 fF	10 Ω	50 GHz	42 GHz

Table 9.1: Fitted circuit parameters from S11 data for PDs on 50-Ω CPW measured at -1 V bias.

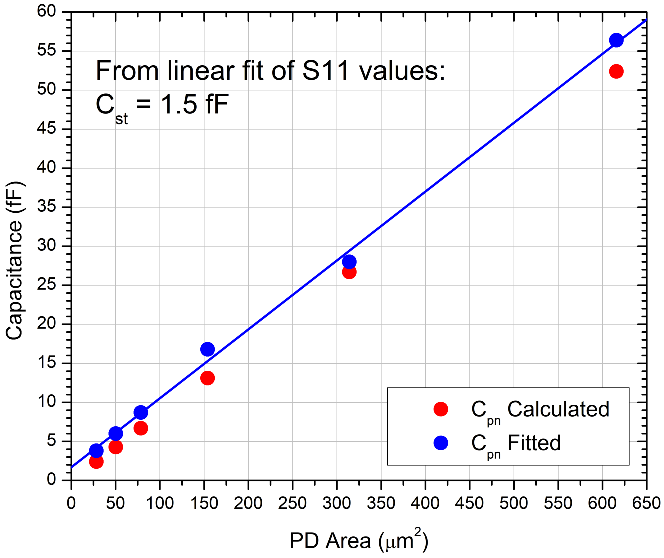

Figure 9.5: Junction capacitance calculated (red) and fitted from S11 (blue) for all devices at -1 V bias.

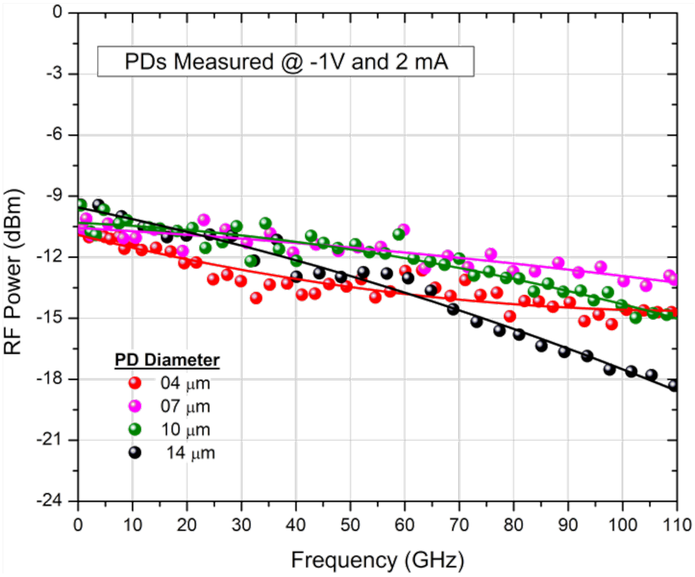

Figure 9.6: Bandwidth measurements for PDs measured at -1 V bias and 2 mA.

lower lateral resistance as current has more cross-sectional area to flow through, and while this resistance is relatively low, it could still contribute to the larger resistance extracted in the smaller PDs. Another potential contributor to the higher series resistance is the p-contact resistance. The SIMS shown in Appendix B show that the doping density was around the designed value. However, while the dopants exist in the p-contact, there is the possibility that they are electrically inactive, and therefore don't sit on a lattice spot and replace a host atom, thus leading to a mesa size dependent contact resistance. One of the questions that arises as we push towards smaller devices is where the trade-off in smaller capacitance for larger resistance begins to hold back performance.

9.3 Saturation Power

To determine the optimum bias voltage for saturation power measurements, RF power was measured over a range of bias voltages, near the saturation power point, in a 10-µm and 14-µm PD. The result is shown in Figure 9.7. At -1.8 V bias, the peak RF power output is reached in both devices. This decreasing power output at higher field potentially comes from velocity overshoot in the InP collector. At relatively low electric field, electrons travel much faster than at higher fields when they reach their saturation velocity. Saturation power measured at -1.8 V at 100 GHz and 160 GHz is shown in Figure 9.8. In Figure 9.8a at 100 GHz, a 14-µm PD reaches 5.8 dBm at 37.5 mA, and at 160 GHz in Figure 9.8b, a 10-µm PD reaches 1.23 dBm at 25.1 mA. Figure 9.9 shows power

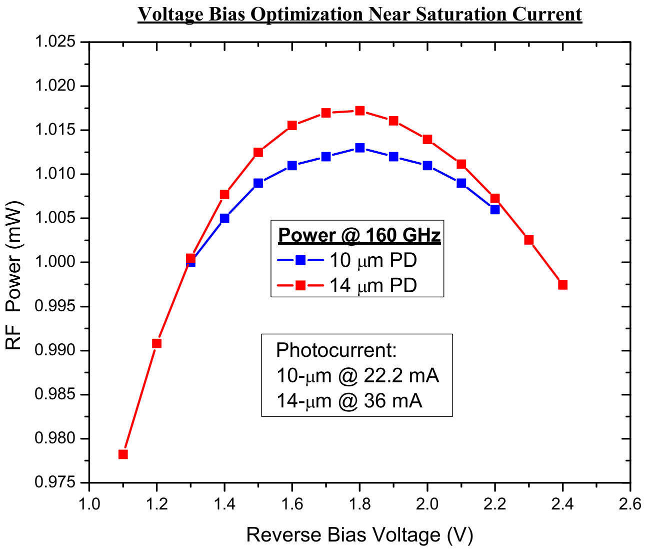

Figure 9.7: 160 GHz RF output power near saturation point vs. bias voltage for a 10-µm PD at 22.2 mA photocurrent and 14-µm PD at 36 mA photocurrent.

measured at -1.8 V at 220 GHz, and at 300 GHz. At 220 GHz, in Figure 9.9a, a 10-µm PD reaches -3.07 dBm at 24.7 mA, and at 300 GHz in Figure 9.9b a 10-µm PD reaches -10.5 dBm at 25.3 mA.

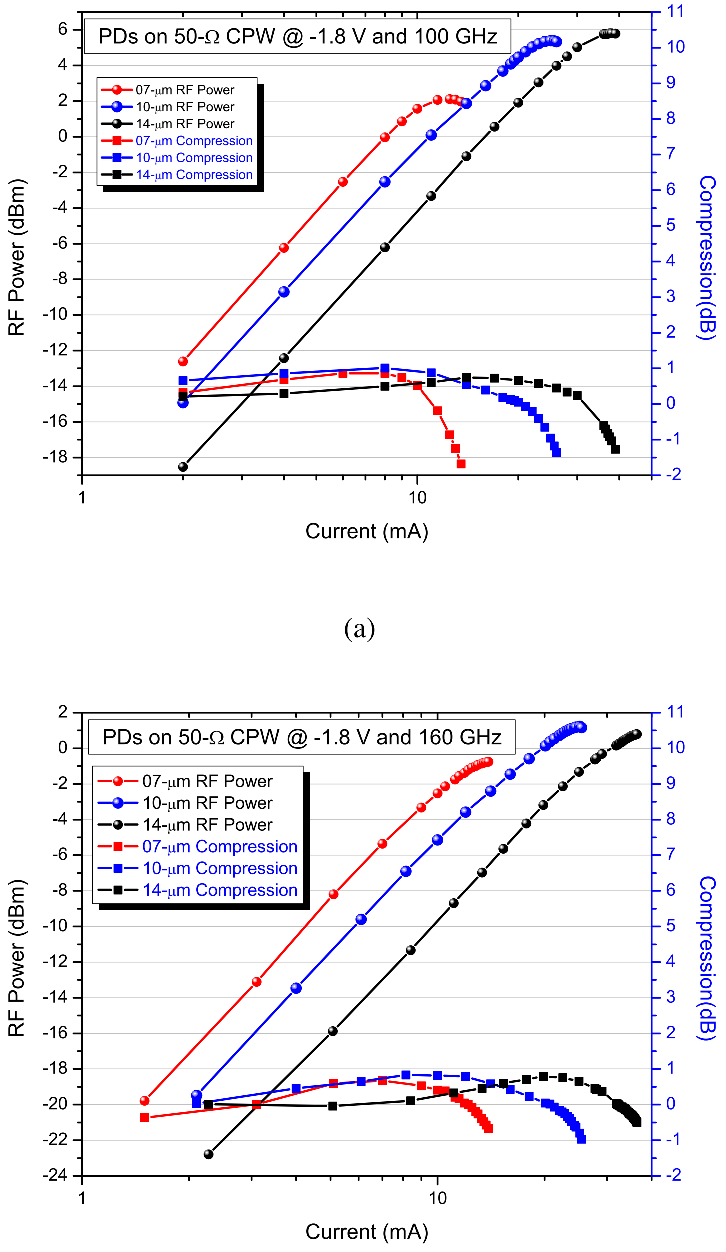

(a)

(b)

Figure 9.8: Saturation power and compression measured at -1.8 V bias and (a) 100 GHz and (b) 160 GHz for a 07-µm, 10-µm, and 14-µm PD.

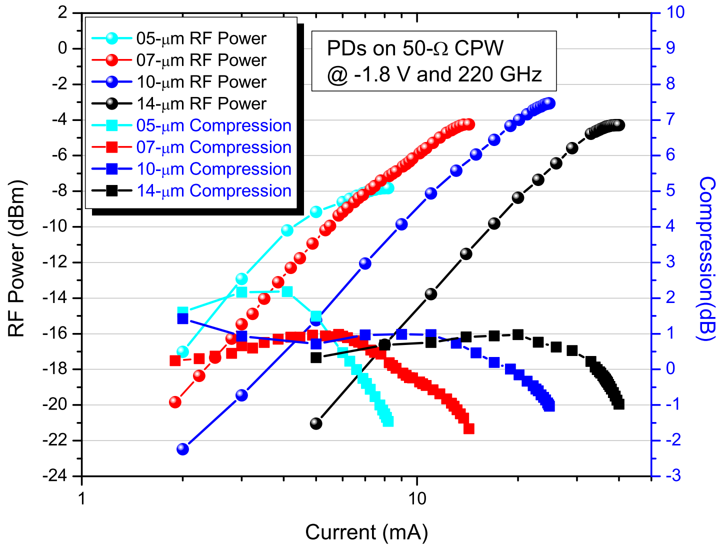

(a)

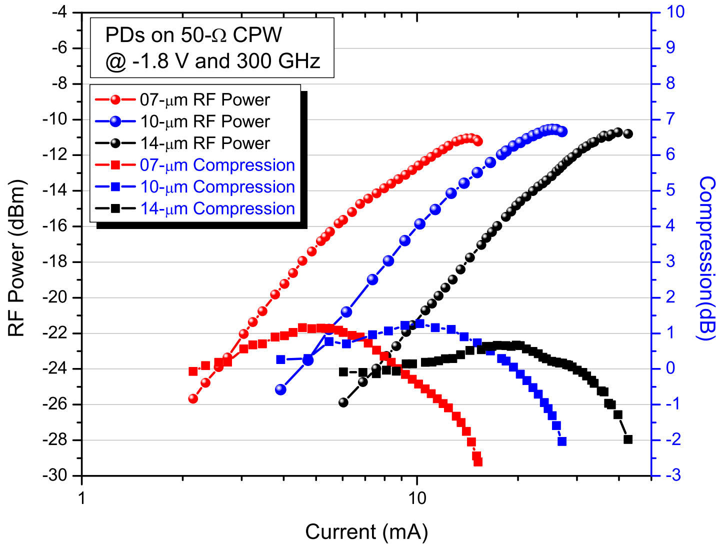

(b)

Figure 9.9: Saturation power and compression measured at -1.8 V bias at (a) 220 GHz for a 05-µm PD, 07-µm, 10-µm PD, and 14-µm PD and (b) and at 300 GHz for a 07-µm PD, 10-µm PD, and a 14-µm PD.

9.4 Zero-Bias Operation

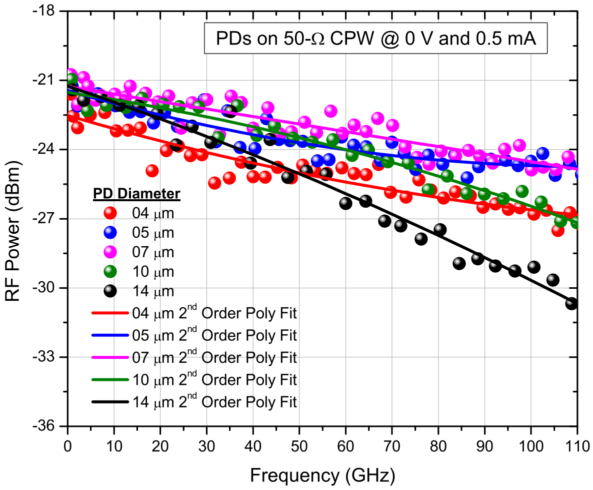

Figure 9.10: Bandwidth measurements for all PDs measured at 0 V bias and 0.5 mA.

With the type two band-alignment as shown in Figure 6.1, the natural slope in the conduction band leading from the GaAsSb absorber to the InP collector, promotes zero-bias operation. Figure 9.10 shows the bandwidth measurement result for various sized PDs measured at 0 V bias and 0.5 mA. From a second-order polynomial fit (solid lines), a 07-μm PD achieves a 3-dB bandwidth of 92 GHz. Figure 9.11 shows the bandwidth measurement result for a 07-μm (red dots), 10-μm (blue dots), and 14-μm (black dots) PD measured at 0 V bias and 1 mA. From a second-order polynomial fit (solid lines), the PDs achieve a 3-dB bandwidth of 89 GHz, 65 GHz, and 39 GHz, respectively. A summary of the resulting bandwidths is shown in Table 9.2.

PD Diameter	0 V @ 0.5 mA	0 V @ 1 mA
04-μm	61 GHz	–
05-μm	80 GHz	–
07-μm	92 GHz	89 GHz
10-μm	68 GHz	65 GHz
14-μm	40 GHz	39 GHz

Table 9.2: Measured 3-dB bandwidth results at zero-bias.

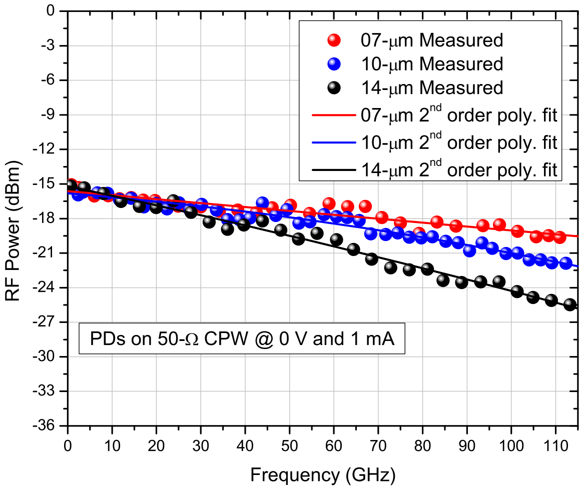

Figure 9.11: Measured data for a 07-µm, 10-µm, and 14-µm PD measured at 0 V bias and 1 mA.

Saturation power measurements are shown in Figure 9.12 and Figure 9.13 at 100 and 160 GHz, and 220 and 300 GHz, respectively. A 10-µm PD reaches -9.3 dBm at 7 mA at 100 GHz, -12.2 dBm at 8 mA at 160 GHz, -14.5 dBm at 8 mA at 200 GHz, -14.3 dBm at 7.6 mA at 220 GHz, and a 07-µm PD reaches -19.3 dBm at 4.9 mA at 300 GHz.

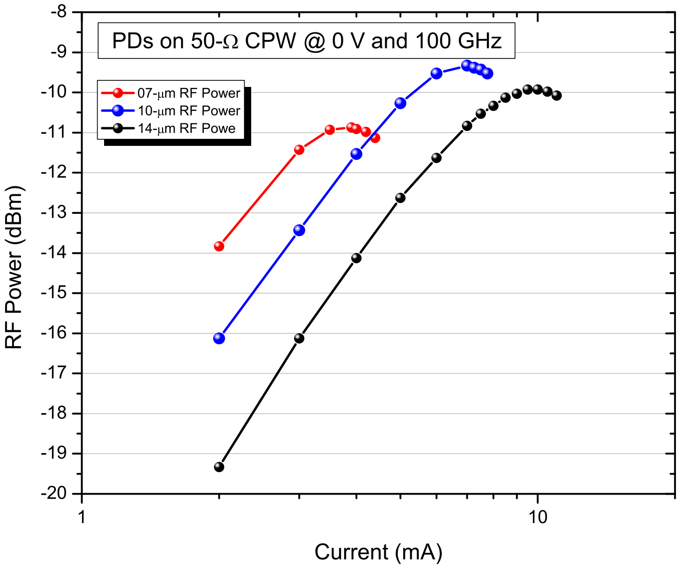

(a)

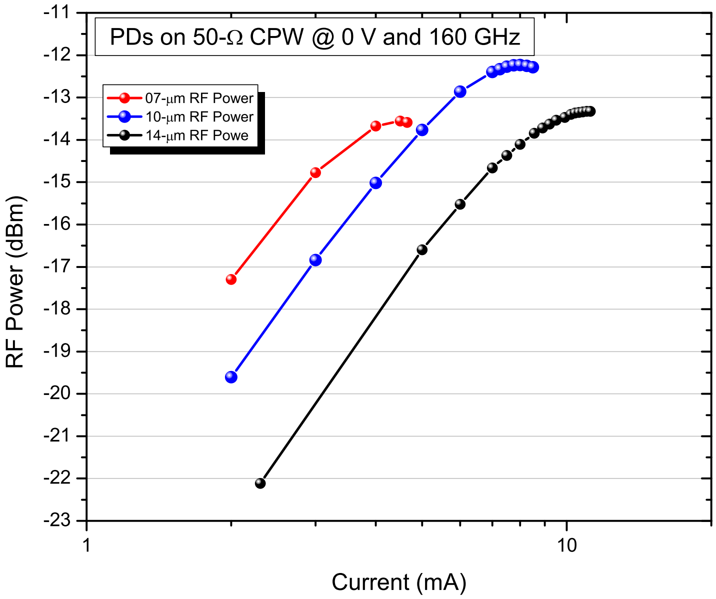

(b)

Figure 9.12: Saturation power measured at zero bias and (a) 100 GHz and (b) 160 GHz for a 07-μm, 10-μm, and 14-μm PD.

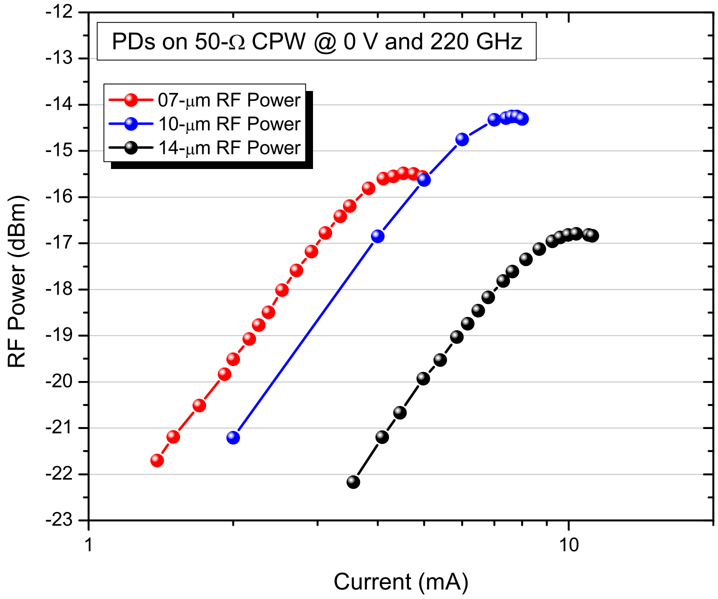

(a)

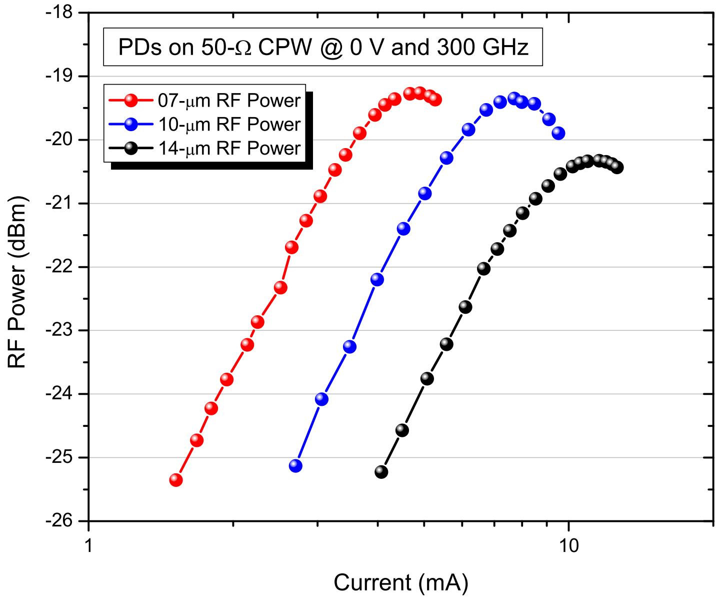

(b)

Figure 9.13: Saturation power measured at zero bias and (a) 220 GHz and (b) 300 GHz for a 07-μm, 10-μm, and 14-μm PD.

9.5 Summary

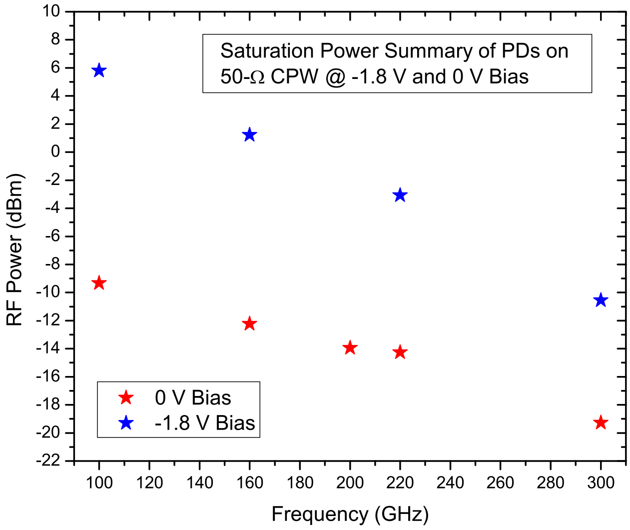

Figure 9.14: Saturation power at 100, 160, 200, 220, and 300 GHz at zero bias (red star) and under bias (blue star) for new generation of PDs.

I have designed high-speed, high-power MUTC photodiodes operating at 1550 nm, using a new epitaxial stack, new device design, and new fabrication procedure for surface normal photodiodes. These PDs achieve 3-dB bandwidths of more than 110 GHz at -1 V bias and 2 mA, and 92 GHz at 0 V bias and 0.5 mA. They achieve a flat roll-off, as evidenced by the saturation power performance over the range of 100 GHz to 300 GHz. They achieved their expected responsivity without anti-reflection coating of 0.1 A/W. The type II band alignment enables zero bias operation, and power levels in the range of 100 GHz to 300 GHz are also demonstrated and shown in Figure 9.14.

Comparing the results of this new generation of PDs to the previous generation of backside illuminated, flip-chip bonded FUTC PDs, we find that the responsivity was higher in the FUTC. As noted previously, this makes sense as the absorber was 60% thicker in the FUTC epi and the FUTC epi utilized an anti-reflection coating on the surface whereas the Hong Kong sample did not. With AR coating we should achieve a responsivity of 0.14 A/W, which is only 30% lower than FUTC. Thus we gain the potential for faster devices with only slightly reduced efficiency. Addition-

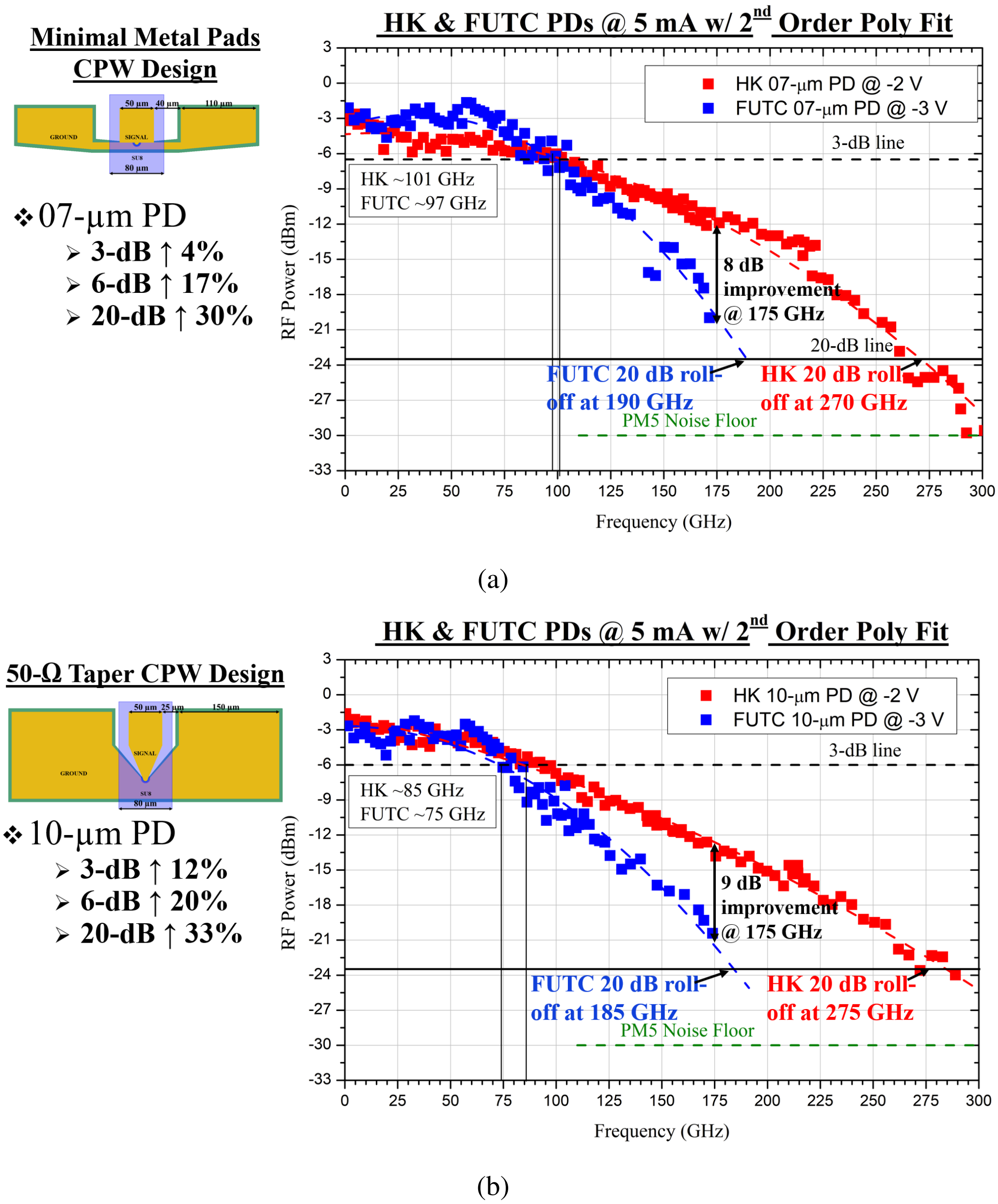

Figure 9.15: Frequency response comparing FUTC and new generation of PD for a 7-µm on minimal metal pads CPW (a) and a 10-µm on 50-Ω taper CPW (b).

ally, and as suggested in Chapter 6, by changing the top p-metal from Ti to a higher reflectivity Pd, we might be able to boost the responsivity closer to 0.19 A/W. As shown in Figure 9.15, bandwidth for the HK devices versus FUTC, on minimal metal pads CPW for 07-µm PDs was 4% higher and in the 10-µm PD on 50-Ω CPW was 12% higher. In terms of frequency response and roll-off through the mmWave spectrum, the 10-µm HK PD on 50-Ω submount achieved a 20% increase in the 6-dB roll-off point, a 9-dB improvement in power at 175 GHz, and the 20-dB down point was improved by 33%, being taken from 185 GHz in FUTC to 275 GHz. The improvements in frequency roll-off were similar for the 7-µm PD on minimal metal pads CPW as shown in Figure 9.15a. For saturation power, two big takeaways are found in the data. Firstly, at higher operating frequencies, if we compare power output in the HK devices to the FUTC generation, we do not need flip-chip bonding to achieve higher power at high frequencies. This will reduce fabrication complexity in the future. Secondly, it is seen that the 14-µm PD gives the highest output power at 100 GHz, and 10-µm at 160, 220 and 300 GHz, while the 07-µm PD begins to have comparable power at 300 GHz. This shows that the roll-off impacts the maximum RF power proportionally to the operating frequency. Further investigation into PD diameters in between those measured might lead to even higher output power for a given frequency. Due to the high R_s in the 3-µm and 04-µm PDs, their roll-off was fast and resulted in very low bandwidth. These results point to diameters between 10-µm and 07-µm PDs being the optimum size for these mmWave frequencies.

The saturation power results of these PDs are shown in Figure 9.16, comparing the results to the literature. The blue cross-stars represent the results at -1.8 V bias. The green cross-stars represent the results a 0 V bias. The collection of points around 300 GHz come from exotic structures like multi-PD arrays. The data at 200 and 220 GHz sits alone. The data at 160 GHz shows the $\sim$4 dB improvement in these devices as compared to the flip chip bonded FUTC generation (red stars). The broad coverage capability of the new PDs does limit their power output at 100 GHz, but as shown, they are still within $\sim$ 4 dB of the record power for single device PDs, which also happens to be the FUTC (red triangle). At 160 GHz at 0 V bias, the new PDs achieve $\sim$ 2 dB higher output power than the previously reported 160 GHz 0 bias PD (pink donut). Furthermore, the pink data points show other zero-bias PDs, which were designed specifically for zero-bias operation, with low doping in the drift layer. These structures, when biased, show only a few dB improvement, whereas the new generation of PD I have designed, offers robust performance both at zero bias and under bias.

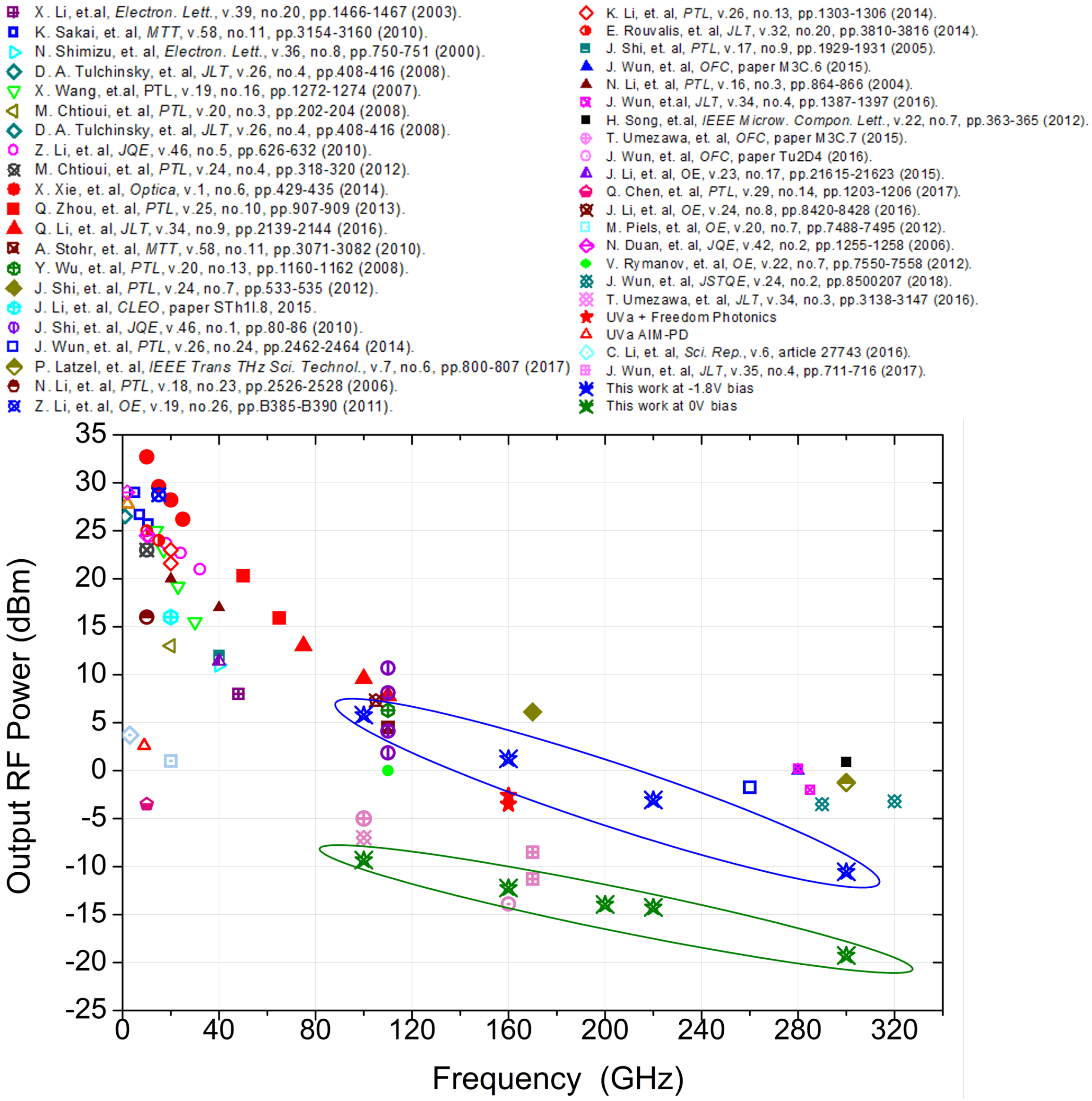

Figure 9.16: Results of new generation PD saturation power compared to the literature.

Chapter 10

Future Work

10.1 Emitter Power Transfer

We have investigated complex conjugate impedance matching between antenna and PD. It is well-known that impedance matching for broadband devices, can limit device performance by creating a narrow band of matching. Through simulation during our previous emitter work in Section 2.3.2, we found that small fF changes in parasitic capacitance, introduced from flip-chip bonding and the inductive affects of the air-bridge, can greatly affect the broadband impedance of the device, making broadband impedance matching difficult to achieve. Thus, I fabricated monolithically integrated photodiode-antenna emitters using the new fabrication procedure, as shown for a 05-µm PD with 200 GHz dipole antenna in Figure 10.2. The antennas fabricated were on the edge of the chip, where uniformity in the SU8 planarization was difficult to achieve due to the square shape of the chips, ultimately leading to an over-etch of the SU8 and a leaky devices; however, the IV data from probing the bias lines, showed a working device nonetheless as seen in Figure 10.1. In addition to the reduction of parasitics in the devices, the stray capacitance was calculated within 0.5 fF of what was measured. This means that we now have the ability to fabricate emitters within a tight tolerance, which can lead to impedance matching realizations, and improvements in overall emitter performance. With a fabrication run prioritizing the antenna structures in the center of the chip, these monolithic emitters should be ready to continue the group's work in the wireless realm.

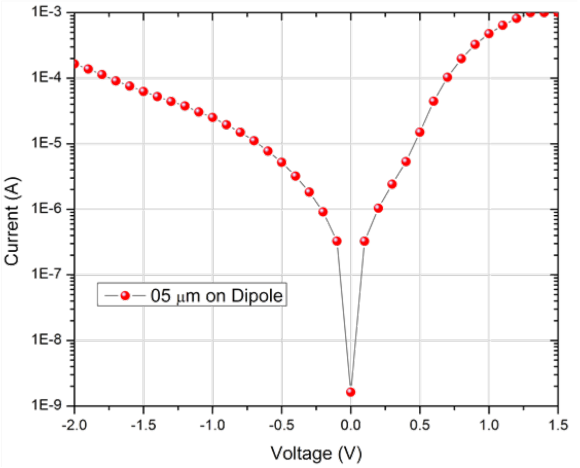

Figure 10.1: IV curve from probing of DC bias lines of 05-µm PD monolithically integrated with dipole antenna.

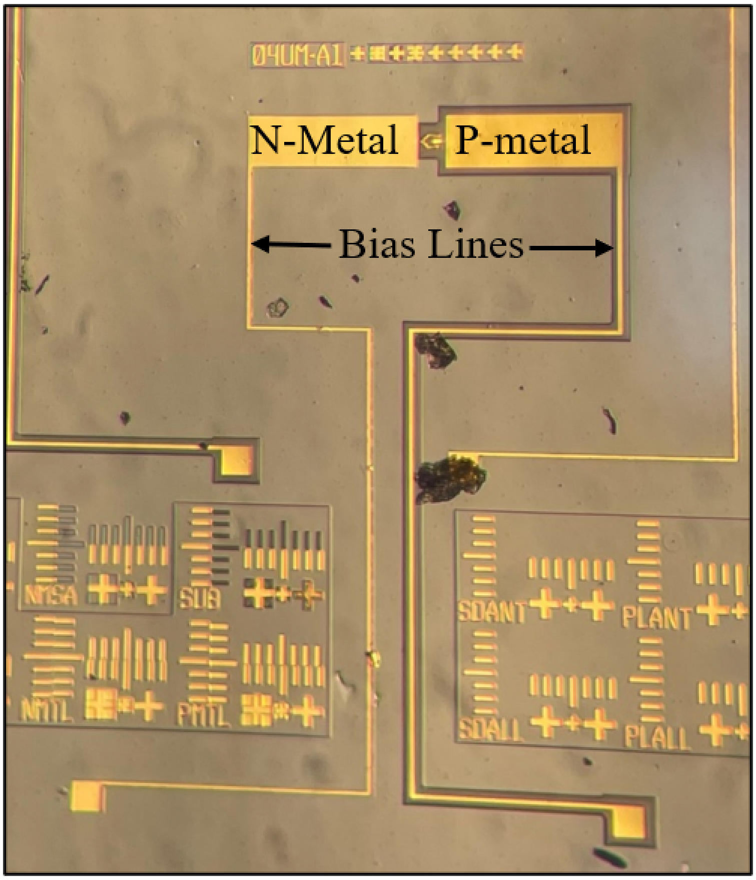

Figure 10.2: Microscope image of fabricated 05-µm PD monolithically integrated with dipole antenna.

Chapter 11

Publications

11.1 Journal Articles

1. Bryan T. Bosworth, Nick R. Jungwirth, Kassiopeia Smith, Jerome Cheron, Franklyn Quinlan, Madison Woodson, Jesse Morgan, Andreas Beling, Ari Feldman, Dylan Williams, Nathan D. Orloff, and Christian J. Long , ”Electro-optically derived millimeter-wave sources with phase and amplitude control”, Appl. Phys. Lett. 119, 151106 (2021).
2. Lischke, S., Peczek, A., Morgan, J.S. et al. Ultra-fast germanium photodiode with 3-dB bandwidth of 265 GHz. Nat. Photon. 15, 925–931 (2021).
3. X. Shen, J. Morgan, et al., ”High-Power V-Band-to-G-Band Photonically Driven Electromagnetic Emitters,” in IEEE Transactions on Microwave Theory and Techniques, vol. 69, no. 2, pp. 1474-1487, Feb. 2021.
4. Wang, B., Morgan, J.S., Sun, K. et al. Towards high-power, high-coherence, integrated photonic mmWave platform with microcavity solitons. Light Sci Appl 10, 4 (2021).
5. Jesse Morgan, Meredith Hutchinson, Tegan Wilson, and Jonathan M. Nichols, ”Linear transfer function estimation using the photodiode impulse response,” Opt. Lett. 44, 5001-5004 (2019).
6. J. Zang, J.S. Morgan, X. Xie, K. Sun., Q. Li, A. Beling and J. Campbell, “InP/InGaAs Photovaractor,” in Journal of Lightwave Technology, vol. 36, no. 9, pp. 1661-1665, May, 01 2018.

7. Keye Sun, Daehwan Jung, Chen Shang, Alan Liu, Jesse Morgan, Jizhao Zang, Qinglong Li, Jonathan Klamkin, John E. Bowers, and Andreas Beling, ”Low dark current III–V on silicon photodiodes by heteroepitaxy,” Opt. Express 26, 13605-13613 (2018).

11.2 Conference Proceedings

1. J. Zang, J. Morgan, A. Beling, and S. Papp, “Broadband Optoelectronic Mixer for Optical Frequency Division and Synthesis,” Conference on Lasers and Electro-Optics (CLEO, 2022), accepted 11 March 2022.
2. S. Lischke et al., ”Very High-Speed Waveguide Integrated Germanium Photo Detectors,” 2021 European Conference on Optical Communication (ECOC), 2021, pp. 1-4.
3. B. Wang, J. S. Morgan, et al., ”Generation of high-power, high-coherence millimeter-wave using microresonator solitons,” Conference on Lasers and Electro-Optics (CLEO, 2021), paper SW4A.2.
4. J. Zang, T. C. Briles, J. S. Morgan, A. Beling and S. Papp, ”Millimeter Wave Frequency Synthesizer Based on Integrated Photonics,” 2020 International Topical Meeting on Microwave Photonics (MWP), 2020, pp. 101-104.
5. J. Morgan et al., ”High-Power Millimeter-Wave Generation using Microresonator Solitons,” 2020 IEEE Photonics Conference (IPC), 2020, pp. 1-2.
6. B. Wang, J. S. Morgan, et al., ”High-power, high-coherence mmWave generation based on integrated microresonator solitons,” in Frontiers in Optics / Laser Science, OSA Technical Digest (Optical Society of America, 2020), paper FW4D.5 (14 September 2020).
7. J. Zang, T. C. Briles, J. S. Morgan, A. Beling and S. Papp, ”Wide-Band Millimeter-Wave Synthesizer by Integrated Microcomb Photomixing,” 2020 Conference on Lasers and Electro-Optics (CLEO), 2020, pp. 1-2, 10 September 2020.
8. M. Woodson, S. Estrella, K. Hay, R. Stahl, H. Garrett, K. Sun, J. Morgan, A. Beling, D. Renner, M. Mashanovitch, ”High-power balanced uni-traveling-carrier photodiodes for high-frequency RF photonic links (Conference Presentation),” Proc. SPIE 11279, Terahertz, RF, Millimeter, and Submillimeter-Wave Technology and Applications XIII, 112791 (10 March 2020).

9. J. Zang, T. C. Briles, J. S. Morgan, S. Yu, A. Beling and S. Papp, ”Soliton Microcomb-Based Millimeter-Wave Synthesizer,” 2019 IEEE Avionics and Vehicle Fiber-Optics and Photonics Conference (AVFOP), 2019, pp. 1-2.

10. S. Dülme M. Grzeslo, J. Morgan, et al., ”300 GHz Photonic Self-Mixing Imaging-System with vertical illuminated Triple-Transit-Region Photodiode Terahertz Emitters,” 2019 International Topical Meeting on Microwave Photonics (MWP), 2019, pp. 1-4.

11. X. Shen, R. Constanzo, J. Morgan, et al., ”High-Power W-band to G-band Photonically-Driven Electromagnetic Emitter with 8.8 dBm EIRP,” 2019 International Topical Meeting on Microwave Photonics (MWP), 2019, pp. 1-4.

12. A. Beling, T. Tzu, J. Gao, J.S. Morgan, et al., ”High-Speed Integrated Photodiodes,” 2019 24th OptoElectronics and Communications Conference (OECC) and 2019 International Conference on Photonics in Switching and Computing (PSC), 2019, pp. 1-3.

13. B. Tossoun, J. Morgan, and A. Beling, ”Ultra-Low Capacitance, High-Speed Integrated Waveguide Photodiodes on InP,” in OSA Advanced Photonics Congress (AP) 2019 (IPR, Networks, NOMA, SPPCom, PVLED), OSA Technical Digest (Optical Society of America, 2019), paper IT3A.6.

14. J. Zang, T. C. Briles, J. S. Morgan, S. Yu, A. Beling, and S. Papp, ”Millimeter-wave Synthesizer Based on Microresonator Soliton Dual-comb Photomixing,” in OSA Advanced Photonics Congress (AP) 2019 (IPR, Networks, NOMA, SPPCom, PVLED), OSA Technical Digest (Optical Society of America, 2019), paper IT1A.4.

15. M. Woodson, et al., ”Photodetection at or below 1 micron wavelengths (Conference Presentation),” Proc. SPIE 10912, Physics and Simulation of Optoelectronic Devices XXVII, 1091210 (08 March 2019).

16. M. Woodson, et al., ”High-power high-bandwidth unitraveling-carrier photodiodes for high-frequency RF photonic links (Conference Presentation),” Proc. SPIE 10917, Terahertz, RF, Millimeter, and Submillimeter-Wave Technology and Applications XII, 109171J (5 March 2019).

17. J.S. Morgan, et al, ”Zero-bias Photovaractor with 60 GHz Resonant Network for Optically Modulated Scatterer (OMS) Application,” in Conference on Lasers and Electro-Optics (CLEO), OSA Technical Digest (Optical Society of America, 2018), paper STu3B.5.
18. J. S. Morgan et al., ”High-Power Flip-Chip Bonded Modified Uni-Traveling Carrier Photodiodes with -2.6 dBm RF Output Power at 160 GHz,” 2018 IEEE Photonics Conference (IPC), Reston, VA, 2018, pp. 1-2.
19. J. Zang, J. Morgan, A. Beling and J. C. Campbell, ”Optically Controlled Microwave Attenuator Based on InP/InGaAs Photovaractor,” 2018 IEEE Photonics Conference (IPC), Reston, VA, 2018, pp. 1-2.
20. A. Beling, J.S. Morgan, K. Sun and Q. Yu, ”High Power Integrated 100 GHz Photodetectors,” 2018 International Topical Meeting on Microwave Photonics (MWP), Toulouse, 2018, pp. 1-4.

Bibliography

[1] Andreas Beling, Ta Ching Tzu, Junyi Gao, Jesse S. Morgan, Keye Sun, Nan Ye, Bassem Tossoun, Fengxin Yu, and Qianhuan Yu. High-speed integrated photodiodes. In *2019 24th OptoElectronics and Communications Conference (OECC) and 2019 International Conference on Photonics in Switching and Computing (PSC)*, pages 1–3, 2019.

[2] Vincent J. Urick, Jason D. McKinney, and Keith J. Williams. *FUNDAMENTALS OF MICROWAVE PHOTONICS*, chapter 10, pages 383–445. John Wiley & Sons, Ltd, 2015.

[3] Ken B. Cooper, Robert J. Dengler, Nuria Llombart, Tomas Bryllert, Goutam Chattopadhyay, Erich Schlecht, John Gill, Choonsup Lee, Anders Skalare, Imran Mehdi, and Peter H. Siegel. Penetrating 3-d imaging at 4- and 25-m range using a submillimeter-wave radar. *IEEE Transactions on Microwave Theory and Techniques*, 56(12):2771–2778, 2008.

[4] Thomas Kleine-Ostmann and Tadao Nagatsuma. A review on terahertz communications research. *Journal of Infrared, Millimeter, and Terahertz Waves*, 32(2):143–171, Feb 2011.

[5] S. Koenig, D. Lopez-Diaz, J. Antes, F. Boes, R. Henneberger, A. Leuther, A. Tessmann, R. Schmogrow, D. Hillerkuss, R. Palmer, T. Zwick, C. Koos, W. Freude, O. Ambacher, J. Leuthold, and I. Kallfass. Wireless sub-thz communication system with high data rate. *Nature Photonics*, 7(12):977–981, Dec 2013.

[6] Beichen Wang, Jesse S. Morgan, Keye Sun, Mandana Jahanbozorgi, Zijiao Yang, Madison Woodson, Steven Estrella, Andreas Beling, and Xu Yi. Towards high-power, high-coherence, integrated photonic mmwave platform with microcavity solitons. *Light: Science & Applications*, 10(1):4, Jan 2021.

[7] A. Beling, J. Campbell, K. Li, Q. Li, Y. Wang, M. Woodson, X. Xie, and Z. Yang. High-power photodiodes for analog applications. *IEICE TRANSACTIONS on Electronics*, E98-C(8):764–768, Aug 2015.

[8] Kazutoshi Kato, Hata Susumu, Kenji Kawano, and Atsuo Kozen. Design of ultrawide-band, high-sensitivity p-i-n protodetectors. *IEICE Transactions on Electronics*, pages 214–221, 1993.

[9] Xiaojun Xie, Qiugui Zhou, Kejia Li, Yang Shen, Qinglong Li, Zhanyu Yang, Andreas Beling, and Joe C. Campbell. Improved power conversion efficiency in high-performance photodiodes by flip-chip bonding on diamond. *Optica*, 1(6):429–435, Dec 2014.

[10] Vincent Jude Urick, Keith J Williams, and Jason D McKinney. *Fundamentals of microwave photonics*. John Wiley & Sons, 2015.

[11] Andreas Beling, Xiaojun Xie, and Joe C. Campbell. High-power, high-linearity photodiodes. *Optica*, 3(3):328–338, Mar 2016.

[12] Efthymios Rouvalis, Cyril C. Renaud, David G. Moodie, Michael J. Robertson, and Alwyn J. Seeds. Continuous wave terahertz generation from ultra-fast inp-based photodiodes. *IEEE Transactions on Microwave Theory and Techniques*, 60(3):509–517, 2012.

[13] Jhih-Min Wun, Cheng-Hung Lai, Nan-Wei Chen, John E. Bowers, and Jin-Wei Shi. Flip-chip bonding packaged thz photodiode with broadband high-power performance. *IEEE Photonics Technology Letters*, 26(24):2462–2464, 2014.

[14] Tadao Ishibashi and Hiroshi Ito. Uni-traveling-carrier photodiodes. *Journal of Applied Physics*, 127(3):031101, 2020.

[15] Dong-Hwan Jun, Jae-Hyung Jang, Ilesanmi Adesida, and Jong-In Song. Improved efficiency-bandwidth product of modified uni-traveling carrier photodiode structures using an undoped photo-absorption layer. *Japanese Journal of Applied Physics*, 45(4B):3475–3478, apr 2006.

[16] N. Shimizu, N. Watanabe, T. Furuta, and T. Ishibashi. Inp-ingaas uni-traveling-carrier photodiode with improved 3-db bandwidth of over 150 ghz. *IEEE Photonics Technology Letters*, 10(3):412–414, 1998.

[17] Freedom Photonics LLC. 65 ghz high power photodiodes.

[18] Xiaochuan Shen, Jesse Morgan, Robert Costanzo, Keye Sun, Madison Woodson, Steven B. Estrella, Andreas Beling, and Steven M. Bowers. High-power v-band-to-g-band photonically driven electromagnetic emitters. *IEEE Transactions on Microwave Theory and Techniques*, 69(2):1474–1487, 2021.

[19] Jesse S. Morgan, Keye Sun, Qinglong Li, Steven Estrella, Maddy Woodson, Kenneth Hay, Milan Mashanovitch, and Andreas Beling. High-power flip-chip bonded modified uni-traveling carrier photodiodes with -2.6 dbm rf output power at 160 ghz. In *2018 IEEE Photonics Conference (IPC)*, pages 1–2, 2018.

[20] Jizhao Zang, Travis C. Briles, Jesse S. Morgan, Su-Peng Yu, Andreas Beling, and Scott Papp. Soliton microcomb-based millimeter-wave synthesizer. In *2019 IEEE Avionics and Vehicle Fiber-Optics and Photonics Conference (AVFOP)*, pages 1–2, 2019.

[21] Jizhao Zang, Travis C. Briles, Jesse S. Morgan, Su-Peng Yu, Andreas Beling, and Scott Papp. Millimeter-wave synthesizer based on microresonator soliton dual-comb photomixing. In *OSA Advanced Photonics Congress (AP) 2019 (IPR, Networks, NOMA, SPPCom, PVLED)*, page IT1A.4. Optica Publishing Group, 2019.

[22] Michele Natrella, Chin-Pang Liu, Chris Graham, Frederic van Dijk, Huiyun Liu, Cyril C. Renaud, and Alwyn J. Seeds. Accurate equivalent circuit model for millimetre-wave utc photodiodes. *Opt. Express*, 24(5):4698–4713, Mar 2016.

[23] W.H. Haydl. On the use of vias in conductor-backed coplanar circuits. *IEEE Transactions on Microwave Theory and Techniques*, 50(6):1571–1577, 2002.

[24] Tadao Nagatsuma, Guillaume Ducournau, and Cyril C. Renaud. Advances in terahertz communications accelerated by photonics. *Nature Photonics*, 10(6):371–379, Jun 2016.

[25] John Federici and Lothar Moeller. Review of terahertz and subterahertz wireless communications. *Journal of Applied Physics*, 107(11):111101, 2010.

[26] Jeffrey G. Andrews, Stefano Buzzi, Wan Choi, Stephen V. Hanly, Angel Lozano, Anthony C. K. Soong, and Jianzhong Charlie Zhang. What will 5g be? *IEEE Journal on Selected Areas in Communications*, 32(6):1065–1082, 2014.

[27] M.N. Afsar, I.I. Tkachov, and K.N. Kocharyan. A novel w-band spectrometer for dielectric measurements. *IEEE Transactions on Microwave Theory and Techniques*, 48(12):2637–2643, 2000.

[28] Sebastian Dülme, Peng Lu, Andreas Beling, Andreas Stöhr, M. Grzeslo, Jesse S. Morgan, Matthias Steeg, Mason Lange, Jonas Tebart, Nils Schrinski, Isra'a Mohammad, and Tom Neerfeld. 300 ghz photonic self-mixing imaging-system with vertical illuminated triple-transit-region photodiode terahertz emitters. *2019 International Topical Meeting on Microwave Photonics (MWP)*, pages 1–4, 2019.

[29] D.M. Sheen, D.L. McMakin, and T.E. Hall. Three-dimensional millimeter-wave imaging for concealed weapon detection. *IEEE Transactions on Microwave Theory and Techniques*, 49(9):1581–1592, 2001.

[30] Giovanni Serafino, Filippo Scotti, Leonardo Lembo, Bilal Hussain, Claudio Porzi, Antonio Malacarne, Salvatore Maresca, Daniel Onori, Paolo Ghelfi, and Antonella Bogoni. Toward a new generation of radar systems based on microwave photonic technologies. *Journal of Lightwave Technology*, 37(2):643–650, 2019.

[31] Ken B. Cooper and Goutam Chattopadhyay. Submillimeter-wave radar: Solid-state system design and applications. *IEEE Microwave Magazine*, 15(7):51–67, 2014.

[32] Xiang Yang, Xiang Zhao, Ke Yang, Yueping Liu, Yu Liu, Weiling Fu, and Yang Luo. Biomedical applications of terahertz spectroscopy and imaging. *Trends in Biotechnology*, 34(10):810–824, 2016.

[33] M. Mahdi Assefzadeh and Aydin Babakhani. Broadband oscillator-free thz pulse generation and radiation based on direct digital-to-impulse architecture. *IEEE Journal of Solid-State Circuits*, 52(11):2905–2919, 2017.

[34] Sam Razavian and Aydin Babakhani. A thz pulse radiator based on pin diode reverse recovery. In *2019 IEEE BiCMOS and Compound semiconductor Integrated Circuits and Technology Symposium (BCICTS)*, pages 1–4, 2019.

[35] Akihiko Hirata, Mitsuru Harada, and Tadao Nagatsuma. 120-ghz wireless link using photonic techniques for generation, modulation, and emission of millimeter-wave signals. *J. Lightwave Technol.*, 21(10):2145, Oct 2003.

[36] Nan-Wei Chen, Jin-Wei Shi, Hsuan-Ju Tsai, Jhih-Min Wun, Fong-Ming Kuo, Jeffery Hesler, Thomas W. Crowe, and John E. Bowers. Design and demonstration of ultra-fast w-band photonic transmitter-mixer and detectors for 25 gbits/sec error-free wireless linking. *Opt. Express*, 20(19):21223–21234, Sep 2012.

[37] E. Lacombe, C. Belem-Goncalves, C. Luxey, F. Gianesello, C. Durand, D. Gloria, and G. Ducournau. 300 ghz ook transmitter integrated in advanced silicon photonics technology and achieving 20 gb/s. In *2018 IEEE Radio Frequency Integrated Circuits Symposium (RFIC)*, pages 356–359, 2018.

[38] Peter Offermans, Lei Zhang, Peter De Heyn, Sofie Janssen, Sadhishkumar Balakrishnan, Xavier Rottenberg, and Joris van Campenhout. Continuous wave generation up to 1.3 thz using antenna-coupled silicon-integrated ge photodiodes. In *2018 11th UK-Europe-China Workshop on Millimeter Waves and Terahertz Technologies (UCMMT)*, volume 1, pages 1–2, 2018.

[39] Keye Sun, Jesse Moody, Qinglong Li, Steven M. Bowers, and Andreas Beling. High power integrated photonic w-band emitter. *IEEE Transactions on Microwave Theory and Techniques*, 66(3):1668–1677, 2018.

[40] H. Ito, T. Furuta, Y. Hirota, T. Ishibashi, A. Hirata, T. Nagatsuma, H. Matsuo, T. Noguchi, and M. Ishiguro. Photonic millimetre-wave emission at 300 GHz using an antenna-integrated uni-travelling-carrier photodiode. *Electronics Letters*, 38:989–990, September 2002.

[41] David A. B. Miller. Attojoule optoelectronics for low-energy information processing and communications. *Journal of Lightwave Technology*, 35(3):346–396, 2017.

[42] Kengo Nozaki, Shinji Matsuo, Takuro Fujii, Koji Takeda, Masaaki Ono, Abdul Shakoor, Eiichi Kuramochi, and Masaya Notomi. Photonic-crystal nano-photodetector with ultrasmall capacitance for on-chip light-to-voltage conversion without an amplifier. *Optica*, 3(5):483–492, May 2016.

[43] Bassem Tossoun, Jesse Morgan, and Andreas Beling. Ultra-low capacitance, high-speed integrated waveguide photodiodes on inp. In *OSA Advanced Photonics Congress (AP) 2019 (IPR, Networks, NOMA, SPPCom, PVLED)*, page IT3A.6. Optica Publishing Group, 2019.

[44] Qinglong Li, Keye Sun, Kejia Li, Qianhuan Yu, Patrick Runge, Willi Ebert, Andreas Beling, and Joe C. Campbell. High-power evanescently coupled waveguide mutc photodiode with >105-ghz bandwidth. *J. Lightwave Technol.*, 35(21):4752–4757, Nov 2017.

[45] H. Ito, T. Furuta, S. Kodama, and T. Ishibashi. Zero-bias high-speed and high-output-voltage operation of cascade-twin unitravelling-carrier photodiode. *Electronics Letters*, 36:2034 – 2036, 12 2000.

[46] Tobias Herr, Victor Brasch, John D Jost, Christine Y Wang, Nikita M Kondratiev, Michael L Gorodetsky, and Tobias J Kippenberg. Temporal solitons in optical microresonators. *Nature Photonics*, 8(2):145, 2014.

[47] Xu Yi, Qi-Fan Yang, Ki Youl Yang, Myoung-Gyun Suh, and Kerry Vahala. Soliton frequency comb at microwave rates in a high-Q silica microresonator. *Optica*, 2(12):1078–1085, 2015.

[48] Victor Brasch, Michael Geiselmann, Tobias Herr, Grigoriy Lihachev, Martin HP Pfeiffer, Michael L Gorodetsky, and Tobias J Kippenberg. Photonic chip–based optical frequency comb using soliton cherenkov radiation. *Science*, 351(6271):357–360, 2016.

[49] Zheng Gong, Alexander Bruch, Mohan Shen, Xiang Guo, Hojoong Jung, Linran Fan, Xianwen Liu, Liang Zhang, Junxi Wang, Jinmin Li, et al. High-fidelity cavity soliton generation in crystalline AlN micro-ring resonators. *Optics letters*, 43(18):4366–4369, 2018.

[50] Alexander L Gaeta, Michal Lipson, and Tobias J Kippenberg. Photonic-chip-based frequency combs. *Nature Photonics*, 13(3):158–169, 2019.

[51] Yang He, Qi-Fan Yang, Jingwei Ling, Rui Luo, Hanxiao Liang, Mingxiao Li, Boqiang Shen, Heming Wang, Kerry Vahala, and Qiang Lin. Self-starting bi-chromatic $LiNbO_3$ soliton microcomb. *Optica*, 6(9):1138–1144, 2019.

[52] Tobias J Kippenberg, Alexander L Gaeta, Michal Lipson, and Michael L Gorodetsky. Dissipative Kerr solitons in optical microresonators. *Science*, 361(6402):eaan8083, 2018.

[53] Daryl T Spencer, Tara Drake, Travis C Briles, Jordan Stone, Laura C Sinclair, Connor Fredrick, Qing Li, Daron Westly, B Robert Ilic, Aaron Bluestone, et al. An optical-frequency synthesizer using integrated photonics. *Nature*, 557(7703):81–85, 2018.

[54] Pablo Marin-Palomo, Juned N Kemal, Maxim Karpov, Arne Kordts, Joerg Pfeifle, Martin HP Pfeiffer, Philipp Trocha, Stefan Wolf, Victor Brasch, Miles H Anderson, et al. Microresonator-based solitons for massively parallel coherent optical communications. *Nature*, 546(7657):274–279, 2017.

[55] Myoung-Gyun Suh, Qi-Fan Yang, Ki Youl Yang, Xu Yi, and Kerry J Vahala. Microresonator soliton dual-comb spectroscopy. *Science*, 354(6312):600–603, 2016.

[56] Avik Dutt, Chaitanya Joshi, Xingchen Ji, Jaime Cardenas, Yoshitomo Okawachi, Kevin Luke, Alexander L Gaeta, and Michal Lipson. On-chip dual-comb source for spectroscopy. *Science advances*, 4(3):e1701858, 2018.

[57] P Del'Haye, A Schliesser, O Arcizet, T Wilken, R Holzwarth, and TJ Kippenberg. Optical frequency comb generation from a monolithic microresonator. *Nature*, 450(7173):1214–1217, 2007.

[58] Myoung-Gyun Suh and Kerry Vahala. Gigahertz-repetition-rate soliton microcombs. *Optica*, 5(1):65–66, 2018.

[59] Qing Li, Travis C Briles, Daron A Westly, Tara E Drake, Jordan R Stone, B Robert Ilic, Scott A Diddams, Scott B Papp, and Kartik Srinivasan. Stably accessing octave-spanning microresonator frequency combs in the soliton regime. *Optica*, 4(2):193–203, 2017.

[60] F-M Kuo, J-W Shi, H-C Chiang, H-P Chuang, H-K Chiou, C-L Pan, N-W Chen, H-J Tsai, and C-B Huang. Spectral power enhancement in a 100 GHz photonic millimeter-wave generator enabled by spectral line-by-line pulse shaping. *IEEE Photonics Journal*, 2(5):719–727, 2010.

[61] W Liang, D Eliyahu, VS Ilchenko, AA Savchenkov, AB Matsko, D Seidel, and L Maleki. High spectral purity Kerr frequency comb radio frequency photonic oscillator. *Nat. Commun.*, 6:7957, 2015.

[62] Xu Yi, Qi-Fan Yang, Xueyue Zhang, Ki Youl Yang, Xinbai Li, and Kerry Vahala. Single-mode dispersive waves and soliton microcomb dynamics. *Nature communications*, 8(1):1–9, 2017.

[63] Junqiu Liu, Erwan Lucas, Arslan S Raja, Jijun He, Johann Riemensberger, Rui Ning Wang, Maxim Karpov, Hairun Guo, Romain Bouchand, and Tobias J Kippenberg. Photonic microwave generation in the X-and K-band using integrated soliton microcombs. *Nature Photonics*, pages 1–6, 2020.

[64] Brian Stern, Xingchen Ji, Yoshitomo Okawachi, Alexander L Gaeta, and Michal Lipson. Battery-operated integrated frequency comb generator. *Nature*, 562(7727):401–405, 2018.

[65] Chao Xiang, Warren Jin, Joel Guo, Jonathan D Peters, MJ Kennedy, Jennifer Selvidge, Paul A Morton, and John E Bowers. Narrow-linewidth III-V/Si/Si_3N_4 laser using multilayer heterogeneous integration. *Optica*, 7(1):20–21, 2020.

[66] Camiel Op de Beeck, Bahawal Haq, Lukas Elsinger, Agnieszka Gocalinska, Emanuele Pelucchi, Brian Corbett, Günther Roelkens, and Bart Kuyken. Heterogeneous III-V on silicon nitride amplifiers and lasers via microtransfer printing. *Optica*, 7(5):386–393, 2020.

[67] Qianhuan Yu, Junyi Gao, Nan Ye, Baiheng Chen, Keye Sun, Linli Xie, Kartik Srinivasan, Michael Zervas, Gabriele Navickaite, Michael Geiselmann, et al. Heterogeneous photodiodes on silicon nitride waveguides. *Optics Express*, 28(10):14824–14830, 2020.

[68] Jhih-Min Wun, Hao-Yun Liu, Cheng-Hung Lai, Yi-Shiun Chen, Shang-Da Yang, Ci-Ling Pan, John E Bowers, Chen-Bin Huang, and Jin-Wei Shi. Photonic high-power 160-GHz signal generation by using ultrafast photodiode and a high-repetition-rate femtosecond optical pulse train generator. *IEEE Journal of Selected Topics in Quantum Electronics*, 20(6):10–16, 2014.

[69] Shuangyou Zhang, Jonathan M Silver, Xiaobang Shang, Leonardo Del Bino, Nick M Ridler, and Pascal Del'Haye. Terahertz wave generation using a soliton microcomb. *Optics Express*, 27(24):35257–35266, 2019.

[70] Jizhao Zang, Travis C. Briles, Jesse S. Morgan, Andreas Beling, and Scott Papp. Wide-band millimeter-wave synthesizer by integrated microcomb photomixing. In *Conference on Lasers and Electro-Optics (CLEO) 2020*. Optical Society of America, 2020.

[71] Tomohiro Tetsumoto, Fumiya Ayano, Mark Yeo, Julian Webber, Tadao Nagatsuma, and Antoine Rolland. 300 ghz wave generation based on a kerr microresonator frequency comb stabilized to a low noise microwave reference. *Optics Letters*, 45(16):4377–4380, 2020.

[72] Jesse Morgan, Beichen Wang, Keye Sun, Mandana Jahanbozorgi, Zijiao Yang, Madison Woodson, Steven Estrella, Xu Yi, and Andreas Beling. High-power millimeter-wave generation using microresonator solitons. In *2020 IEEE Photonics Conference (IPC)*, pages 1–2, 2020.

[73] Xiaojun Xie, Kejia Li, Yang Shen, Qinglong Li, Jizhao Zang, Andreas Beling, and Joe C. Campbell. Photonic generation of high-power pulsed microwave signals. *Journal of Lightwave Technology*, 33(18):3808–3814, 2015.

[74] Wenle Weng, Aleksandra Kaszubowska-Anandarajah, Junqiu Liu, Prince M Anandarajah, and Tobias J Kippenberg. Frequency division using a soliton-injected semiconductor gain-switched frequency comb. *Science Advances*, 6(39):eaba2807, 2020.

[75] Erwan Lucas, Pierre Brochard, Romain Bouchand, Stéphane Schilt, Thomas Südmeyer, and Tobias J Kippenberg. Ultralow-noise photonic microwave synthesis using a soliton microcomb-based transfer oscillator. *Nature Communications*, 11(1):1–8, 2020.

[76] Nicolas Volet, Xu Yi, Qi-Fan Yang, Eric J Stanton, Paul A Morton, Ki Youl Yang, Kerry J Vahala, and John E Bowers. Micro-resonator soliton generated directly with a diode laser. *Laser & Photonics Reviews*, 12(5):1700307, 2018.

[77] Beichen Wang, Zijiao Yang, Xiaobao Zhang, and Xu Yi. Vernier frequency division with dual-microresonator solitons. *Nature Communications*, 11(3975), 2020.

[78] J.J. Lee, E.M. Ferren, D.P. Woollen, and K.M. Lee. Near-field probe used as a diagnostic tool to locate defective elements in an array antenna. *IEEE Transactions on Antennas and Propagation*, 36(6):884–889, 1988.

[79] J. Brown and E.V. Jull. The prediction of aerial radiation patterns from near-field measurements. *Proceedings of the IEE - Part B: Electronic and Communication Engineering*, 108(42):635–644, 1961.

[80] A. Neuber, J. Dickens, D. Hemmert, H. Krompholz, L.L. Hatfield, and M. Kristiansen. Window breakdown caused by high-power microwaves. *IEEE Transactions on Plasma Science*, 26(3):296–303, 1998.

[81] Jean-Charles Bolomey and Fred E. Gardiol. Engineering applications of the modulated scatterer technique. 2001.

[82] A. M. Vural and D. K. Cheng. A light-modulated scattering technique for diffraction field measurements. *Journal of Research of the National Bureau of Standards, Section D: Radio Science*, page 355, 1964.

[83] Robert C. Daniels and Robert W. Heath. 60 ghz wireless communications: Emerging requirements and design recommendations. *IEEE Vehicular Technology Magazine*, 2(3):41–50, 2007.

[84] Jesse S. Morgan, Jizhao Zang, Keye Sun, Bassem Tossoun, Joe C. Campbell, and Andreas Beling. Zero-bias photovaractor with 60 ghz resonant network for optically modulated scatterer (oms) application. In *Conference on Lasers and Electro-Optics*, page STu3B.5. Optica Publishing Group, 2018.

[85] Jizhao Zang, Jesse S. Morgan, Xiaojun Xie, Keye Sun, Qinglong Li, Andreas Beling, and Joe C. Campbell. Inp/ingaas photovaractor. *J. Lightwave Technol.*, 36(9):1661–1665, May 2018.

[86] Hamidreza Memarzadeh-Tehran, Jean-Jacques Laurin, and Raman Kashyap. Optically modulated probe for precision near-field measurements. *IEEE Transactions on Instrumentation and Measurement*, 59(10):2755–2762, 2010.

[87] Jizhao Zang, Zhanyu Yang, Xiaojun Xie, Min Ren, Yang Shen, Zack Carson, Olivier Pfister, Andreas Beling, and Joe C. Campbell. High quantum efficiency uni-traveling-carrier photodiode. *IEEE Photonics Technology Letters*, 29(3):302–305, 2017.

[88] S. Lischke, A. Peczek, J. S. Morgan, K. Sun, D. Steckler, Y. Yamamoto, F. Korndörfer, C. Mai, S. Marschmeyer, M. Fraschke, A. Krüger, A. Beling, and L. Zimmermann. Ultra-fast germanium photodiode with 3-db bandwidth of 265 ghz. *Nature Photonics*, 15(12):925–931, Dec 2021.

[89] Molly Piels and John E. Bowers. Si/ge uni-traveling carrier photodetector. *Opt. Express*, 20(7):7488–7495, Mar 2012.

[90] Han-Ki Kim, Tae-Yeon Seong, Ilesanmi Adesida, Chak Wah Tang, and Kei May Lau. Low-resistance pt/pd/au ohmic contacts to p-type algan. *Applied Physics Letters*, 84(10):1710–1712, 2004.

[91] Jun Liu, Zhiping Yu, and Lingling Sun. A broadband model over 1–220 ghz for gsg pad structures in rf cmos. *IEEE Electron Device Letters*, 35(7):696–698, 2014.

[92] Kristian Hagsted Rasmussen, Stephan Sylvest Keller, Flemming Jensen, A. M. Jorgensen, and Ole Hansen. Su-8 etching in inductively coupled oxygen plasma. *Microelectronic Engineering*, 112:35–40, 2013.

[93] Naofumi Shimizu, Noriyuki Watanabe, Tomofumi Furuta, and Tadao Ishibashi. Improved response of uni-traveling-carrier photodiodes by carrier injection. *Japanese Journal of Applied Physics*, 37(Part 1, No. 3B):1424–1426, mar 1998.

Appendix A

Planar MUTC Device Fabrication

1. Step 01 P-Mesa
    - (a) P-Metal Evaporation
        - i. Chip clean/preparation
            - A. Spray bottle clean acetone, IPA; DI rinse in beaker; nitrogen dry
            - B. Hot plate bake 4 minutes @ 160 C
            - C. O2 plasma: RF 150-200 W; O2 50-100 sccm; 5-20 min
        - ii. E-Beam metal evaporation
            - A. Ti 300-Å @ 1.0- Å/sec
            - B. Pt 500- Å @ 1.0- Å/sec
            - C. Au 2000- Å @ 1.0- Å/sec (suggest x2)
            - D. Ti 200- Å @ 1.0- Å/sec
    - (b) SiO_2 Deposition
        - i. Chip clean/preparation
            - A. Spray bottle clean acetone, IPA; DI rinse in beaker; nitrogen dry
            - B. Hot plate bake 4 minutes @ 160 C
            - C. O2 plasma: RF 150-200 W; O2 50-100 sccm; 5-20 min
        - ii. SiO_2 PECVD deposition
            - A. SiO_2 540 nm (thickness critical when doing thicker p-metal)
    - (c) P-Mesa Lithography

    i. Chip clean/preparation
        A. Spray bottle clean acetone, IPA; DI rinse in beaker; nitrogen dry
        B. Hot plate bake 4 minutes @ 160 C
        C. O2 plasma: RF 150-200 W; O2 50-100 sccm; 5-20 min
    ii. Spin resist
        A. HMDS precursor: 30 seconds @ 3000 rpm @ 3krpm/sec ramp
        B. (Critical) Hot plate bake: 2 minutes @ 90 C
        C. Spin AZ5214: 40 seconds @ 3000 rpm @ 3 krpm/sec ramp ($\sim$1.87 um)
        D. Edge-bead removal & backside cleaning with cotton swab + acetone
        E. Soft bake (hot plate): 2 minutes @ 100 C
    iii. Exposure
        A. Contact: hard or vacuum
        B. Vacuum contact: seal pressure $>$ 12 kPa; check for WEC pressure specific to chuck
        C. Alignment: ideally along crystal axis (parallel with straight edge)
        D. Exposure @ 365 nm & 10 mW: dose $\sim$170 mJ/cm, $\sim$8 seconds
        E. Exposure @ 320 nm & 7 mW: $\sim$40 seconds
        F. Exposure @ 320 nm & 10 mW: $\sim$30 seconds
    iv. Development
        A. AZ300 MIF: 30 sec agitate
        B. Hard bake (hot plate): 50 seconds @ 110 C
        C. O2 plasma to remove film: RF 150-200 W; O2 50-100 sccm: 3 min

(d) P-Mesa Dry Etch
    i. SiO_2 hard mask etch recipe
        A. Temp: 20 C
        B. ICP: 0 W
        C. RF: 100 W
        D. DC Bias: 200 V
        E. Gas #1: CHF3 25 sccm
        F. Gas #2: N/A

            G. Pressure: 98 mTorr
            H. He backing: 14 sccm
        ii. SiO_2 hard mask etch rates
            A. SiO_2: 7 nm/min
            B. PR: 4 nm/min
        iii. Metal/III-V etch recipe
            A. Temp: 50 C
            B. ICP: 200 W
            C. RF: 115 W
            D. DC Bias: 395 V
            E. Gas #1: N2 20 sccm
            F. Gas #2: Cl2 8 sccm
            G. Pressure: 4 mTorr
            H. He backing: 20 sccm
        iv. Metal/III-V etch rates
            A. SiO2: 23 nm/min
            B. GaAsSb: 115 nm/min
            C. InGaAs: 110 nm/min
            D. InAlGaAs: 180 nm/min
            E. InP: 100 nm/min
            F. Metal: 45 nm/min
    (e) Final P-Mesa

2. Step 02 N-Mesa
    (a) N-Mesa Lithography
        i. Chip clean/preparation
            A. Spray bottle clean acetone, IPA; DI rinse in beaker; nitrogen dry
            B. Hot plate bake 4 minutes @ 160 C
            C. O2 plasma: RF 150-200 W; O2 50-100 sccm; 5-20 min
        ii. Spin resist

      - A. HMDS precursor: 30 seconds @ 3000 rpm @ 3krpm/sec ramp
      - B. (Critical) Hot plate bake: 2 minutes @ 90 C
      - C. Spin AZ4330: 40 seconds @ 4000 rpm (3.9 um thickness)
      - D. Corner-bead removal & backside cleaning with cotton swab + acetone
      - E. Soft bake (hot plate): 1-2 minutes @ 100 C
    - iii. Exposure
      - A. Contact: hard or vacuum
      - B. Vacuum contact: seal pressure $>$ 12 kPa; check for WEC pressure specific to chuck
      - C. Exposure @ 365 nm & 10 mW: dose $\sim$170 mJ/cm, $\sim$8 seconds
    - iv. Development
      - A. AZ400K/DI (1:4) agitate: 60 sec @ RH = 36%
      - B. Hard bake (hot plate): 2 minutes @ 100 C
      - C. O2 plasma to remove film: RF 150-200 W; O2 50-100 sccm: 3 min
  - (b) N-Mesa Dry Etch
    - i. III-V etch recipe
      - A. Temp: 50 C
      - B. ICP: 200 W
      - C. RF: 115 W
      - D. DC Bias: 395 V
      - E. Gas #1: N2 20 sccm
      - F. Gas #2: Cl2 8 sccm
      - G. Pressure: 4 mTorr
      - H. He backing: 20 sccm
    - ii. III-V etch rates
      - A. InAlGaAs: 180 nm/min
      - B. InP: 100 nm/min
      - C. PR: 180 nm/min
  - (c) Final N-Mesa

3. Step 03 N-Metal

(a) N-Metal Lithography
  i. Chip clean/preparation
    A. Spray bottle clean acetone, IPA; DI rinse in beaker; nitrogen dry
    B. Hot plate bake 4 minutes @ 160 C
    C. O2 plasma: RF 150-200 W; O2 50-100 sccm; 5-20 min
  ii. Spin LOR and resist
    A. LOR 3A: 45 seconds @ 2500 rpm @ 10 krpm/sec ramp
    B. Hot plate bake: 4:30 @ 160 C
    C. Spin AZ5214: 40 seconds @ 3000 rpm @ 3 krpm/ sec ramp
    D. Edge-bead removal & backside cleaning with cotton swab + acetone
    E. Soft bake (hot plate): 2 minutes @ 100 C
  iii. Exposure
    A. Contact: hard or vacuum
    B. Vacuum contact: seal pressure $>$ 12 kPa; check for WEC pressure specific to chuck
    C. Exposure @ 365 nm & 10 mW: dose $\sim$170 mJ/cm, $\sim$8 seconds
  iv. Development
    A. AZ300 MIF agitate: 30 sec
    B. Hard bake (hot plate): 50 seconds @ 110 C
    C. O2 plasma to remove film: RF 150-200 W; O2 50-100 sccm: 3 min

(b) SiO_2 Wet Etch
  i. Wet etch: agitate in BOE

(c) N-Metal Evaporation
  i. E-Beam metal evaporation
    A. AuGe 100-Å @ 1.0- Å/sec
    B. Ni 100- Å @ 1.0- Å/sec
    C. Au 1000- Å @ 1.0- Å/sec (suggest x2-3)
  ii. Lift-off
    A. Soak in Remover PG @ 50 C: 10-20 min
    B. Low power ultrasonic bath in Remover PG: 10-30 seconds

   (d) Final N-Metal

4. Step 04 SU8 Planarization
   (a) SU8 Lithography
      i. Chip clean/preparation
         A. Spray bottle clean acetone, IPA; DI rinse in beaker; nitrogen dry
         B. Hot plate bake 4 minutes @ 160 C
         C. O2 plasma: RF 150-200 W; O2 50-100 sccm; 5-20 min
      ii. Spin resist
         A. HMDS precursor: 30 seconds @ 3000 rpm @ 3krpm/sec ramp
         B. Bake (hot plate): 3 minutes @ 100 C
         C. Spin SU8 2005:
            10 seconds @ 500 rpm @ 100 rpm/sec ramp
            35 seconds @ 2000 rpm @ 300 rpm/sec ramp
         D. Backside cleaning with cotton swab + acetone
         E. Soft bake (hot plate): 3:30 minutes @ 95 C
         F. Slow cooling on cleanroom paper
         G. Edge bead removal with cotton swab + acetone
      iii. Exposure
         A. Contact: hard or vacuum
         B. Vacuum contact: seal pressure $>$ 12 kPa; check for WEC pressure specific to chuck
         C. Exposure @ 365 nm & 10 mW: dose $\sim$115 mJ/cm
         D. Post exposure bake: 3 minutes @ 95 C (critical)
      iv. Development
         A. SU8 Developer:
            1 minute agitate
            Fresh developer 10 seconds agitate
         B. IPA rinse
         C. IPA soak 20 seconds
         D. N2 dry

      E. Cure bake (hot plate): 200-230 C 20 minutes

  (b) SU8 Dry Etch

    i. III-V etch recipe

      A. Temp: 10 C
      B. ICP: 0 W
      C. RF: 80 W
      D. DC Bias: 320 V
      E. Gas #1: O2 40 sccm
      F. Gas #2: SF6 4 sccm
      G. Pressure: 20 mTorr
      H. He backing: 20 sccm

    ii. SU8 etch rate

      A. SU8: 240 nm/min

  (c) Final SU8

5. Step 05 Signal Metal

  (a) Signal Metal Lithography

    i. Chip clean/preparation

      A. Spray bottle clean acetone, IPA; DI rinse in beaker; nitrogen dry
      B. Hot plate bake 4 minutes @ 160 C
      C. O2 plasma: RF 150-200 W; O2 50-100 sccm; 5-20 min

    ii. Spin LOR and resist

      A. LOR 3A: 45 seconds @ 2500 rpm @ 10 krpm/sec ramp
      B. Hot plate bake: 4:30 @ 160 C
      C. Spin AZ5214: 40 seconds @ 3000 rpm @ 3 krpm/ sec ramp
      D. Edge-bead removal & backside cleaning with cotton swab + acetone
      E. Soft bake (hot plate): 2 minutes @ 100 C

    iii. Exposure

      A. Contact: hard or vacuum

            B. Vacuum contact: seal pressure $>$ 12 kPa; check for WEC pressure specific to chuck
            C. Exposure @ 365 nm & 10 mW: dose $\sim$170 mJ/cm, $\sim$8 seconds
        iv. Development
            A. AZ300 MIF agitate: 30 sec
            B. Hard bake (hot plate): 50 seconds @ 110 C
            C. O2 plasma to remove film: RF 150-200 W; O2 50-100 sccm: 3 min

(b) Signal Metal Evaporation
    i. E-Beam metal evaporation
        A. Ti 100-Å @ 1.0- Å/sec
        B. Au 2200- Å @ 1.0- Å/sec
    ii. Lift-off
        A. Soak in Remover PG @ 50 C: 10-20 min
        B. Low power ultrasonic bath in Remover PG: 10-30 seconds

(c) Final Signal Metal

Appendix B

Honk Kong Epi Details

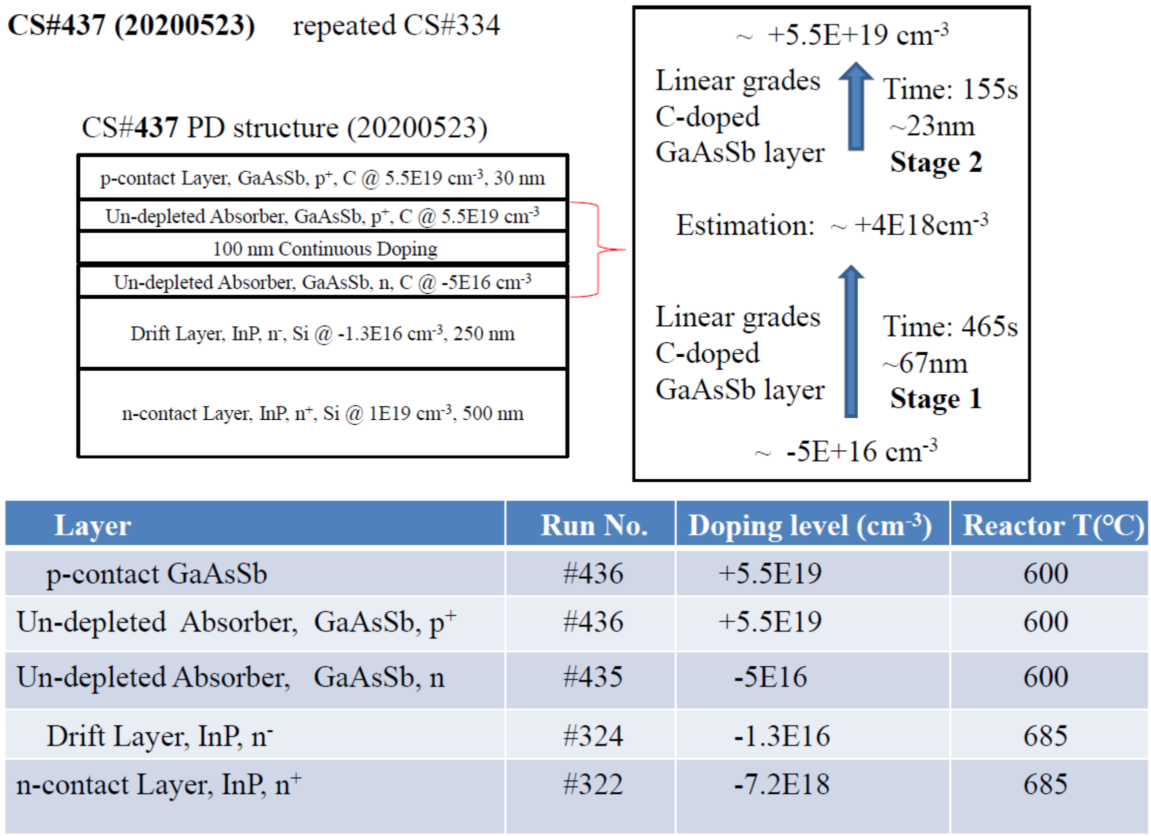
CS#437 (20200523) repeated CS#334

CS#**437** PD structure (20200523)

p-contact Layer, GaAsSb, p^+, C @ 5.5E19 cm^{-3}, 30 nm

Un-depleted Absorber, GaAsSb, p^+, C @ 5.5E19 cm^{-3}

100 nm Continuous Doping

Un-depleted Absorber, GaAsSb, n, C @ -5E16 cm^{-3}

Drift Layer, InP, n^-, Si @ -1.3E16 cm^{-3}, 250 nm

n-contact Layer, InP, n^+, Si @ 1E19 cm^{-3}, 500 nm

Layer	Run No.	Doping level (cm^{-3})	Reactor T(°C)
p-contact GaAsSb	#436	+5.5E19	600
Un-depleted Absorber, GaAsSb, p^+	#436	+5.5E19	600
Un-depleted Absorber, GaAsSb, n	#435	-5E16	600
Drift Layer, InP, n^-	#324	-1.3E16	685
n-contact Layer, InP, n^+	#322	-7.2E18	685

Figure B.1: Details of Hong Kong epitaxial growth. The sample fabricated and characterized in this thesis refers to structure #CS437.

CS**437** PD structure (20200523) repeated CS334

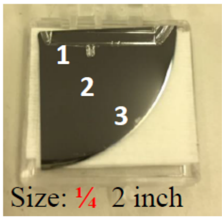

Size: ¼ 2 inch

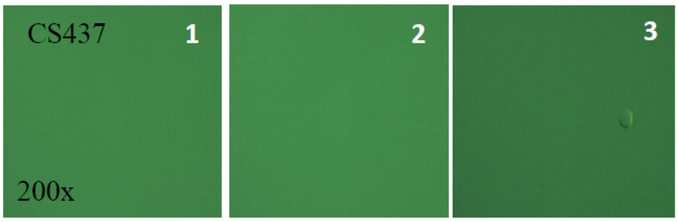

CS437 **XRD fitting**

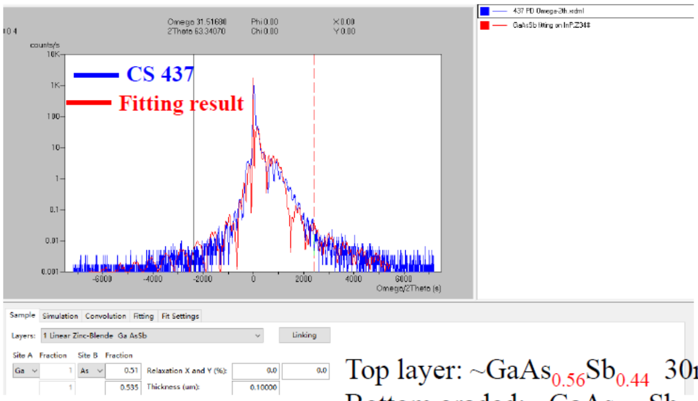

Layers: 1 Linear Zinc-Blende Ga AsSb

Site A	Fraction	Site B	Fraction			
Ga	1	As	0.51	Relaxation X and Y (%):	0.0	0.0
	1		0.535	Thickness (um):	0.10000	

Top layer: ~$GaAs_{0.56}Sb_{0.44}$ 30nm
Bottom graded: ~$GaAs_{0.51}Sb_{0.49}$ to
100 nm ~$GaAs_{0.535}Sb_{0.465}$

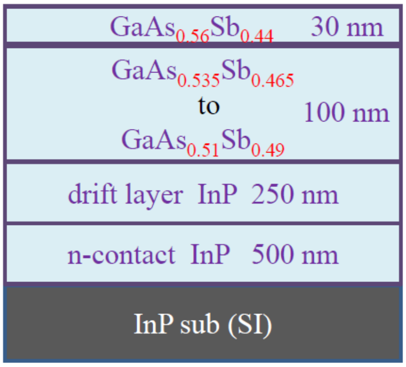

$GaAs_{0.56}Sb_{0.44}$	30 nm
$GaAs_{0.535}Sb_{0.465}$ to $GaAs_{0.51}Sb_{0.49}$	100 nm
drift layer InP	250 nm
n-contact InP	500 nm
InP sub (SI)	

Fitting result

Figure B.2: Details of Hong Kong epitaxial growth. The sample fabricated and characterized in this thesis refers to structure #CS437.

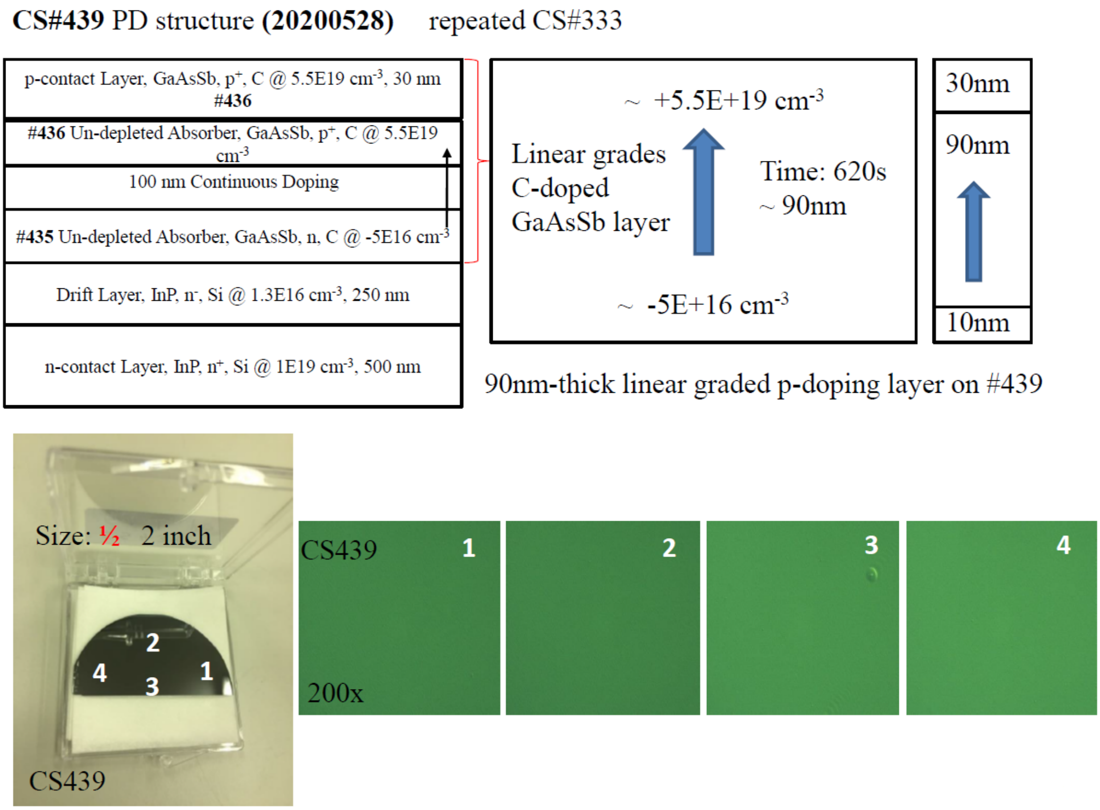

Figure B.3: Details of Hong Kong epitaxial growth. The sample fabricated and characterized in this thesis refers to structure #CS437.

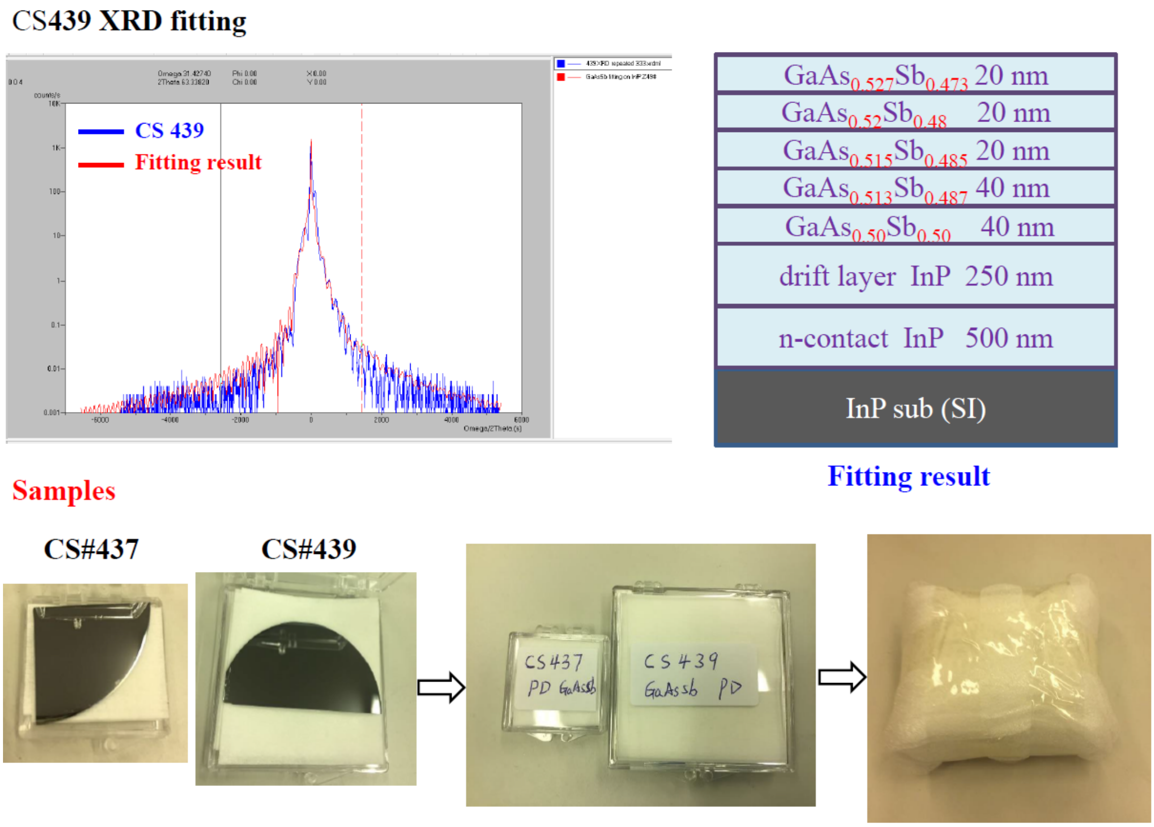

Figure B.4: Details of Hong Kong epitaxial growth. The sample fabricated and characterized in this thesis refers to structure #CS437.